ISBN 978-82-471-4026-0
ISBN 978-82-471-4027-7
ISSN 1503-8181

NTNU – Trondheim
Norwegian University of
Science and Technology

Mahdi Shabanimashcool

Doctoral theses at NTNU, 2012:349

NTNU

Doctoral Thesis

NTNU
Norwegian University of Science and Technology
Thesis for the degree of Philosophiae Doctor
Faculty of Engineering Science and Technology
Department of Geology and
Mineral Resources Engineering

Doctoral theses at NTNU, 2012:349

Mahdi Shabanimashcool

Numerical modelling of the longwall mining and the stress state in Svea Nord Coal Mine

NTNU – Trondheim
Norwegian University of
Science and Technology

Mahdi Shabanimashcool

Numerical modelling of the longwall mining and the stress state in Svea Nord Coal Mine

Thesis for the degree of Philosophiae Doctor

Trondheim, September 2012

Norwegian University of Science and Technology
Faculty of Engineering Science and Technology
Department of Geology and Mineral Resources Engineering

NTNU – Trondheim
Norwegian University of
Science and Technology

NTNU
Norwegian University of Science and Technology

Thesis for the degree of Philosophiae Doctor

Faculty of Engineering Science and Technology
Department of Geology and Mineral Resources
Engineering

ISBN 978-82-471-4026-0
ISBN 978-82-471-4027-7
ISSN 1503-8181

Doctoral theses at NTNU, 2012:349

MILJØMERKET 241 TRYKKSAK 731

Printed by Skipnes Kommunikasjon as

To the people lost their life during the Azerbaijan earthquakes on 12/08/2012

Abstract

This thesis presents numerical and analytical investigation of the geomechanics underlying longwall mining. It was tried out to study the disturbances induced by longwall mining in nearby rocks and their influence on the stability of the gates, pillars and main tunnels of longwall mines. The thesis consists of two major parts: numerical and analytical investigations. The study site is the Svea Nord coalmine, Svalbard, Norway.

A novel algorithm was proposed for numerical simulation of the longwall mining process. In the proposed algorithm progressive cave-in and fracturing of the roof strata, consolidation of the cave-in materials and stress changes are simulated in detail. In order to outline the caved-in roof rocks a criterion based on maximum principal strain (in tension) was used. The critical tensile strain of roof cave-in was determined through back-calculation of the surface subsidence above a longwall panel at the mine. The results of the simulations were then used to analyse stress changes induced by longwall mining and the stability of gates. The simulations revealed that the stability of the gates and the loading to the rock bolts are closely related to the width of the chain pillars. With slender pillars, shear displacements along weak interlayers and bedding planes result in heavy loading to the rock bolts. Therefore, the locations of weakness zones should be taken into account in rock bolt design.

The developed algorithm was implemented to study the loading and stability of the barrier pillar of the mine. The barrier pillars protect the main tunnels and border area of the mine from disturbances induced by longwall mining in the panels. The simulations show that the stresses in the barrier pillars fluctuate up and down during mining because of periodic cave-in events behind the longwall face. A failure zone of about 12 m exists in the wall of the barrier pillars. A large portion of the barrier pillar is still intact and is, thus, capable of protecting the border area.

The results of the detailed simulations of longwall mining via the developed algorithm were, also, implemented in a large-scale numerical model. The model consists of all of the longwall panels and the border area of the mine. It is intended that the coal in the border area on the other side of the longwall panels will be mined after completion of the longwall mining. There is concern about how the longwall mining affects the stress state in the border area and how stress changes would affect future mining in the border area. A failure zone of about 20 m developed in the wall of the main tunnels on the side of the border area after all the longwall panels were mined out. The stress state in the remaining portion of the border area remains unchanged. Therefore, it will be possible to mine the border area in the future.

In order to investigate the roof strata cave-in mechanism in detail a discontinuous numerical simulation of roof cave-in process was conducted by UDEC code. The block size in the roof strata and the mechanical parameters of the discontinuities were obtained through back-calculations. The back-calculations were conducted with a statistical method, Design of Experiment (DOE). Numerical simulations revealed that jointed voussoir beams formed in the roof strata before the first cave-in. Beam bending results in stress fluctuations in the roof strata. The maximum deflection of a roof stratum at the study site before the first cave-in is about 70% of the stratum thickness. The simulations and field measurements show no periodic weighting on the longwall shields in this mine. Numerical sensitivity analyses show, however, that periodic weighting may occur in strong roof strata. Roof strata with a high Young's modulus and large joint spacing are not suitable for longwall mining. The maximum sustainable deflection of the roof strata before cave-in depends upon the horizontal in-situ stress state. It slightly increases with the in-situ horizontal stress in the stratum beams, but the horizontal stress would increase the possibility of rock-crushing in deflected roof beams. The implemented numerical method would be useful in assessment of the cavability of the roof strata and in selection of longwall shields with adequate load capacity.

As shown through discontinuous numerical simulations, the roof strata above the underground opening constructed in the stratified rocks form voussoir beams. The stability of those beams is the major concern in the study of the gate stability and roof cave-in assessment in the longwall panels. Two different analytical methods were developed for cases with and without the in-situ horizontal stress acting along the beams. In the analytical model for the beams without horizontal stress a bilinear shape was assumed for the compression arch generated within the voussoir beams. The stability of the compression arch is governed by the energy method. The model requires an iterative procedure for convergence, and an algorithm was proposed for it. The analytical method was verified with numerical simulations by means of a discrete element code, UDEC. For the beams subjected to in-situ horizontal stress, the classic beam theory was employed to drive the analytical solution for it. The superposition method was used to obtain bending/deflection equations of the beam. The validity of both the assumptions and the developed method were, also, investigated by numerical simulations. The developed analytical method revealed that high Young's modulus of a beam rock increases the stability of the beams against buckling but it causes higher stress within the compression arch which increases the probability of crushing failures in the beam abutments and midspan. In-situ horizontal stress along beams increases their stability against buckling and abutment sliding failure, but it raises the possibility of crushing failure at the abutments and the midspan.

Key words: Longwall mining, Numerical simulation, Cave-in, Voussoir beam, Rock support, Gate, Pillar

Acknowledgments

I wish to express my deepest gratitude to my supervisor Professor Charlie Chunlin Li whose insight, guidance, meticulous review, and criticism of the work had a significant impact not only in this thesis but also on my perception of research in Rock Mechanics. His inspiration attitude toward research, trust in his students, and insight into the problem, left a significant impression on this work.

I am very grateful for the financial support provided by Store Norske Spitsbergen Kulkompani. Particularly, I give my deepest heart-felt thanks to the miners in Svea Nord coal mine; their hard working has given me this opportunity. I cannot thank them enough as my life will always bear an imprint of their efforts.

I would like to thank for the helps and supports of the Svea Nord mine manager Mr. Per Nilsen. I am grateful for the helps and corporations of Mr. Tomas Warnqvist; his great attitude of working inspired me always. I appreciate very much the helps and supports of Mr. David Hovland and Mr Magne Larsen; they helped me a lot during my first visits of the mine. I also would like to thank the design team of Lunckefjell mine, which allowed me to apply my achievement during this PhD research in the new mine design.

I am grateful for the instructive corporation with Professor Lanru Jing (Department of Engineering Geology and Geophysics, School of Architecture and the Built Environment, KTH - Royal Institute of Technology) during the course of the discontinuous numerical simulations.

I am grateful to the Professor Arne Myrvang (Department of Geology and Mineral Resource Engineering, NTNU) and Professor Lu Ming (School of Civil and Environmental Engineering, Nonyang Technological University) for their suggestions and comments in the course of the research.

I wish to express my thanks for my PhD colleagues for the interesting discussions and pleasant working environment. Special thanks are given to the Department of Geology and Mineral Resource Engineering, NTNU, for all the great corporations and helps during last four years.

I am thankful to my parents for their unconditional love, support and sacrifices over all this years. I am thankful to my brother and sisters for all their love and supports.

I am grateful to my friends in Greenfield football team, thank you for sharing your free-time with me. I always inspired by the competition attitude of you guys. I wish to thank my friend, Mohammad-Hossein Mohammadlu, for his helps during these four years. I am grateful to my friend Mrs. Nielster Ann Malay, for here helps. I am grateful to Mrs. Nelia Castro for reviewing of the final draft of the thesis.

Contents

List of figures

List of Tables

List of symbols

Roman Symbols

A: Average area of compression arch cross-sections along a beam

b: Maximum height of cave-in zone

c: cohesion of rock materials

d: Thickness of beam

E: Young's modulus

E_0: Initial tangency modulus of cave-in materials

F: Compression arch force

G: Shear modulus

g: Gravitational acceleration

H: Overburden

h: Height of roof strata from the stope floor

h_c : Height of stope

h_{cr} : Maximum thickness of cave-in zone

h_f : Height of the fractured zone from panel floor

I: Moment inertia of a beam cross-section

K: Bulk modulus

K_n : Normal stiffness of joints

K_s: Shear stiffness of joints

l_{Open} : Open length of the abutment joints of a voussoir beam subjected to in-situ horizontal stress

l_p : First cave-in distance

l_S : Periodic cave-in distance

M_0: Bending moment at beam ends

n: Thickness of compression arch along the beam

n_0 : Thickness of compression arch at the abutments and midspan of a voussoir beam

P: Horizontal force at a beam ends induced by in-situ horizontal stress

R_b: Hydraulic radius of rock blocks

S: Beam span

S_j : Spacing of crosscut joints

S_{ult} : Ultimate stable span of a beam against buckling

T : Bending moment of a beam

T_{max}: Maximum bending moment

w_p: Width of a longwall panel

Z_0: Primary height of arch axis

Z: Height of arch axis after deflection

BF: Bulking factor

FS_{bk} : Factor of safety against buckling

FS_{sl} : Factor of safety against sliding

FS_{cr} : Factor of safety against crushing

Greek symbols

α : Primary angle of a arch axis with a horizontal line

β : Deflection angle of arch axis

σ : Normal stress

γ : Unit weight of rocks

ϕ : Friction angle

ρ: Density

θ: Abutment angle

ε_v : Volumetric strain

ε_v^m : Maximum volumetric strain

ε_1^p : Maximum principal plastic strain

ε_1^t : Maximum principal total strain

ε_1^e : Maximum principal elastic strain

ε^c : Critical cave-in strain

δ: Maximum deflection of a beam

δ_m^f : Maximum deflection a continuum beam with end-fixed condition

$\sigma_{\max}^f$: Maximum bending stress at the beam with end-fixed condition

$\sigma_{\max}^p$: Maximum bending stress of a beam with pinned-end

σ_{ci} : Uniaxial compressive strength of rocks

σ_m : Maximum abutment stress of a voussoir beam

$\sigma_{\max}^{ab}$: Maximum abutment stress of a voussoir beam subjected to in-situ horizontal stress

1 Introduction

Coal is one of the energy resources in the earth which has been used for centuries. Mainly coal is mined out either with surface or underground mining methods. Nowadays, due to the lack of the surface deposits of the coal and environmental issues, the underground coal mining is very popular. Majority of the coal mines uses either room-and-pillar or longwall mining methods. The longwall mining method is the most popular and productive method for coal mining in the world.

The study site in this research is the Svea Nord coal mine, located at Spitsbergen, Svalbard, Norway. In the Svea Nord mine, the longwall mining method is employed to extract coal from underground. The longwall is 250 m long and every panel covers an area of 250 m x 2500-3000 m. The longwall mining will be finished in two years. After that, it is intended that the remainder of the coal seam in the border area of the mine will be mined by either the room-and-pillar or the longwall method. Longwall mining in the panels dramatically changes the in-situ stress state in the border area. Mining also initiates and propagates fractures and yielding of the mine's host rock masses in the border area. Therefore, mining in the border area will be a challenging practice.

This research aims to study longwall mining geomechanics in detail and to develop engineering tools to consider those mechanisms in the stability analysis of the gates, pillars and main tunnels of the mine. The thesis focuses particularly on the disturbances induced by longwall mining in the border area of the study site. The results of this study would help to improve the stability of the mine's gates, main-tunnels, pillars and stopes, particularly in the border area.

This thesis is based on the following published/under review articles:

- Shabanimashcool M, Hovland, D, Li, C.C. (2010) ‘Numerical analysis of the rock support of the tailgates in Svea Nord mine’, in *Proceeding of Rock Mechanics in the Nordic countries*, pp. 250-262.

- Shabanimashcool, M. Li, C.C. (2011) ‘Numerical Study on disturbance of longwall mining to stress state in the rock mass’, in Qian, Q. and Zhou, Y. (eds) *Proceeding of 12th ISRM International Congress on Rock Mechanics*, Beijing, China, pp. 1579-1585.

- Shabanimashcool M, Li, C.C. (2012) ‘Numerical modelling of longwall mining and stability analysis of gates in a coal mine’, *International Journal of Rock Mechanics and Mining Science*, 51, pp. 24-34.

- Shabanimashcool M, Li C.C. (2012) ‘A numerical study of stress changes in barrier pillars and a border area in a longwall mine’, Submitted to: *Coal Geology*.

- Shabanimashcool, M. Jing, L. Li, C.C. (2012) ‘Discontinuous modelling of stratum cave-in in a longwall coal mine’, Submitted to *Geological and Geotechnical Engineering*.

- Shabanimashcool, M. Li, C.C. (2012) ‘Analytical methods for investigation stability of the laminated roof strata above underground openings’, Would be submitted to *International Journal of Numerical and Analytical Methods in Geomechanics*.

In longwall mining, the stability of the gates, tunnels, pillars and stopes is related to both the roof cave-in performance and the interaction of the cave-in materials with the overburden rocks. Therefore, they should be carefully considered in the investigations. Roof cave-in is a dynamic phenomenon, which begins at a critical distance from the panel start-up and continues periodically with stope face advances. That dynamic procedure must be considered in the stability analyses and design of roof and rib support for the gates, pillars and stopes.

Owing to the inaccessibility of the goaf area in longwall mines, it is very difficult to observe and characterise the roof cave-in procedure. The only practicable method is to study it indirectly by looking at the longwall shield load, pillar load, gate roof and rib support as well as surface subsidence. Thus, for calibration of the developed methods for studying longwall geomechanics a proper algorithm of back-calculations is also required. Such back-calculations might lead to more than one answer, of which the physically acceptable one should be chosen.

Moreover, in the coal mining industries there is still a noticeable lack of knowledge regarding the geomechanics of longwall mining and ill-designed roof support and longwall layout could cause gate collapse, stope jamming, and rock and air bursts. Nowadays, the design of chain pillars and the roof support for gates are usually conducted by the empirical methods developed for the USA and Australian coal mines, ALPS (Mark et al. 1994) and ALTS (Colwell et al. 2003), respectively. These methods and their recommended design criteria are based on data collected from industrial practices. Their applicability to other mines is restricted because they do not combine geomechanics with the statistics from collected field data.

1.1 Research Objective

The main objective of this thesis is to estimate disturbances induced by longwall mining in the surrounding rocks and border area of the study site, and then use those results for studying the stability of gates, main tunnels, pillars and stopes as well as designing mine layout.

To achieve those objectives, it is necessary to improve our understanding of the roof strata cave-in mechanism and develop a method for its inclusion in longwall planning and support design. Therefore, this research explores:

- progressive roof strata cave-in and fracturing mechanism above longwall panels
- interaction of the caved-in materials with the overburden rocks
- longwall mining induced disturbances to the stress state and the rock masses at the border area of the study site.

It also tries to develop:

- an approach which accommodates the dynamic procedure of roof cave-in in the stability analysis of gates, main tunnels and pillars
- developing analytical easy-to-follow methods for studying the stability of roof strata above the underground opening in stratified rocks.

The major part of the research was conducted through continuous numerical simulations with FLAC$^{(3D)}$. A novel algorithm was developed and implemented in FLAC$^{(3D)}$ to simulate progressive roof cave-in, fracturing and the consolidation of the cave-in material under the weight of overburden rocks. In order to study the roof cave-in in detail, discontinuous simulations with UDEC code were conducted. The code has the ability to consider the rock joints in detail while the rock blocks are deformable. Finally, two analytical methods were developed to study roof stability of the openings constructed in the stratified rocks.

Enhancing our knowledge regarding longwall geomechanics will, it is hoped, help the Svea Nord mine and other coal mines to extract coal from underground more efficiently and economically and in an environmentally friendly fashion.

1.2 Thesis outline

The thesis systematically examines longwall mining geomechanics. It first focuses on describing current knowledge about longwall mining geomechanics. After that an algorithm is developed for numerical simulation of the longwall mining procedure and implemented at the study site. The model is calibrated by the field measurement data. The modelling results achieved by the algorithm have been used to establish a mine-scale model to study longwall mining-induced disturbances at the border area.

Discontinuous numerical simulation was used for detailed study of the roof cave-in process. Eventually, based on those investigations, an analytical method was proposed for studying the stability of the roof strata in the underground opening constructed in the stratified rocks.

In Chapter 2 the background and current knowledge about longwall mining geomechanics are presented. The advantages and disadvantages of the different methods are discussed briefly and the challenges tackled by this research were described.

In Chapter 3, the study site is introduced and it’s geological and geomechanical characteristics are presented. The field measurement data, which have been used for back-calculations and calibration of the numerical models, are also presented.

In Chapter 4, a new algorithm is proposed for numerical modelling of longwall mining and calibrated with the field measurement data.

Chapter 5 presents the numerical results about the stability of the gates obtained via the developed algorithm. The influences of the overburden height and chain pillar dimension on the bolt loads are, also, investigated in detail.

The stress changes ahead the stope face and within the goaf area are studied in Chapter 6. Loading of the barrier pillars and longwall mining-induced disturbance at the border area of the study site are studied in detail with numerical simulations.

Detailed simulations of the roof cave-in process were conducted by a discontinuous numerical code, UDEC. The beam theory was used to explain the cave-in mechanism. These simulations are presented in Chapter 7.

In Chapter 8, analytical methods are proposed based on the beam theory to study the stability of the roof strata over the gates and panels. The methods are easy to follow and fast, so they could be used for engineering purposes.

Conclusions and contributions of the thesis are presented in Chapter 9 and the suggestions for the further research are included in Chapter 10.

2 State of the art

2.1 Introduction

This chapter presents a literature review and the current knowledge about longwall mining geomechanics. It describes the limitations and achievements of the current methods and the necessity for the research conducted in this PhD study.

The longwall mining method is distinguished from other mining methods by the fact that the roof strata over the open stope cave in and fill the stope void. This cave-in process induces severe disturbances to the rocks surrounding the longwall panels. Therefore, special considerations are needed in the study of the geomechanics of longwall mining.

In this chapter, the longwall mining method, in-situ stress redistribution induced by longwall mining and the stability of the gates and chain pillars of longwall panels are briefly discussed.

2.2 Longwall mining

Coal is one of the world’s most abundant fossil fuels and is mined either on the surface or from underground. Coal is mostly used for steel production and electricity generation, which give it a strategic value. In underground coal mines, longwall and room-and-pillar mining methods are largely used to extract the coal. The longwall mining method is the most productive and popular one.

Longwall mining is an exploitation method used for flat-lying, tabular deposits in which a long face is established to extract the mineral (Hartman & Muntmansky 2002). In the longwall panels, large blocks of coal about 200-300 m wide and 2-3 km long are mined. The panels have two major tunnels on each side, known as headgates and tailgates, supplying fresh air for the stope and transportation facility, Figure 2.1. The headgate of a panel when mined-out becomes the tailgate of the adjacent panel. In this research, the general term ‘gates’ is used for both tailgates and headgates. In multiple-entry gates, pillars between two adjacent tunnels are constructed, known as chain pillars. A pillar with large dimensions also separates longwall panels from the main tunnels of the mine, and this is known as the barrier pillar. The geometry and configuration of the chain pillars considerably influence the productivity and safety of the longwall operation.

The coal is extracted along the stope face by a shearer or tabular coal cutter heads and collected via the elbows of a collecting machine which transfers the coal into a conveyor belt. Then, the belt transfers coal through the tailgates to the outside of the mine. The stope space is protected from roof collapse by hydraulic shields, called longwall shields. Hydraulic jacks are placed in the longwall shields to support the unstable roof and prevent it from collapsing and filling the stope void underneath. By cutting of the coal, the longwall shields move further to support the recently excavated area. With further advance of the stope face, the roof strata of the open stope behind the longwall shields cave in and fill the stope void. The fully filled cave-in area is known as the goaf, gob or caved-in zone. The roof strata cave-in significantly affects the stability of the stope and gates as well as the main tunnels.

In longwall mining, stope voids are filled by cave-in materials. Cave-in of roof strata results in stress redistribution in the rock mass surrounding longwall panels and it improves the stability of the stope with reducing of both the load on the longwall shields and the stresses in the abutments of the stope. A delayed roof cave-in could have severe consequences, for instance stope jamming, stope face bursting and rock and air bursts. Therefore, a thorough understanding of the roof cave-in mechanism is helpful for ground control design in the planning stage of longwall mining, for instance in estimating the load capacity of longwall shields and the length of longwall stopes.

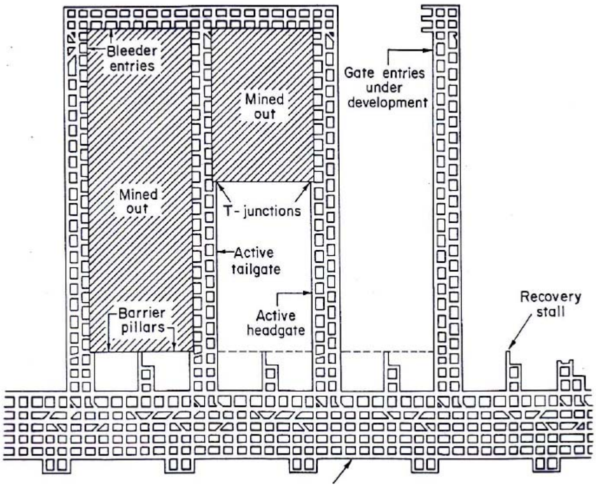

Figure 2.1 A typical layout of a longwall mine (Mark 2000)

Roof cave-in is a complex dynamic process involving rock fracturing, disintegration and movement. The cave-in materials are compacted and consolidated afterward and the stress concentration in the chain pillar is reduced (Brady & Brown 2002). The roof strata above the longwall panels can be divided into three zones: the cave-in zone, the fracture zone and the continuous deformation zone (Figure 2.2) (Peng & Chiange 1984). Duplancis & Brady (1999) defined the cave-in zone as the region in which rock blocks are separated from the host rock strata and fall into the panel void. The fracture zone refers to the region in which rocks are fractured and lose some or all of their cohesion on the fracture planes. The continuous deformation zone consists of two regions: a seismic active zone and an elastic deformation zone. The seismic zone is located immediately above the fracture zone, where microseismic activities occur on bedding planes and other types of discontinuities. The elastic deformation zone refers to the rest of the rocks above the seismic active zone which behave elastically.

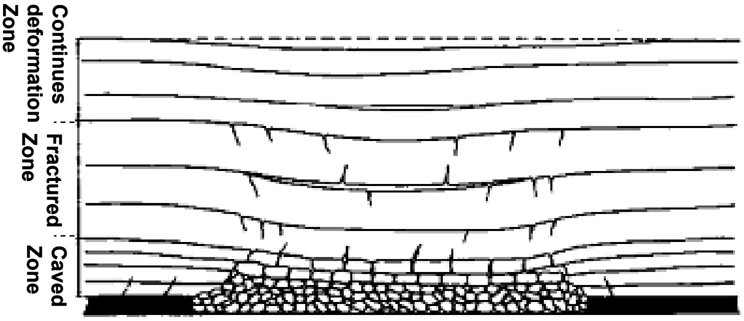

Figure 2.2 Disturbed zones over a longwall panel (Brady & Brown; 2002).

Peng & Chiang (1984) developed a scenario based on field observations to illustrate the process of roof strata cave-in in longwall mines (Figure 2.3). In their scenario, the first cave-in occurs when the stope length reaches a critical distance l_p at which the stope void is fully filled by caved-in materials. The thickness of the caved-in strata is constant in the middle of the caved zone, whereas it decreases with the distance to the longwall face, resulting in a domed roof, composed of cantilever beams of laminated rock, behind the face. Cave-in behind the face owing to breakage of the cantilever beams periodically occurs for every critical advance of l_s, until mining in the panel is completed. The cavability of a panel roof is associated with the critical lengths of l_s and l_p. Long l_s and l_p could result in violent cave-in events and release a large amount of energy per cave-in. This is harmful to stabilisation of the stope.

The first cave-in event in a panel involves the following processes in the roof strata: shear-fracturing ahead of the stope, bedding separation above the stope void and formation, deflection and finally collapse of voussoir beams. The collapsed voussoir beams fill the stope void underneath.

The periodic cave-in events also involve shear fracturing and separation of roof strata, but cantilever beams instead of voussoir beams collapse with every cave-in event. Shear fracturing occurs in the roof strata ahead of the face.

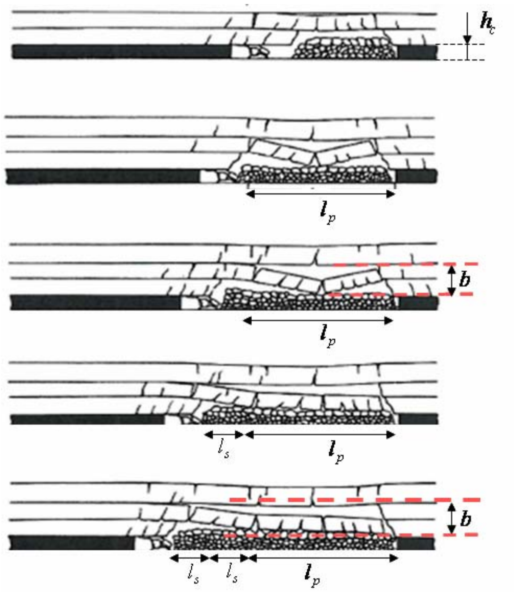

Figure 2.3 Roof strata cave-in scenario (after Peng & Chiange 1984). h_c and *b* refer to the thickness of coal seam and the maximum thickness of the cave-in zone.

The strata behind the face experience tensile fracturing and extension, resulting in separation of bedding planes. The stratified roof strata are crosscut by sub-vertical joints, which are either original or mining-induced. The rock blocks rotate and interlock with each other, forming a voussoir beam above the stope void. The dead weight of the beam as well as the ground pressure above are transferred to the abutments via the voussoir beam.

The primary failure modes of a voussoir beam are buckling, compressive failure (crushing) in the middle span and at the abutments, slippage at the abutments and diagonal fracturing (Figure 2.4) (Diederichs & Kaiser 1999a). Slippage and diagonal fracturing occur in thick beams with low span-to-thickness ratios, whereas crushing and buckling occur in slender beams with high span-to-thickness ratio. In longwall mines, the voussoir beams are usually of slender type since the thickness of a sedimentary rock layer is much smaller than the stope span.

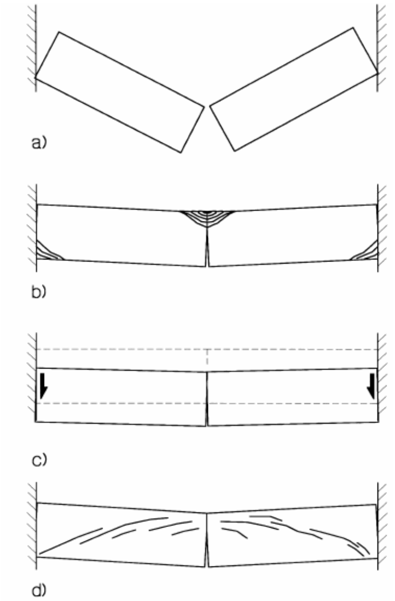

Figure 2.4 Failure modes of voussoir beams: (a) buckling (b) crushing (c) sliding and (d) diagonal cracking (Diederichs & Kaiser 1999a).

Voussoir beams are statically undetermined. Some analytical methods have been developed to study the stability of voussoir beams, and these are discussed in Chapters 7 and 8. In this research, the stability and mechanical behaviour of the voussoir beams are investigated by numerical simulation. New analytical methods are developed to stability analysis of the voussoir beams.

A number of analytical, empirical and numerical methods have been developed to assess roof cave-in performance (cavability) in longwall mining. Analytical solutions are typically based on either theoretical approaches such as beam theory or on conceptual parameters such as bulking factor. For instance, Obert & Duvall (1966) utilised beam theory to predict the first cave-in distance as well as the subsequent periodic cave-in distances. Analytical methods usually oversimplify the cave-in process, however, casting doubt on the results.

Empirical methods have been developed for India's coal mines to investigate the cavability of roof strata. Sheorey (1984) modified the Q rock mass classification system (Rock Tunnelling Quality Index, Barton et al. 1974) and used it for cave-in assessment in coal mines. He calculated the first cave-in distance based on the geomechanics of the rock mass surrounding the panel. Ghose and Dutta (1987) combined a rock mass classification approach with fuzzy set theory and proposed a new classification system for roof cavability in longwall mining. Das (2000) proposed another classification system for the roof strata cavability assessment using data collected from mechanised longwall panels in India. The applicability of the classification systems is restricted to the situations where relevant data are available. However, those classifications are developed on the basis of the specific geomechanical conditions of the mines. Furthermore, most of the data were collected from panels whose width was shorter than 150 m. Today, the width of longwall panels usually exceeds 200 m (Hartman & Muntmansky 2002). It should be noted that the increase in the width of longwall panels is vulnerable to roof cave-in.

In the past years, a number of attempts have been made to study the roof cavability by numerical methods. Singh & Singh (2009) implemented a numerical approach in FLAC$^{(2D)}$ to study the cavability of roof strata and loading on longwall shields. Their method is applicable for cases where open stopes are not yet fully filled by cave-in materials. Vakili & Habblewhite (2010) generalised the cave-in model of Smart & Aziz (1989) and implemented it in numerical UDEC models. They developed a cave-in criterion for Top Coal Caving longwall mining through statistics of the numerical results.

Other methods and models have been proposed to study the interaction between longwall shields and roof strata. They include the detached block model, bulking factor method, empirical methods, analysis of the cyclic load on longwall shields, neural network, numerical simulations and the ground response curve (Trueman et al. 2009). All of these methods have their limitations in terms of interpreting the interaction between strata and longwall shields (Trueman et al. 2009). Recently, Trueman et al. (2009) developed a code for monitoring strata-shield interaction. Such monitoring is useful in determining whether the shield capacity and setting pressure are adequate.

In summary, the existing methods are not efficient enough for determining the cavability of roof strata and the required support capacity of shields. Roof cave-in is a progressive process which starts at a critical distance behind the stope face and develops upward as the face advances. Cave-in ceases when the cave-in materials fully fill the stope void. The roof strata next to the stope face load the shields via downward deformation or the dead weight of the cave-in materials. Strong and massive roof strata do not cave in immediately, leaving an overhang behind the longwall shields. Periodic cave-in events occur after the first cave-in so that a periodic weighting is placed on the longwall shields. These phenomena may also be observed when the stope void is not yet fully filled. Moreover, the roof cave-in depends not only on the geomechanical characteristics of the roof strata, but is also associated with the height of the stope and the location of the bedding planes in the roof. As a result, numerical modelling is an appropriate method for simulating the dynamic process of cave-in and assessing the load on the longwall shields.

In this research, an algorithm for numerical modelling of longwall mining in FLAC$^{(3D)}$ is proposed, which takes into account roof strata cave-in, fracturing and consolidation of caved-in materials. The author used a critical tensile strain to outline the cave-in zone. In addition, the roof cave-in mechanism was studied via discontinuous numerical simulations. Discontinuous models describe rock masses more realistically than continuous models, an advantage which makes them preferable for studying mechanisms. The numerical models were verified with field measurement data of the study site.

2.3 In-situ stress redistribution induced by longwall mining

In longwall mining, stope voids are filled by caved-in rock materials. Cave-in of the roof strata results in stress changes in the rock mass surrounding the longwall panels. The stress redistribution is mainly associated with the in-situ stress state, the layout of the panels, and the mining sequence. The vertical stress in panel walls increases with an enlargement of the mined-out region. The horizontal stresses in the roof and floor also change by the advance of the longwall face or the enlargement of the mined-out void.

Whittaker (1974) developed an empirical approach to calculate the vertical stress ahead of the longwall face for rock conditions prevailing in the UK (Figure 2.5). In his approach, a yield zone exists ahead of the face. The vertical stress is zero both at the face and at the rib side and it increases quickly with the distance from the face. Wilson (1977, 1981) developed an analytical-empirical method for the same purpose, whose results agree with those of Whittaker (1974). Numerical analyses conducted by, for example, Park & Gall (1988) and Everling (1973) agree well with the results of Whittaker and Wilson. All these studies showed that the maximum abutment stress of four to six times the original vertical stress occures at a close distance from the stope face.

Recently, however, numerical studies and field measurements in Australia showed that the maximum abutment stress of about twice the original one occurs at a great distance from the stope face. Kelly et al. (1998) argued that those diversities are owed to the high horizontal stress acting along the panel. High horizontal stress causes shearing of the intact rock and bedding planes, which results in abutment stress concentration far ahead of the stope.

The horizontal stress redistribution owed to longwall mining has been studied through field measurements and numerical modelling. Such cases are, however, limited and there is no internationally accepted approach to assess the horizontal stress redistribution due to longwall mining. Gale and Blackwood (1987) carried out a numerical investigation on the influences of the horizontal stress orientation on the stability of the gates at an Australian colliery. They devised a graph, depicting the stability of the gate roof in relation to the orientation of the principal in-situ stress with alignment of the gates.

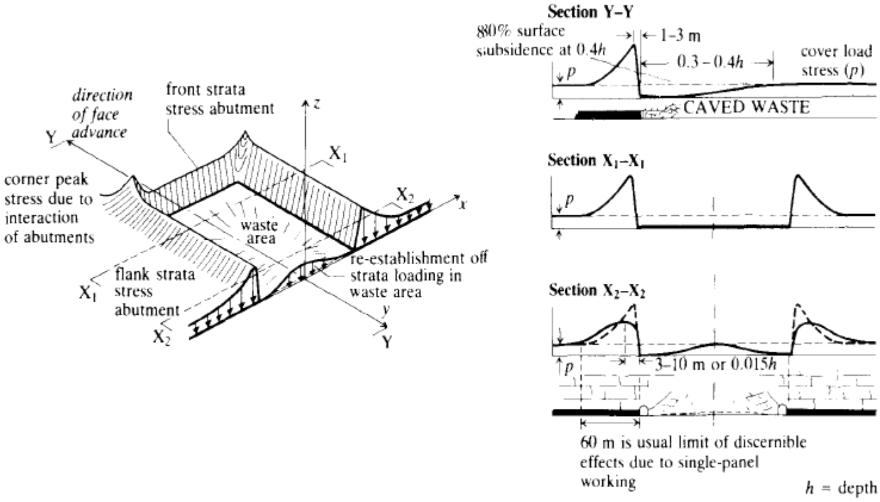

Figure 2.5 Vertical stress distribution in the coal seam level around the longwall face, (After Whittaker 1974)

Mark et al. (2007) investigated horizontal stress changes in the tailgate roof of a coal mine in the USA using detailed field measurements. They showed that horizontal stress in the direction perpendicular to the longwall panels dramatically increases owing to mining and the principal stresses reorient owing to roof strata yielding. They also claimed that the required length of the rock bolt for reinforcing of the roof strata is dependent on the magnitude of the horizontal stress perpendicular to the gates.

The stress redistribution is associated with the geological conditions, the mechanical properties of the rocks, the state of the in-situ stresses, the layout of the panels, the mining sequence, and so on. Neither analytical nor empirical approaches can take into account so many factors in their estimations, so their applications have limitations (Brady & Brown 2002). Oversimplifications, on the other hand, cause uncertainties in the results. Numerical modelling, however, provides us with an opportunity to include a good number of relevant factors in the analysis so that the results are more realistic than those of analytical-empirical approaches. Furthermore, the effects of a single factor can be easily studied numerically, which is helpful for identifying the most important factors for use in practice. Numerical modelling together with field measurements is an appropriate way for studying the stress redistributions in longwall coal mines.

2.4 Stability of gates

The stability of gates is essential to ensure the safety of longwall mines and continuation of production. In longwall mines, stope voids are filled by cave-in roof rocks. Roof cave-in causes rock fracturing and yielding as well as stress concentrations in the surrounding rock mass. Gates and chain pillars between longwall mining panels are subjected to a complex loading process throughout their service life. Roof bolting is one of the major measures applied to stabilise gates. Obviously, loading to the rock bolts is caused by the longwall mining. Therefore, analysis of the bolt load can be a proper method for studying the stability of gates.

Nowadays in longwall coal mines, the gates are constructed in a rectangular shape and the rock reinforcement approach is normally implemented to stabilise them. In some circumstances, however, the rock supports, i.e. wooden packs, are used to protect the tailgates in the zones close to the stope face. For instance, in Australian longwall mines, the roof is mainly reinforced by a pattern of 2.1 m long, grouted steel bolts which are installed through mesh and steel straps (Figure 2.6) (Brady & Brown 2002). In this approach, four to six rock bolts are installed in each row and the distance between each row is around 1-2 m. Cable bolts might be used in the intersections where the immediate roof beam weight is required to be carried by the cables. Rib-bolting is also a common stabilising activity in the gates where they have large height.

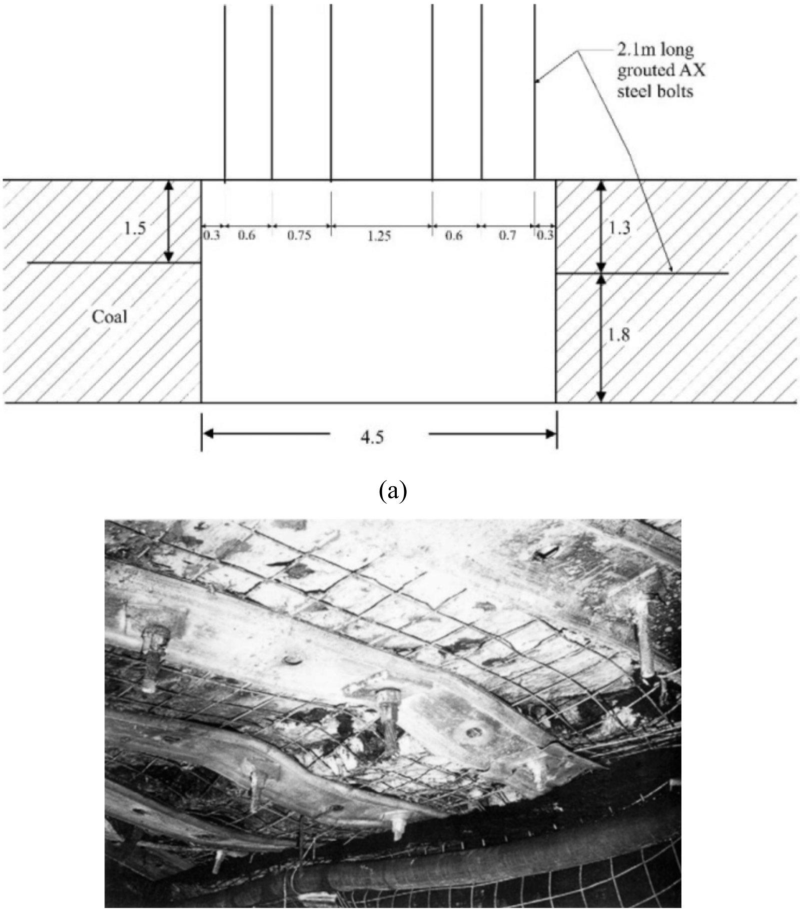

(a)

(b)

Figure 2.6 Gate reinforcement: (a) pattern (b) detail in practise (Brady & Brown 2002).

The design of roof-bolting and rib-bolting is associated with mining layout, the geomechanical characteristics of the roof strata and in situ stress state of the surrounding rocks (Brady & Brown 2002). The main mechanisms of the rock reinforcement loading in the gates are: bed separation, shearing at the bedding planes, failure of the rock materials, tensile failure of the rock materials and opening of the pre-existing rock joints, fall of the rock blocks and rib failure owing to the vertical stress concentration. Generally, there are four ways to estimate the bolt load and roof-bolting design: empirical, analytical, numerical and hybrid empirical-numerical methods.

Generally, the roof-bolting design is conducted by the ALPS (Mark et al. 1994, 2001) and ALTS (Colwell et al. 2003) methods. These methods are based on a rock mass classification method, the 'Coal Mine Roof Rating' (CMRR), developed for geomechanical rating of the roof strata in longwall coal mines (Molinda & Mark 1994). ALPS was developed for the USA's coal mines and mainly for the panels with three gates in each side; whereas ALTS was developed for the Australian coal mines which have two gates in each side of the panels. In those methods design charts are constructed by statistical analyses of the data collected from industrial practices (Colwell et al. 2003; Mark et al. 2001). The estimated bolt load is based on the data collected in a limited number of sites. Such charts are limited in their ability to take into account the variety of rock conditions and mining sequences.

Analytical methods are mainly based on elasticity theory. They are appropriate for low-stress conditions in hard rocks. In such sites, it can be assumed that the rock behaves elastically.

Lawrence (2009) developed a hybrid numerical and empirical method to design rock-bolting in gates. A number of datasets regarding rock-bolting in Australian coal mines were collected and used to develop design charts. The method used simple elastic numerical simulations to account the stress concentrations in gates caused by longwall mining.

Numerical modelling can be used to investigate the stability of gates. However, the constitutive models and parameters used to simulate the behaviour of rock masses need to be carefully considered, (Jing & Hudson 2002). In addition, an appropriate algorithm is required for simulation of longwall mining and for consideration of the mining-induced disturbances in the stability analyses. In practice, however, the design results have to be supported by field observations (Habbelwhite & Lu 2004; Frith 2000).

2.5 Chain pillars for longwall panels

Chain pillars are subjected to a complex loading path throughout their service life and, therefore, their design is not as straightforward as that of room-and-pillar method. The chain pillars are loaded: during the construction of the gates, mining the first adjacent panel and later on during mining of the second adjacent panel. The chain pillar located close to the longwall face has its highest vertical load since its construction (Brady & Brown 2002). The width of the chain pillars varies from 20 to more than 100 m, depending on their depth, in-situ stress, mine layout and the mass strength of the coal materials. Moreover, the pillars are designed for more than just pillar stability. They are also designed to maintain the serviceability of the gates and maximise coal recovery (Colwell et al. 1999). Designing the pillars requires calculation of their loading and strength. The factor of safety is calculated by dividing the pillar strength by the pillar load.

Analytical, empirical and numerical methods have been developed to estimate the mining-induced load of pillars. Analytical methods, e.g. those of Salamon (1964) and Wilson (1982), assume elastic homogeneous media. Mark (1992) used modified tributary area theory by assuming an abutment angle, which represents the angle of the overhang rocks from the pillar edge, to obtain the chain pillar loading (Figure 2.7). His method is adapted in the ALTS and ALPS methods of pillar design. Field measurements and numerical modelling have revealed, however, that the constant abutment angle is not consistent with the reality (Mark & Chase 1997; Colwell et al. 1999). Heasley (1998) added the effect of stratification of the roof layers in calculation of the pillar loading. All of these methods assume the elastic behaviour of the rocks surrounding the longwall panels. They have not considered the effect of the horizontal stresses on the loading of the pillars. The major issue in calculating the loading of the pillars is to consider the dynamic nature of the roof strata cave-in and consolidation of the cave-in materials in the pillar load, factors which have not been taken into account in the above methods.

There are a number of formulas for evaluating the strength of coal pillars, e.g. Bieniawski (1968), Obert & Duval (1966) and Salamon & Munro (1967). These formulas mainly propose a nonlinear relationship between pillar strength and their width to height ratio. The formulas have a constant, which represents the strength of a cube of coal materials with unit dimensions. The equations have been implemented successfully in pillar design. There have been also a number of attempts to obtain pillar strength and post-failure modulus of pillars with numerical simulations (Mortazavi et al. 2009). The major element is a constitutive model for coal materials which must be able to govern the nonlinear post-peak behaviour of the coal.

The main methods of chain pillar design are ALPS (Mark et al. 1994, 2002) and ALTS (Mark et al. 1999), which use the CMRR value of the roof strata to evaluate a required factor of safety for the pillars and the roof supports. The pillar strength in these methods is obtained via the Bieniawski's pillar strength formula. The loading of the pillars is calculated by the tributary area theory by taking into account an abutment angle (Figure 2.7). The pillar loading changes, however, during mining of its two adjacent panels. Therefore, an empirical formula was also suggested in ALPS to find out the maximum load of a pillar during its service life. The factor of safety is calculated as the ratio of the pillar strength to the pillar load. Finally, the calculated factor of safety must be larger than that suggested by ALPS or ALTS for the CMRR value of the roof strata over the pillar.

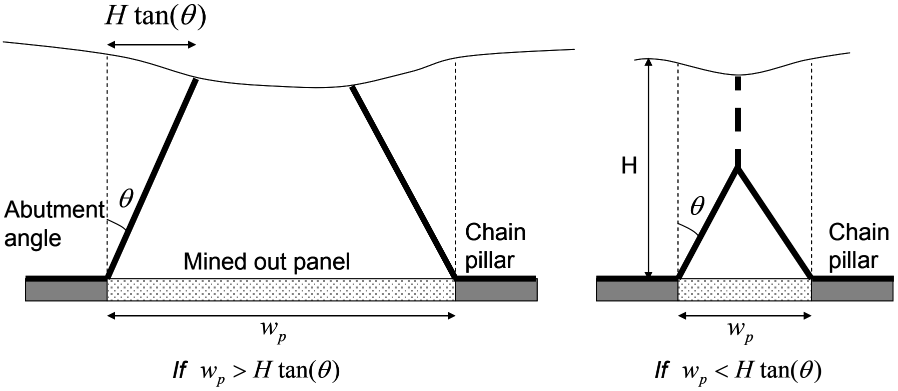

Figure 2.7 The side abutment load, after Mark et al (2001). *H* is the depth of a panel, w_p the width of panel and θ the abutment angle

When the pillar depth is more than 500 m, the mentioned methods suggest a large dimension for the pillars, which is not suitable. Large pillars can produce coal burst, bump and may also brick the roof strata and penetrate into the floor. Bader et al. (2002) showed that in this condition construction of yield pillars instead of the conventional chain pillars would be more successful. Yield pillars have a width to height ratio of three to five. The yield pillars are allowed to yield and it is tried out to mobilise their post peak strength to control the downward deformation of roof strata.

3 Study Site

3.1 Svea Nord Coal Mine

Svea Nord is one of the large coalmines in the arctic area. The mine is located at 78°N in the western part of Spitsbergen, Svalbard. The longwall mining method is used with an annual production of 3 million tonnes of coal. Longwall panels are approximately 250 m wide and 2500 m long. The overburden of the panels varies from 10 to 400 m. In addition, most of the ground surface is covered by glaciers, with an ice thickness of up to 250 m in the mine area. Figure 3.1 shows the mine map.

Two gates are parallel excavated for every panel. The rock party between the two gates is the so-called chain pillar, which is 40 m wide. Crosscuts are excavated in the chain pillar about every 75 m between the two adjacent gates.

There exist a number of inverse faults with strikes that are approximately perpendicular to the major in-situ principal stress σ_1. The persistence of the faults is limited such that they do not jeopardise the stability of the mine.

Figure 3.2 shows the vertical geological column in the study site, which is constructed based on core logging. The roof stratum is composed of siltstone and finely grained sandstone that contains thin interlayers of coal and bentonite. A bentonite seam is 2-3 m above the coal seam. The roof rocks may be roughly divided into three units. Unit 1 contains the rock party from 0 to 2.5 m in the roof and is composed of siltstone with thin coal interlayers. A layer of bentonite is the upper limit of this unit. Unit 2 refers to the party from 2.5 to 10 m in the roof and is composed of sandstone and siltstone with coal interlayers. This unit is capped by a thin coal layer. Unit 3 is the rock party above 10 m and is mainly composed of sandstone and siltstone.

Mechanical and physical properties of the intact rocks of the mine were obtained by laboratory tests, which are summarised in table 3.1. Rock mass classification methods are adapted to obtain the rock mass properties. The representative values of GSI (Ground strength Index, Hoek & Brown 1998) for the mining area were used to obtain the rock mass properties, table 3.2. However, recently Barton & Pandey (2011) argued about the limitations of the GSI method in characterising of the rock masses, and they showed that Q_c method, developed by Barton (2002), is an appropriate method to obtain the rock mass characteristics. The author's investigations at the study site have showed that the suggested values for cohesion and friction of the rock masses are fairly similar by those two methods (Table 3.3). However, the rock mass cohesion suggested by Q_c is higher than the one obtained by the GSI method.

Table 3-1: Mechanical properties of the intact rocks in the study site

Rock type	Uniaxial compressive strength	Young's modulus	Poisson's ratio	Cohesion (MPa)	Friction angle (Deg.)
Coal	30	6	0.4	6	46
Siltstone	60	25	0.24	12	45
Sandstone	100	35	0.175	18	49

When in the numerical modelling it is required to deal with the strength degradation in rocks, e.g. in modelling of pillars and strata fracturing, it would be required to use nonlinear constitutive models to capture the post peak behaviour of the rocks (Mortazavi et al. 2009). Therefore, in the numerical simulations a strain softening constitutive model was used. Obtaining of the strain softening parameters of the rock masses still is not clear. However, recently with advance of stochastical and statistical methods for the rock mass characterisation, a method is developed denoted as synthetic rock mass model (Ivars et al. 2011). This method could be used to obtain the strain softening properties of rock masses. However, it is very time consuming and needs a large number of data collected from the site in order to make statistical model of the rock discontinuities. Another method has proposed by Cai et al. (2007) for the hard rocks. They assumed that the strength degradation is due to that the rock discontinuities lose their frictional resistance because of the asperity failure. However, in the weak rocks the strain softening behaviour is related to both the strength reduction of rock discontinuities and intact rock fracturing. Moreover, the intact rock failure is scale dependent which could change by the size of the blocks composing the rock mass.

Table 3-2: Mechanical and physical parameters of the rock mass*.

Rock Mass	Coal	Sandstone	Siltstone
K (GPa)	2.33	6.8	5.3
G (GPa)	0.5	5.1	3.2
c (MPa)	1.06	2.8	1.9
ϕ (Deg.)	29	49	37
σ_t (MPa)	0.033	0.28	0.42
$c_r(MPa)$	0.0106	0.28	0.19
ϕ_r (Deg.)	29	30	30
e_p(%)	0.5	0.05	0.05

*K is the bulk modulus, G the shear modulus, c the cohesion, ϕ the internal friction, σ_t the tensile strength, c_r the residual cohesion, ϕ_r the residual friction and e_p the plastic strain parameter at the residual strength.

Table 3-3: Mechanical properties of the rock masses obtained by the Qc method (Barton 2002)

Rock Mass	Coal	Sandstone	Siltstone
c (MPa)	1	6	4.5
ϕ (Deg.)	30	45	40

In this research a strain softening constitutive model developed for FLAC$^{(3D)}$ is used to simulate the strain-softening behaviour of the rocks and it was assumed that the rocks behave relatively brittle. Based on the suggestions by Hoek (2007) and Hajabdolmajid at al. (2002) the residual cohesion of the rocks is assumed to be almost 10% of its peak while the friction angle decreases to the basic friction angle of the rocks. A small amount of shear-strain parameter is used to simulate brittle fracturing of the rocks (Table 3.2).

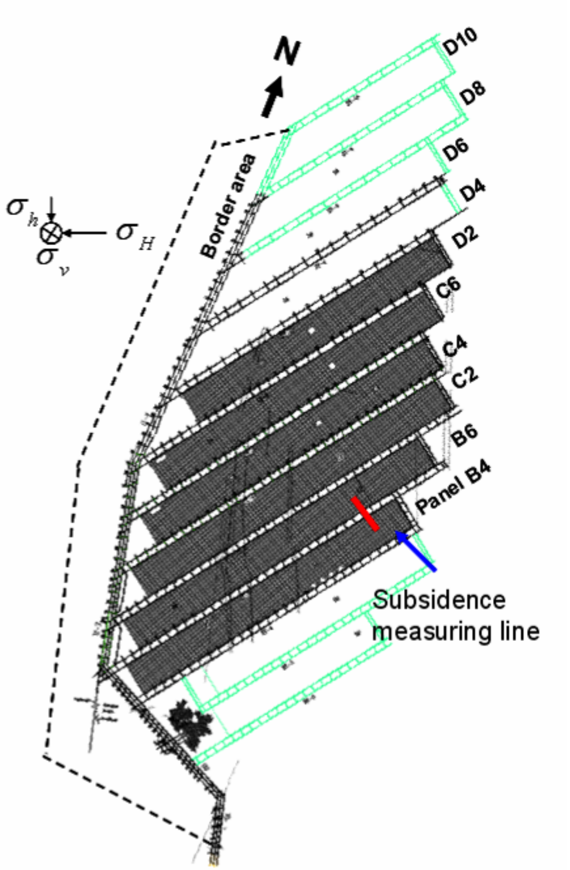

Figure 3.1 Mine map.

The rock mass is generally dry in the mining region, except in the caved region, which is penetrated by a limited amount of glacier-thawing water. Water is not a significant issue in the mine.

The ground subsidence was measured along the line drawn in Figure 3.1. The measurement was started when the first southern panel of the mine, Panel B4, has been mined out and it was continued during mining of the second southern panel of the mine (Hansen 2004). The maximum subsidence was 1.8 m at the northern end of the line.

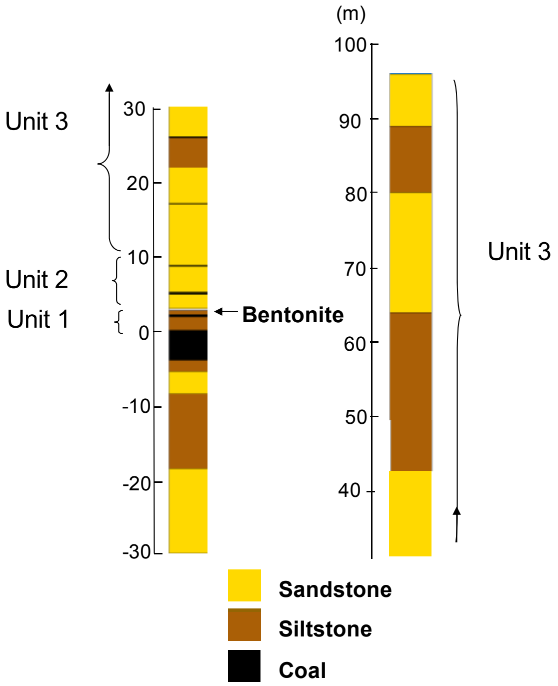

Figure 3.2 Geological column at the study site

3.2 *In-situ stress measurements at the study site*

In-situ rock stresses were measured in 6 locations in the mine using the overcoring relief method. The measurements show that both the major and the moderate principal stresses are horizontal. All the measurements are conducted in the roof of the gates at the stretch of 4 m from the gate roof. The measurements are conducted in the stress disturbed zones at the roof of the gates. Therefore, 6 elastic numerical modelling was conducted with a finite element code, Phase2, in order to find the magnitude of the original in-situ stresses.

The major principal stress σ_1 is approximately parallel to the longwall panels, while the moderate stress σ_2 is perpendicular to it, a deviation of about 15-20 degree, Figure 3.1. The minor principal stress σ_3 is vertical and equal to the weight of the overburden. The magnitudes of the maximum and minimum horizontal principal stresses at the coal seam level are about σ_1=10 MPa and σ_2=8 MPa.

3.3 Stress changes due to longwall mining

In the study site, a monitoring station was installed in gate CT8-B, 20 m inby the cross cut Tr-20, Figure 3.3. A doorstopper cell was installed in the middle of the gate and in 4 m above the roof to measure changes in the horizontal stresses during mining of panel C6. Monitoring was conducted in the entire period of mining in panel C6.

Figure 3.4 presents changes of the horizontal stresses in directions parallel ($\Delta\sigma_{xx}$) and perpendicular ($\Delta\sigma_{yy}$) to panel C6. The stress changes were plotted versus the position of the stope face in panel C6 with respect to the monitoring station. Increase in the compressive stresses is positive and decrease is negative in the plots. The measurements of the stress changes in the monitoring station were conducted in long distance intervals until the stope face reached the station. Thus, it is uncertain on the reliability of the measurement results and what looked like between the measurement points. The measurement points before the face reached the station are connected with dashed lines in Figure 3.4.

The stress increment in the direction parallel to the gate, $\Delta\sigma_{xx}$, started to increase when the longwall face was in a distance of about 200 m to the monitoring station. The maximum increment, 0.35 MPa, was reached when the stope face had passed the monitoring station of about 30 m. At this distance the roof strata behind the longwall face started to cave. The roof cave-in resulted in that stress increment. $\Delta\sigma_{xx}$ decreased gradually with increase in the distance from the face. $\Delta\sigma_{xx}$ finally stabilized at a level of about 0.1 MPa when the stope face passed the monitoring station about 300 m.

The stress change in the direction perpendicular to the gates, $\Delta\sigma_{yy}$, is reduction. The stress decrement, $\Delta\sigma_{yy}$, had already reached about 0.85 MPa when the longwall face was in a distance of 200 m to the monitoring station. $\Delta\sigma_{yy}$ stabilized at about -1 MPa after the stope face passed the monitoring station.

The monitoring results indicate that the horizontal stresses became stabilized in approximately 300 m after that stope face passed the monitoring station. This may be the distance in which the caved material reaches its maximum consolidation. The stress changes are very small compare to the original in-situ rock stresses which are σ_{xx} =10 MPa and σ_{yy}=8 MPa. It implies that the chain pillar might play a role in reduction stress changes in the host rock.

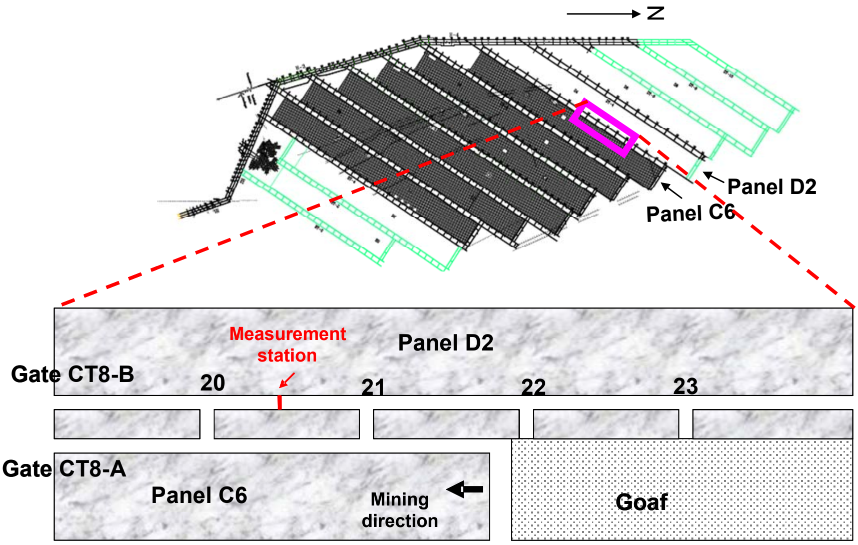

Figure 3.3 The location of the monitoring station for the measuring longwall induced stress changes

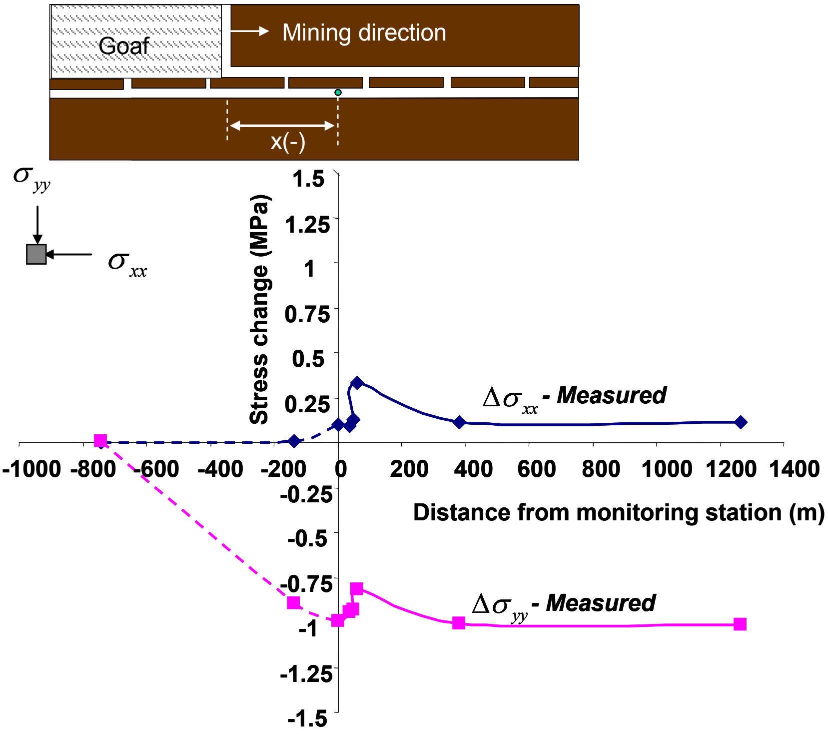

Figure 3.4 In-situ measurement of the horizontal stress changes by stope face advance

3.4 Bolt load measurements at a gate

A measurement station was set up about 30 m from crosscut 7 in gate CT8-B (Figure 3.5). Strain-gauge instrumented rock bolts were installed in the roof of the gate. The bolts were 2.5 m long. The strain gauges on all the instrumented bolts except on bolts 5 and 6 became damaged shortly after installation. Thus, only measurement data for bolts 5 and 6 are available for analysis. The instrumented bolts were installed when the excavation face of gate CT8-B was about 10 m from the station. Measurements started immediately after the bolt installation and lasted throughout the excavation of gate CT8-B and mining of the entire panel C6 until the longwall front of panel D2 reached the measurement station. Figs. 3.6 and 3.7 show the axial loads and bending moments measured in the two of the installed bolts at different excavation stages.

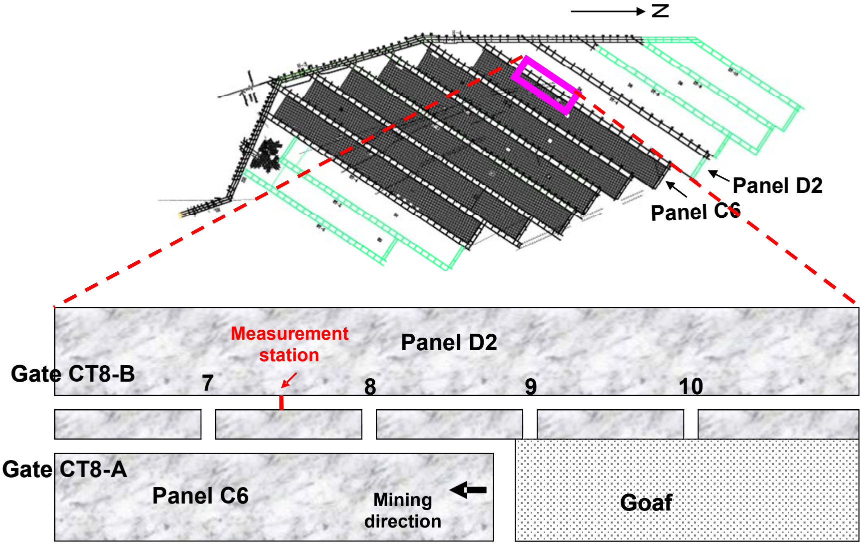

Figure 3.5 A monitoring station to measure bolt load changes by stope face advance.

It is seen in the figures that the bolt load and the bending moment are mainly built up during excavation of the gate. Afterwards, they did not change much over the course of the mining in panel D2. They started to change only when the longwall front reached a distance of about 300 m to the measurement station. However, the changes were not considerable until the distance was shorter than 20 m. The bolt load refers to the pull load subjected to the bolt, while the bending moment is a measure of the shear load laterally applied to the bolt. The measurement data show that the bolts were generally loaded both axially and laterally along their lengths. This fact implies that both rock dilation and shear moments between bedding planes occurred in the rock mass.

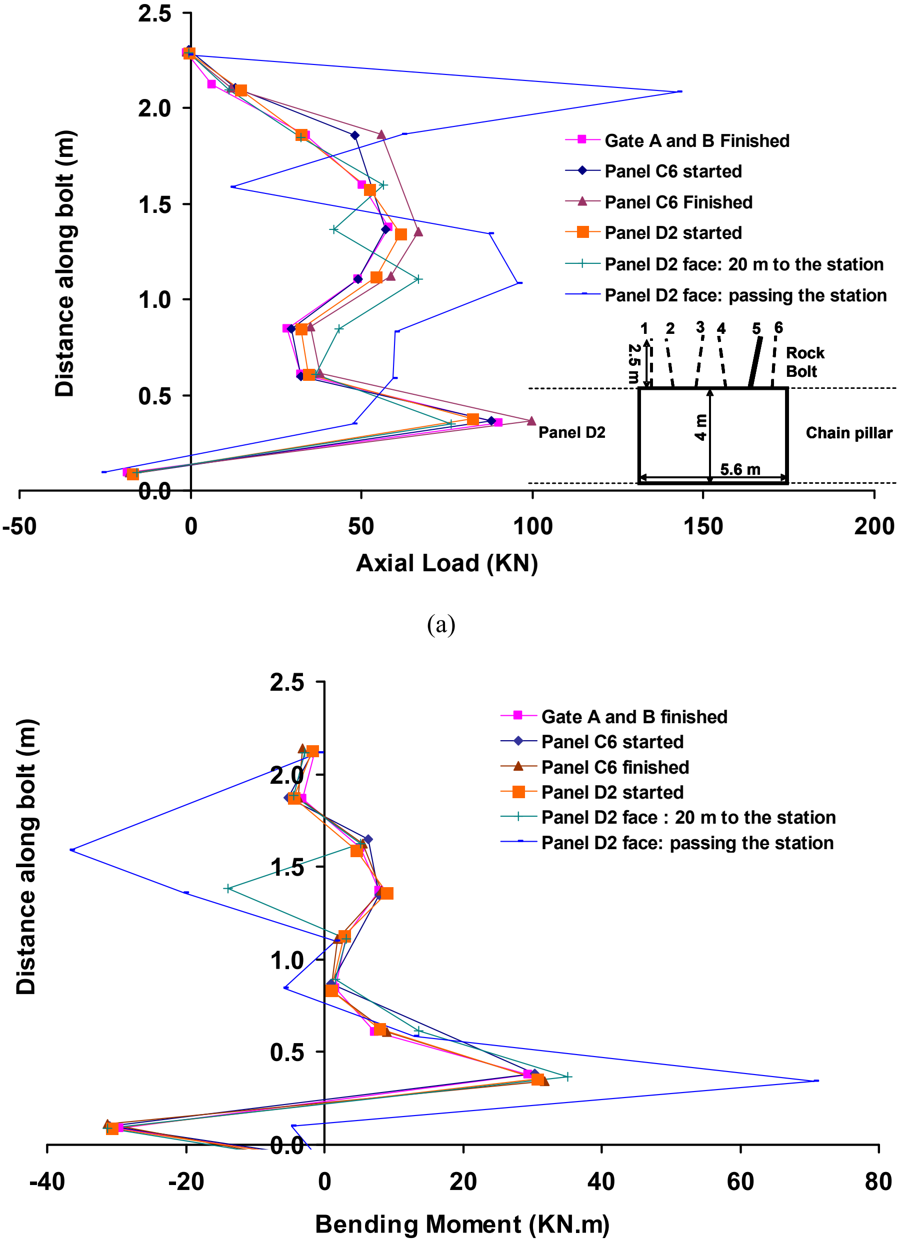

(a)

(b)

Figure 3.6 Distribution of the axial load and the bending moment along rock bolt 5: (a) axial load, (b) bending moment.

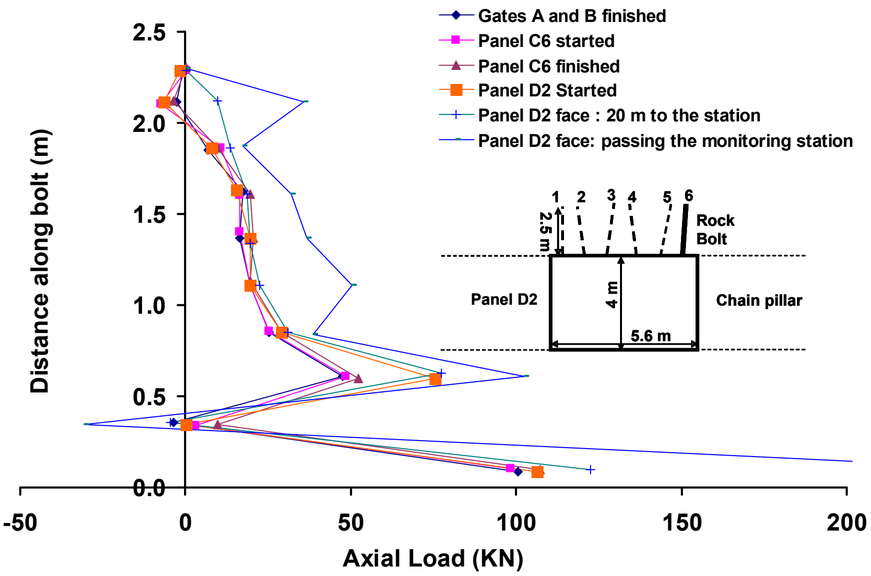

(a)

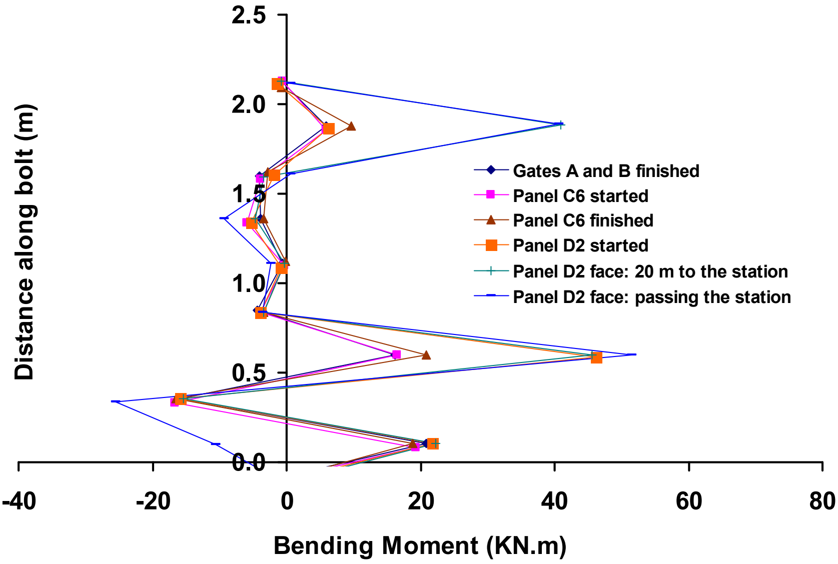

(b)

Figure 3.7 Distribution of the axial load and the bending moment along rock bolt 6: (a) axial load, (b) bending moment.

4 Numerical modelling of longwall mining

4.1 Introduction

The main issue in numerical modelling of longwall mining is how to consider the progressive roof cave-in and fracturing and consolidation of the cave-in materials due to weight of the overburden rocks. The dynamic nature of the roof cave-in makes numerical modelling of longwall mining a challenging job.

Many attempted to numerically model longwall mining in the past years. In those attempts, empirical methods, the parameter of bulking factor and field measurements were employed to estimate the height of the cave-in zone. Whittles et al. (2006) employed an empirical method to estimate the height of the cave-in zone above a mined-out panel. The empirical method was developed by Bai et al. (1995) based on data collected in coal mines in China and USA regarding changes in the hydraulic conductivity of the rocks surrounding the mined-out panels. Trueman (1990a and b) and Thin et al. (1993) used the bulking factor concept to find the height of the cave-in zone. The bulking factor is implemented to find out a boundary in the roof under which the cave-in rocks fully fill the stope voids. Wargle (1993) reported a trial to measure the height of the cave-in zone by borehole drilling from the mine surface to the goaf.

Roof cave-in is a progressive process which starts at a critical distance behind the stope face and develops upward in the roof strata with face advance. Cave-in ceases when the volume of the cave-in materials is large enough to fully fill the stope void. All the methods mentioned above, i.e. empirical method, bulking factor method and drilling method, can be used to find out the maximum height of the cave-in zone. However, numerical modelling is an appropriate approach to assess the dynamic stress state around a longwall face. Moreover, roof strata cave-in not only depends on the geomechanical characteristics of the roof strata, but also is associated with the height of the stope and the location of the bedding planes at the roof. In other words, it is strongly site dependent.

Another issue in modelling of longwall mining is choosing a proper constitutive model to simulate the consolidation of the cave-in materials under the weight of the overburden rocks. Trueman (1990a and b) implemented a modified stress-strain relationship of a stone-built pack and assumed a maximum volumetric strain of 0.33 for consolidation. Thin et al. (1993) used the double-yield constitutive model of FLAC^{2D} code to simulate the consolidation of the cave-in materials. They applied the stress-strain relationship by Trueman (1990a and b) to calculate the parameters of the double-yield model. The double-yield constitutive model was also used for cave-in materials in the study reported in this thesis. In this study a back-calculation approach was applied to assess the parameters of the double-yield model for cave-in materials.

This chapter presents a novel numerical simulation algorithm to model the longwall mining in the Svea Nord mine. A finite difference numerical code, FLAC^{3D}, is used for simulations. A strain-softening constitutive model is used to simulate the nonlinear behaviour of the rock masses. Back-calculation is used to obtain the required rock mass parameters of the developed algorithm. The numerical model, then, is calibrated by comparing of its results with the field measurement data of bolt loads and stress changes at the gate roof with longwall face advance.

4.2 Developing an algorithm for numerical modelling of longwall mining

Cave-in is different from yield in a mechanical sense. Yield means that the rock is subjected to failure because the stress exceeds the rock strength. Cave-in refers to the disintegration of failed rock pieces, which then move downward because of the gravity.

Singh and Singh (2009) numerically studied the ground pressure on the hydraulic shields next to the longwall face. The criterion for identifying the cave-in rocks in their study is a shear strain of 0.25 or a downward displacement of 1 m. In reality, it is not necessary that rock fails in shear in the case of cave-in. In reality, rock is more than often subjected to tensile failure when cave-in occurs. In addition, the vertical displacement of the cave-in body is associated with the size of the stope void. Therefore, neither shear strain nor the downward displacement is appropriate as a cave-in criterion. In the cave-in area, rock slabs separate from the host rock and move downward. The maximum principal plastic strain ε_1^p (in tension) should be an appropriate parameter to outline the boundary of the cave-in zone. In the plasticity theory, the total maximum principal strain ε_1^t is defined as (ITASCA 2010):

$$\varepsilon_1^t = \varepsilon_1^e + \varepsilon_1^p \tag{4.1}$$

where ε_1^e is the maximum principal elastic strain and ε_1^p is the maximum principal plastic strain. In the cave-in zone the rock mass yields in tension. The tension strength of the coal rock is very small. The plastic strain is usually much larger than the elastic strain in the cave-in zone, $\varepsilon_1^p >> \varepsilon_1^e$. Therefore, it can be said that the total principal strain is approximately equal to the plastic strain, $\varepsilon_1^t \approx \varepsilon_1^p$. The maximum tensile strain in the roof strata before they cave in is denoted as the critical cave-in strain (ε^c). This critical value is used to identify the cave-in boundary. The roof strata is said to be caving in if

$$\varepsilon_1^t \geq \varepsilon^C \tag{4.2}$$

The bulking factor (BF) is a parameter that represents the dilation of the rock after cave-in. Site investigations in coalmines show that the bulking factor of coal rocks is in a range of 1.1-1.5 (Peng & Chiang 1984). Several studies have proved that the porosity of cave-in materials is approximately 0.3 (Mark & Piers 2009; Brown 2003). This porosity corresponds to a bulking factor of 1.43. In this study, the bulking factor is used to determine whether the stope voids are fully filled by cave-in materials. A bulking factor of 1.43 refers to the stope being fully filled. The stope is not fully filled for BF > 1.43, and the cave-in material is under consolidation for BF < 1.43. The bulking factor can be estimated by taking into account the change in the size of the cave-in zone with respect to the height of the stope:

$$BF = \frac{h_c + h_{cr}}{h_{cr}} \tag{4.3}$$

where h_c is the stope height and h_{cr} is the thickness of the cave-in zone in the roof.

Knowledge of the consolidation behaviour of the cave-in material is limited owing to the inaccessibility of the goaf (Wargle 1993). Pappas & Mark (1993) conducted laboratory compressive tests to study the consolidation of loose materials. They claimed that Salamon's formula (1999) is valid for cave-in materials:

$$\sigma = \frac{E_0 \varepsilon_v}{1 - \varepsilon_v / \varepsilon_v^m} \tag{4.4}$$

where σ is the applied compressive stress to the loose material while the material is rigidly confined laterally, E_0 is the initial tangential modulus of the material, ε_v is the volumetric strain and ε_v^m is the maximum volumetric strain. ε_v^m can be obtained from the bulking factor (Yavuz 2004):

$$\varepsilon_v^m = \frac{BF - 1}{BF} \tag{4.5}$$

A strain-softening constitutive law is assigned to the rock mass in the simulations. The rock experiences a path of unloading-reloading in the fracture zone. The stresses in the fracture zone decrease during cave-in. After cave-in ceases, consolidation of the cave-in materials starts. The stresses at the fracture zone increase again in the consolidation period. The deformation modulus of the rock mass is reduced in the post-failure stage because of the created fractures. In this study, fracturing of the rock above the cave-in zone is taken into account by using a residual strength and a reduced deformation modulus in the models.

The double-yield constitutive model is used to simulate the consolidation of the cave-in materials. The mechanical properties of the rock in the cave-in and fracture zones are calculated by back-calculating the subsidence data measured on the ground surface above the mine. Salamon's formula (Eq. 4.4) is used to calculate the cap pressure parameters. The back calculation method is presented in the next section.

An algorithm was developed for the numerical simulation of the cave-in and mining process in accordance with the scenario proposed by Peng & Chiang (1984) (Figure 2.3). The height of the longwall stope is denoted as h_c. The first cave-in event occurs when the length of the open stope reaches l_p. The cave-in rock has a constant thickness of b in the middle of the cave-in zone, while the thickness decreases approaching the longwall front, which results in a concave roof formed by cantilever beams of laminated rock behind the longwall front. With a critical advance of l_s, the cantilever beams break and fall down. Cave-in occurs repeatedly with every advance of l_s until the panel is completed. The calculation results show that the thickness of the cave-in roof is constant regardless of whether the cave-in occurs for the first time or during the sequential excavations.

In the proposed algorithm, it is assumed that the roof convergence ceases when the roof of the stope meets the floor. The upper boundary of the cave-in zone is then determined with the criterion described above in Eq. 4.2. Until this moment, the cave-in materials are loose and do not bear any stress. The volume of the cave-in rocks is checked whether it is large enough to fully fill the stope voids. Caving in ceases when BF ≤ 1.43. Afterward, the loose materials are compacted and consolidated in the cave-in zone due to the inward deformation of the surrounding rock mass. The fracture zone is defined as the failed rock masses above the cave-in zone.

Figure 4.1 is a flowchart for the simulation of the mining and cave-in processes. The longwall mining starts with advance of 5 m every time in the beginning. The calculation steps 100 cycles after every excavation round. The unbalanced force ratio in the model is then checked to see whether equilibrium has been reached. A further 100 calculation cycles are run if the unbalanced force ratio is larger than 10^{-5} and the maximum vertical roof displacement is smaller than the stope height. This iteration continues until the unbalanced force ratio becomes less than 10^{-5}, and then, a further excavation advance is performed. The iteration ceases when the maximum vertical displacement of the stope roof, d_z^{max}, is equal to the height of the stope void, h_c. The roof of the stope void has met the floor when $d_z^{max} \geq h_c$. The boundary of the cave-in zone is then identified by the criterion of $\varepsilon_l^t = \varepsilon^c$. The mesh elements of the model in the cave-in zone are nulled, that is, the relevant mechanical properties in the mesh elements are assigned with zero values when the bulking factor, BF, of the cave-in materials is larger than 1.43. Bulking factor is calculated by Eq. 4.3. The BF is infinitive before cave-in occurs and gradually declines with the upward extension of the cave-in zone. In the numerical modelling, calculation iterations are carried out and the bulking factor is checked. Excavation advances until the bulking factor reaches 1.43, which indicates that the cave-in materials have fully filled the mined-out void underneath and the cave-in process stops. From now on the cave-in materials will be consolidated under the pressure of the strata above. A double-yield material model is used for simulating the consolidation of the cave-in materials. Accordingly, the mechanical properties of the nulled mesh elements of the model in the stope voids with $BF \leq 1.43$ are changed to the double-yield model. The elastic properties, i.e., the Young's modulus and Poisson's ratio, of the rock mass in the fracture zone are then reduced for a certain amount from their original values. At this moment, the critical cave-in length l_p and the thickness, b, of the cave-in strata are determined. After that, a similar excavation process is done to find the critical advance length l_s at which subsequent cave-in events occur. Finally, the longwall face advances a length of l_s every time and calculation iterations are carried out to update the boundary of the cave-in zone and the bulking factor. This process continues until the entire panel is mined out.

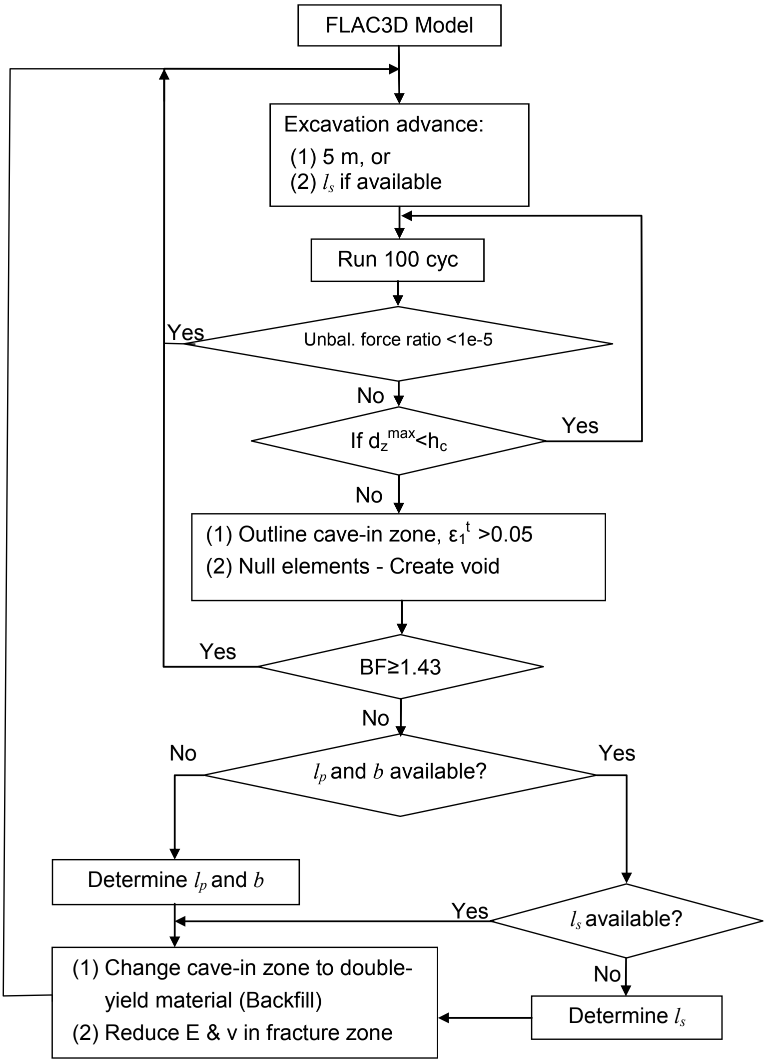

Figure 4.1 An algorithm for numerical modelling of longwall mining with FLAC$^{(3D)}$.

4.2.1 Back-calculating of cave-in strain

The critical cave-in strain, ε^c, was used in the algorithm to outline the border of the cave-in zone. It represents the maximum value of the extension strain that the roof strata could sustain before cave-in. The critical strain ε^c depends on the quality of the roof strata, the thickness of the each stratum and the stress state. There are no straight forward methods to obtain ε^c. Back-calculation of measurement data is the most reliable way to do it. In the study site, the ground subsidence was once measured in the location marked in Figure 3.1. The subsidence data along the measurement profile was adopted to back-calculate the critical strain ε^c and the mechanical properties for the cave-in and fracture zones.

It is recommended that the acceptable range of the critical strain should be pre-defined for back-calculations (Orest 2005). Coal rocks have low ultimate tensile strains. Therefore, it was assumed that the critical strain of the rock strata in question is less than 10% in the back-calculations.

The consolidation of the cave-in materials is simulated by using the double-yield constitutive model. The cohesion of the cave-in materials is assumed zero and their inherent basic friction angle is about 30 degree. The cap pressure and the maximum volumetric strain were calculated with the Eqs. 4.4 and 4.5, respectively. The initial tangential modulus of the cave-in materials (E_0 in Eq. 4.4) was obtained by back-calculation. Laboratory compressive tests of the cave-in materials revealed that the initial tangential modulus of the cave-in materials with considering the compressive strength of the roof strata is about 80 MPa (Pappas & Mark 1993; Yavuz 2004). In the back calculations it was assumed 60 MPa $\leq E_0 \leq$ 100 MPa.

The E modulus of fractured rocks above a cave-in zone is assumed about 500 MPa (Tajdus 2009). In our back-calculations the E modulus was limited to a range larger than the initial tangential modulus of the cave-in rocks and smaller than 500 MPa i.e. $E_0 < E \leq 500$ MPa. The Poisson's ratio of the fractured rocks was assumed 0.3 (Hoek 2001).

The numerical simulation code of FLAC^{3D} was used in the back-calculations. The shape and the boundary conditions of the model are similar to the one shown in Figure 4.2. However, the model has a dimension of 1000 ×300 ×400 m (length × width × height). In addition, Panel 1 and 2 in Figure 4.2 represent panels B4 and B6 and gate A and B represent gates BT6-A and B, respectively. The model at the coal seam level has the mesh size of 2×1×1 m in X,Y and Z directions, respectively. The mesh size in the roof and floor strata increases with increasing of the distance from the coal seam. Generally the mesh size in the roof and floor strata is between 2×1×1 to 4×4×4 m in X,Y and Z directions, respectively. The roof and floor strata are simulated in the model based on the geological column of the study site, Figure 3.2. The bedding planes and the sandwiched coal and bentonite interlayers are simulated as the discontinuities in the model. The mechanical properties of the rock masses and the discontinuities assigned to the model are presented in tables 3.2 and 4.1, respectively. The in-situ stress filed is included in the model same as the field measurements since their directions have a small deviation with x,y and z directions of the model. After initiating of the in-situ equilibrium in the model and excavation of the gates, the longwall mining process was simulated according to the algorithm shown in Figure 4.1.

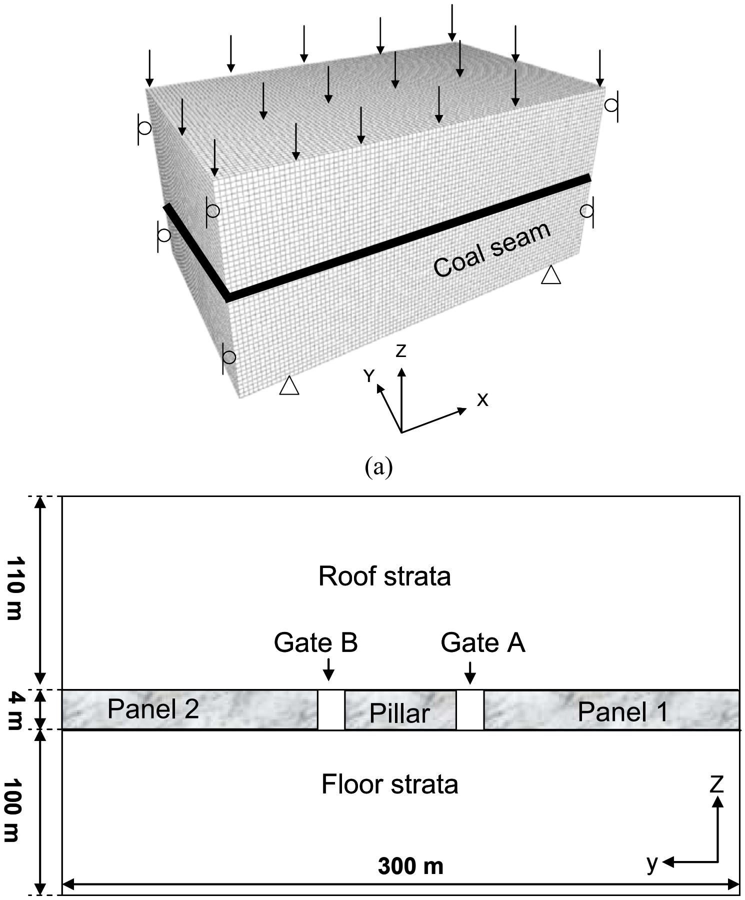

Figure 4.2 (a) The three-dimensional model. (b) Vertical cross section in the Y-Z plane.

Table 4-1: Mechanical properties of the discontinuities used in the numerical models.

Discontinuity	Cohesion (MPa)	Friction (Deg.)	Tensile strength (MPa)
Bedding	0.3	30	0.03
Thin coal interlayer	0.3	30	0.1
Bentonite interlayer	0.5	25	0.4

In the simulations, three E-modulus values were assumed for each of the cave-in zone and the fracture zone. For the cave-in rock, they are E_0 = 50, 80 and 100 MPa and for the fractured rock E = 100, 200 or 400 MPa. The critical strains for the trials are ε^c = 2%, 5% and 10%, respectively. It was found in the simulations that use of 10% for the critical strain resulted in unrealistic subsidence data so that it was disregarded in the subsequent simulations. The subsidence obtained for E_0 = 80 MPa are presented along the measurement line in Figure 4.3. In the figure the measurement data are also plotted for comparison. It is seen that the simulation result by using ε^c =5% and E = 160 MPa matches very well the measurement data.

The approved mechanical properties of the cave-in materials and fractured rocks are presented in table 4.2 and ε^c = 5% was chosen for the criterion to outline the border of the cave-in zone. A summary of the approved cave-in properties are presented in table 4.2.

Table 4-2: Mechanical properties of the cave-in and fracture zones.

Material	Constitutive model	Properties				
Cave-in material	Double-Yield	Cap pressure (MPa)	E_0 (MPa)	ε_m^v (%)	C (MPa)	Friction angle. (Deg.)
		$p = \frac{80\varepsilon_v}{1-\varepsilon_v/\varepsilon_m^v}$	80	0.3	0	30
Fracture zone	-	E (MPa)		v		
		160		0.3		

Note: ε_v is the volumetric strain; ε_v^m the maximum volumetric strain, P the cap pressure, *E_0* the initial tangential modulus, C the cohesion, E the Young's modulus and *v* the Poisson's ratio.

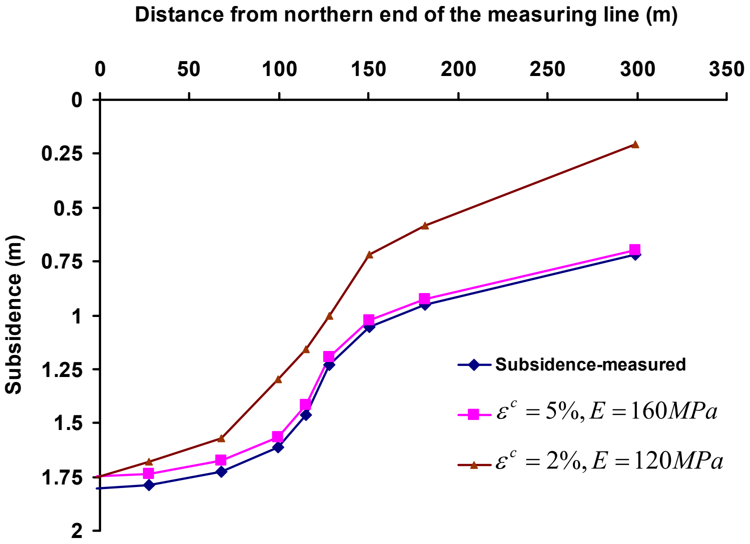

Figure 4.3 Ground subsidence profile for the group of the simulations with E_0=80 MPa and E= 120 and 160 MPa.

4.3 Verification of the numerical model

The proposed algorithm was implemented for the study site in the Svea Nord mine. The field measurement data obtained of the bolt load in the measuring station at gate CT8-B, between crosscuts 7 and 8 (Figure 3.5) and stress changes at the roof strata of the gate DT8-B, between crosscuts 20 and 21 (Figure 3.3) were used to verify the numerical models. The 3D FLAC model has dimensions of 1000 × 300 × 210 m (length × width × height). In the model, panels 1, 2 and gates A, B represent panels C6, D2, and gates CT8-A, B, respectively. The geometry and the boundary condition of the model are sketched in Figure 4.2. The roof strata are simulated based on the geological column at the study site presented in Figure 3.2. The profiles of the field measurement stations are included in the model. The overburden in the position of the measurement stations are about 110 m with a glacier of 250 m. A nonlinear strain-softening constitutive law was used for the rock mass. The mechanical and physical properties of the rock mass are presented in Table 3.2. Bedding planes and the sandwiched bentonite and coal interlayers are modelled as discontinuities in the model. The mechanical properties of the discontinuities and caved-in and fractured rocks are presented in Table 4.1 and 4.2, respectively. The mesh density and loading process of the model is same as the model presented in the section 4.2.1.

In the Svea-Nord mine, the longwall stopes usually start to cave in when the mined out distance reaches about 36 m. This figure is used to validate the model. The model is then used for the simulation of the entire mining process. Figure 4.4 shows the simulation results on the dimensions of the cave-in and fracture zones above the mining panel. It is seen that the first cave-in distance (l_p) is about 36 m in the 4-m-high longwall stope. The height of the cave-in zone increases from zero at the longwall front to about 16 m when the distance to the longwall front is beyond the cave-in distance (36 m). The fracture zone has a height of about 110 m in the cave-in area. It shows that the fracturing of the rocks would propagate to the ground surface in the shallow parts of the mine.

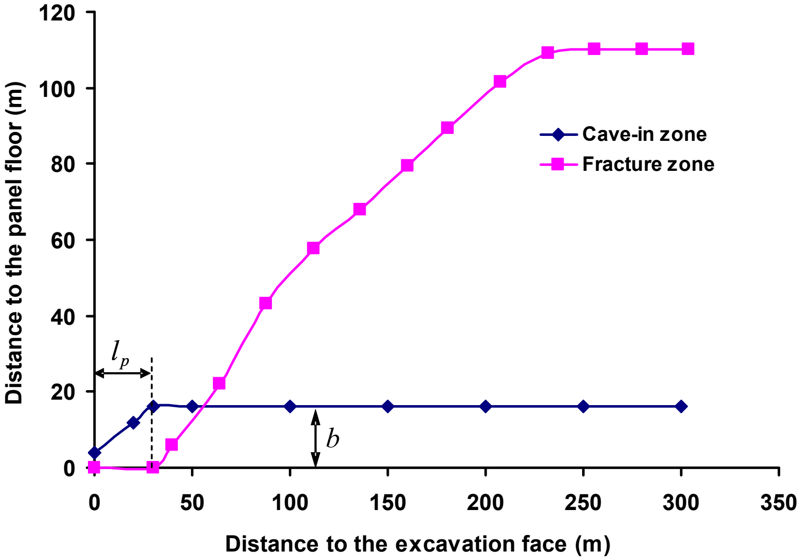

Figure 4.4 Height of the cave-in/fracture zone above the longwall panel

4.3.1 *Modelling of the bolt load*

We desired to compare the numerical modelling results of the bolt load with the in-situ measurement data obtained for gate CT8-B, between crosscuts 7 and 8 (Figure 3.5). The 3D model was too large for such detailed modelling. Therefore, a 2D model was established for this purpose. The 2D model was constructed in a vertical cross section in the Y-Z plane in the middle of the model where the in-situ measurement station was located (Figure 4.2). A plain strain condition must remain valid for 2D models. Three-dimensional modelling was conducted to check how the plain strain condition could be achieved when the 3D problem was simplified to a 2D problem. The modelling showed that the plain strain condition remains valid in the vertical cross section profile until the longwall front reaches about 20 m from the profile. The boundary conditions of the 2D model were identical to the 3D model except on the upper boundary, where a distribution of the vertical stress and in-plane shear stress is applied. The vertical and shear stress on the upper boundary change with the advance of the longwall front. It is determined in the 3D model and then applied to the 2D model.

Figure 4.5 shows the 2D model. The normal and shear stresses applied on the upper boundary of the model are different at different mining stages and are determined in the 3D model. They are presented in detail in Figure 4.6 for different mining stages. It is seen that the vertical stress is very low close to the chain pillar in panel C6, which is filled by cave-in materials. The stress approaches its original state at long distances from the chain pillar. A large stress elevation occurs in the chain pillar. The vertical stress increases gradually in panel D2 when the longwall front approaches the profile. The shear stress has its maximum above gate CT8-A and decreases with the distance apart from the gate.

The computer program Phase2 was used to run the 2D model. The physical and mechanical properties of the rock mass and discontinuities are identical to those in the 3D model (Table 3.2, 4.1 and 2). Mesh size in the phase2 model nearby the excavation surfaces is 0.5×0.5 m in the Y and Z directions, respectively, and larger meshes are assigned in the model for the locations far from the excavations.

A modelling sequence in the 2D models was adapted which could represent the original 3D modelling condition. In the model after initiating of the in-situ equilibrium, the gates are constructed. Then the mechanical properties of the cave-in and fracture zones above the panel C6 are changed to the desired values and stress distribution in the upper boundary of the model is changed to the values presented in Figure 4.6. Later on, modelling is continued just by changing of the stress distribution in the upper boundary of the model.

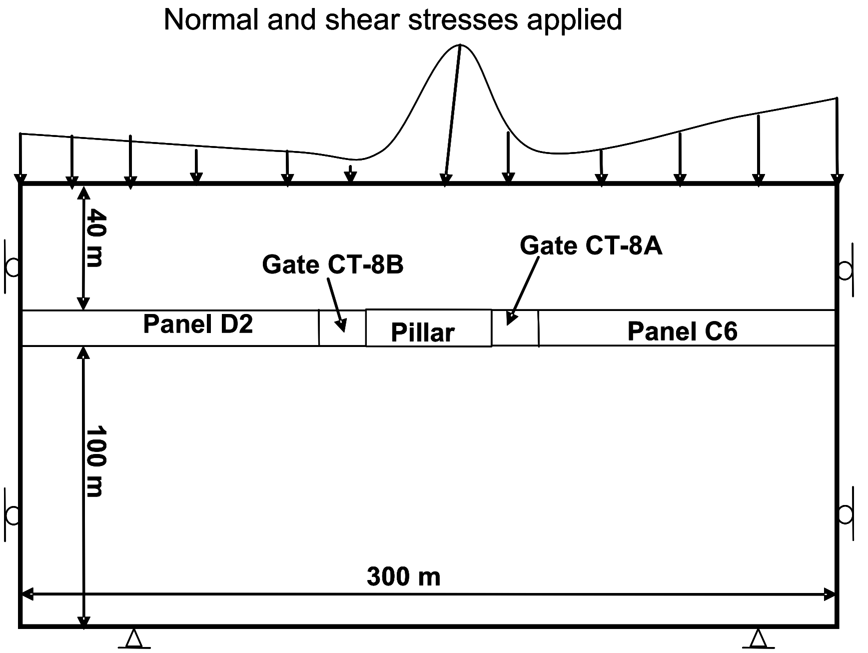

Figure 4.5 Geometry and boundary conditions of the two-dimensional model.

Table 4-3: Mechanical parameters of the rock bolts in the two-dimensional model*.

E (GPa)	d_b(mm)	Ultimate axial strength (KN)	Out of plane spacing
200	21.7	300	0.5

* E is the Young's modulus of the bolt material and d_b is the diameter of the bolt.

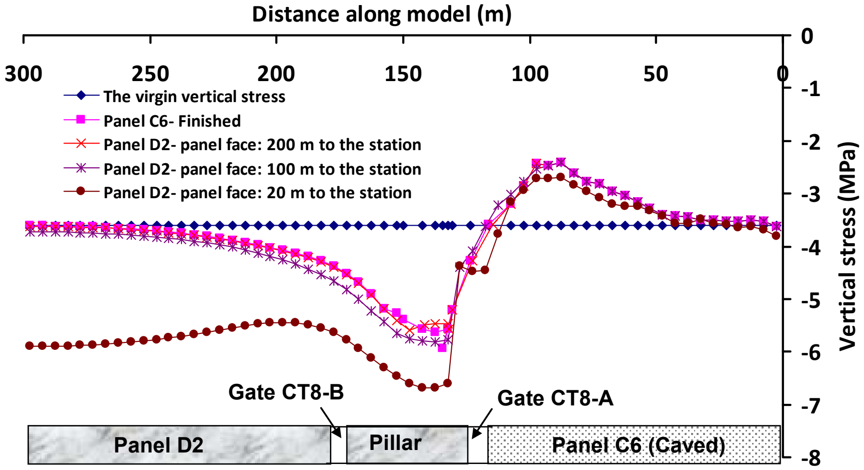

(a)

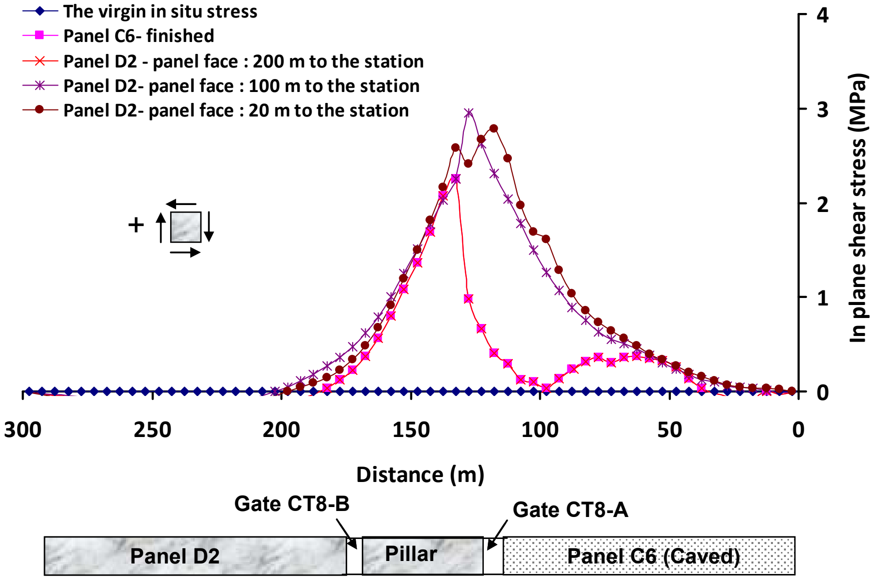

(b)

Figure 4.6 Stress distributions applied to the upper boundary of the two-dimensional model at different stages. (a) The vertical stress. Negative values indicate compressive stresses. (b) The horizontal in-plane shear stress.

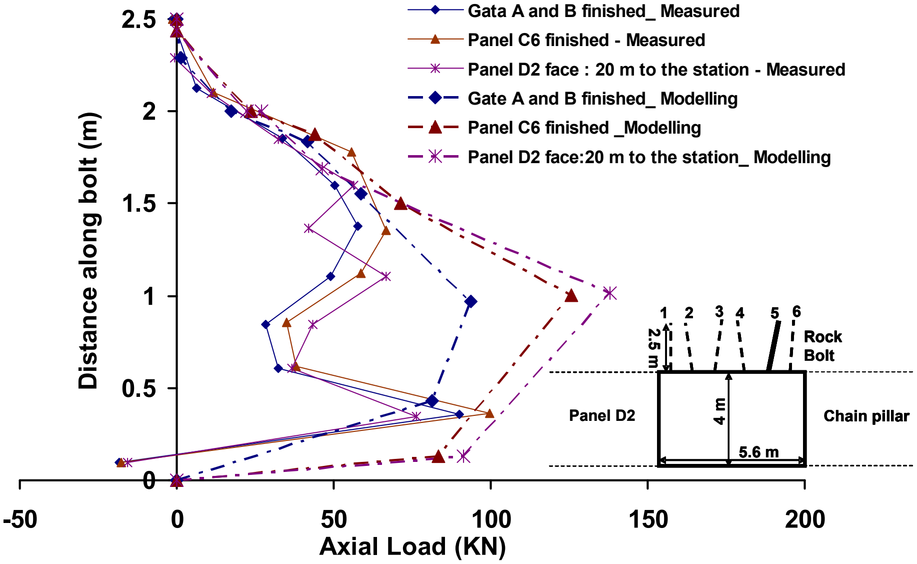

(a)

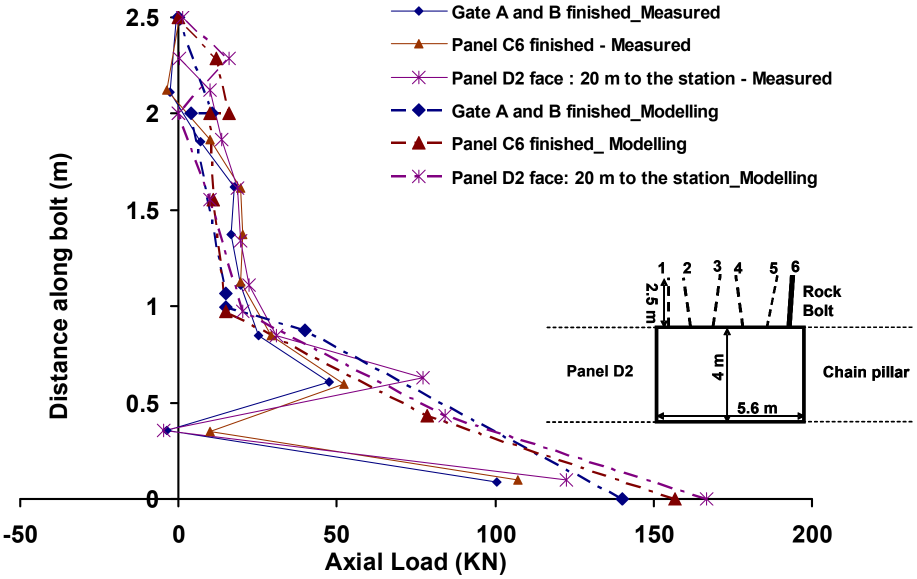

(b)

Figure 4.7 The numerical results of the bolt load in two rock bolts: (a) bolt 5, (b) bolt 6.

The bolts are simulated by fully bonded elements of the software. Their mechanical parameters are presented in Table 4.3. The modelling results of the axial load for bolts 5 and 6 are presented in Figure 4.7. In comparison to Figures 3.6 and 3.7 the modelling results are generally consistent with the measurement data. The modelling results deviate from the measurement results in the position close to the roof surface. The reason for this deviation may be that the model used a continuum material, while the real roof strata contain bedding planes. The discrete separations of the bedding planes may induce local high loads in the rock bolts. It is also observed in the numerical modelling that the axial load in the rock bolts is mainly built up during excavation of the main gate. The mining in the panels does not significantly change the bolt load.

4.3.2 Modelling of stress changes induced by longwall mining

The stress changes measured at the DT8-B, between crosscuts 20 and 21 (Figure 3.3), with longwall face advances in the panel C6 are used for verifying the numerical model. The stress changes obtained by numerical simulations and field measurement are presented in Figure 4.8.

The simulations show the stress change $\Delta\sigma_{xx}$ starts to increase when the stope face is in a distance of about 200 m to the station (Figure 4.8). A peak value of 0.4 MPa is reached when the stope face is in a distance of about 50 m to the station. After that, it decreases until the stope face passes the station. Then it rises again and reaches a maximum value of 0.6 MPa. It then decreases again because of caving of the roof strata. It finally stabilizes at a level of about 0.2 MPa when the stope face is in a distance of about 250 m from the monitoring station.

The simulated stress change $\Delta\sigma_{yy}$ increases rapidly when the stope face approaches the station and reaches a value of about 0.7 MPa just before the face passes the station (Figure 4.8). It drops then quickly to -1.4 MPa and gradually rebounds to about -0.75 MPa.

It is seen by comparing the measurement data and numerical results that the simulated stress change $\Delta\sigma_{xx}$ seems in a good agreement with the measurement data except just before the face reaches the monitoring station. A peak stress change occurs there in the simulation while there are no measurement data in that period. However, the simulated stress change $\Delta\sigma_{yy}$ deviates largely from the measurement data in the period before the stope face reaches the monitoring station. As pointed out previously, the measurement data before the face reached the station are too few. It is hard to assess the measurement data are true or false. On the basis of geomechanical assessment, it seems the simulated results are more reasonable than the measured data in that period. In general, the numerical results look acceptable in capturing the stress changes in the rock caused by excavation. They are in a relatively good agreement with the measurement data.

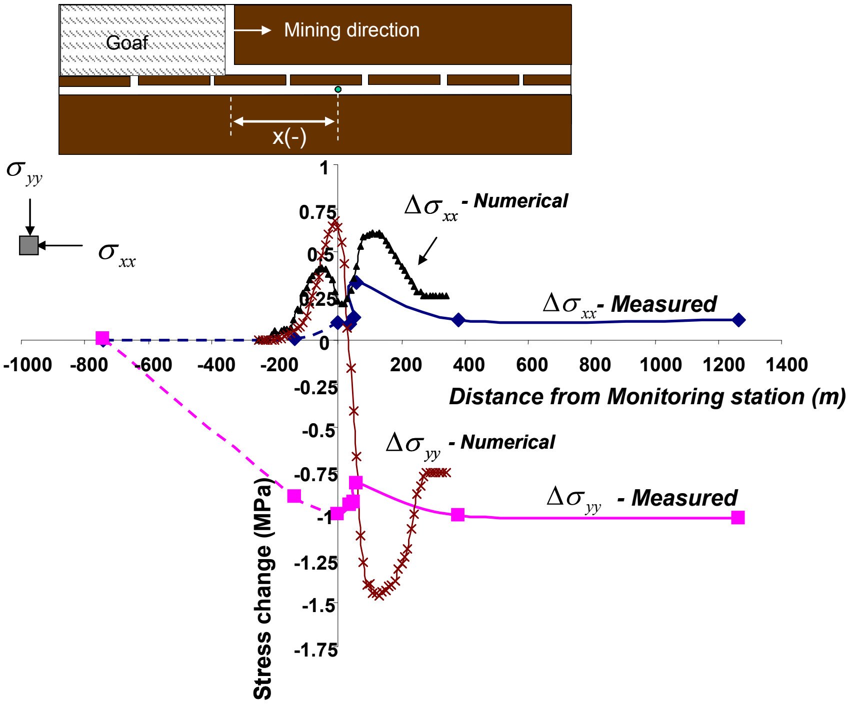

Figure 4.8 Numerically simulated and field measured changes of the horizontal stresses in the monitoring station

5 Stability analysis of the gates with numerical simulations

5.1 Introduction

As discussed in the chapter 2 the gates are constructed to serve the retreating longwall face. Stability and loading of the gate roof are actually associated with the longwall mining induced disturbances and dimension of the chain pillars. The width chain pillars would provide enough stability for the gates while decreases the recovery rate of the mine. The developed algorithm for numerical modelling of longwall mining allows us to model the dynamic roof strata cave-in process and longwall induced disturbance at the surrounding rocks. Therefore, it is an appropriate tool to investigate the stability of the gates. The numerical method was previously implemented to calculate the bolt load, installed at the roof of a gate, in the section 4.4.1 (using 3D simulation results to do detailed 2D simulations). In this chapter, also, same method was implemented to study bolt loading and stability of the gates. The affect of the pillar width on the bolt loading is also investigated in detail. The simulations are conducted for three representative overburden of the mine: case I: 110 m rock +250 m ice, case II: 300 m rock + 100 m ice and case III: 400 m rock. For all of those overburdens the bolt load for the conditions with pillar width of 30, 40 and 50 m are obtained. The models have same mechanical properties, boundary conditions, mesh size and loading process as described in the previous chapter.

In this chapter, first the roof cave-in progress via longwall mining is presented for those representative overburdens of the mine and later a critical distance ahead of the stope face, at which gate roof experiences stress increments, are obtained. Eventually, loading of the bolts installed at that critical distance is obtained for different pillar width.

5.2 Roof cave-in at the representative overburdens of the mine

Figure 5.1 illustrates the height of the cave-in and fracture zones with respect to different overburdens which obtained by numerical simulations. The geometry and boundary condition of the numerical models are similar to Figure 4.2 and the algorithm presented at Figure 4.1 was implemented to simulate longwall mining. Mining was started first in panel 1 and later on was continued in panel 2 until that the stope face is in a distance of 20 m to the 2D modelled cross section. The final height of the cave-in zone is a constant regardless of the overburden. It is mainly related to the strength of the roof strata and the locations of the weakness planes in the hanging wall. The major cave-in distance (l_p), however, is affected by overburden. It becomes shorter when the overburden increases. This change is because of higher tensile stresses induced in the roof under a large overburden. The height of the fracture zone increases slightly with an increase in the overburden.

5.3 Stress changes in the mining region

The stress changes in the rock and the cave-in materials obtained from the 3D model are shown on a horizontal plane located 2 m above the stope roof. It is assumed in the model that panel 1 has been completely mined out and panel 2 is half mined out. In this section, results of one of those representative overburdens are presented. The width of the chain pillar is 30 m, and the overburden of the model consists of 110 m of rock plus 250 m of ice. The distribution of the vertical stress on the horizontal plane is shown in Figure 5.2a. The vertical stress on the plane is quite low in areas close to the chain pillars in the mined-out regions. The vertical stress returns to its original state in the central areas of the mined-out regions. Stress concentration occurs also in the un-mined party of rock in panels in front of the longwall front and along gate B. The vertical stress is elevated in the position of the chain pillar, particularly in the completely mined-out region. It is worth pointing out that the vertical stress in the chain pillars is highly elevated for about 50 m ahead of the longwall front, where gate B is still used as a tailgate.

Figure 5.2b shows the horizontal stress parallel to the longwall front. It is obvious that low horizontal stresses occur in the mine-out regions because the cave-in materials are loaded mainly vertically. The horizontal stress increases ahead of the panel face along gate B for 30 m.

By considering Figure 5.2a and b it could be concluded that the most dangerous range ahead of the stope face, which need special consideration regarding the roof stability is a stretch of 50 m. Therefore, it is required for special treatment about roof stability and supporting measures in that stretch.

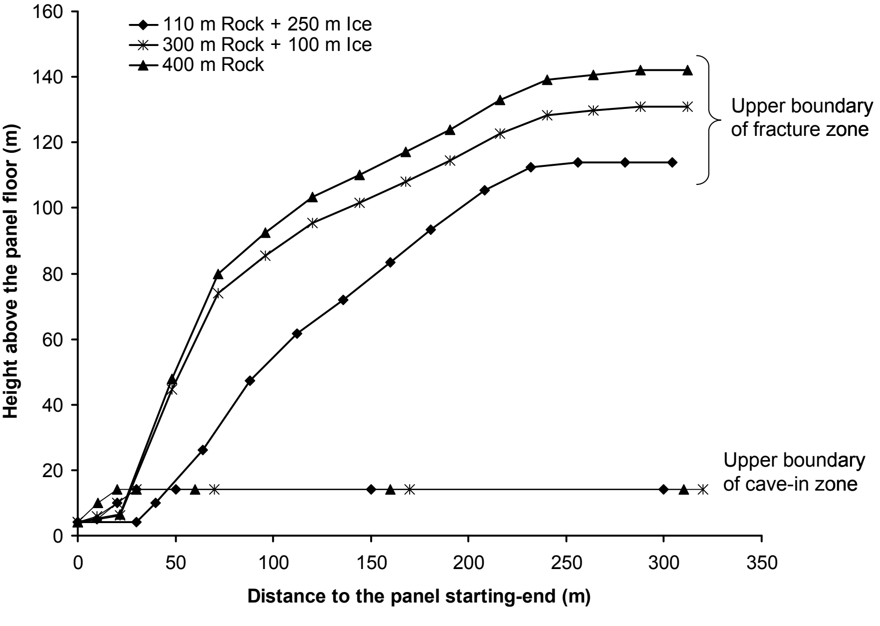

Figure 5.1 Height of the cave-in and fracture zones under different overburdens.

5.4 Influence of the chain pillar on the bolt loads

The influence of the pillar width on the load of rock bolts was studied numerically. Three pillar widths, 30, 40 and 50 m, were used for the simulations. Figure 5.3 shows the modelling results of the load distribution in the bolt located at the middle of the gate (B) when the panel 1 have been mined out and the stope face is 20 m inby modelled cross-section in panel 2. The bolt load changes abruptly at a depth of 1.5 m because of the existence of a weak coal seam. The maximum bolt load increases with a decrease in the width of the chain pillar. The bolt load was further studied by varying the thickness of the overburden (Figure 5.4). Under an overburden thicker than 400 m (300 m rock + 100 m ice), the bolts are subject to failure when the chain pillar is less than 40 m wide. It reveals that the stability of the gates is associated with the pillars width and at the study site. The chain pillars must have width more than 40 m in order to have stable gates.

Shear displacement occurred along the coal seam located at a depth of 1.5 m in the roof of the gate B. The relative shear displacement between the upper and lower limits of the seam is presented in Figure 5.5 with respect to three different pillar widths. The shear displacement will load rock bolts laterally and induce bending moments in the bolts. The shear displacement increases with a decrease in the pillar width. Therefore, rock bolts are more highly shear loaded in the case of a thin chain pillar than a wide pillar.

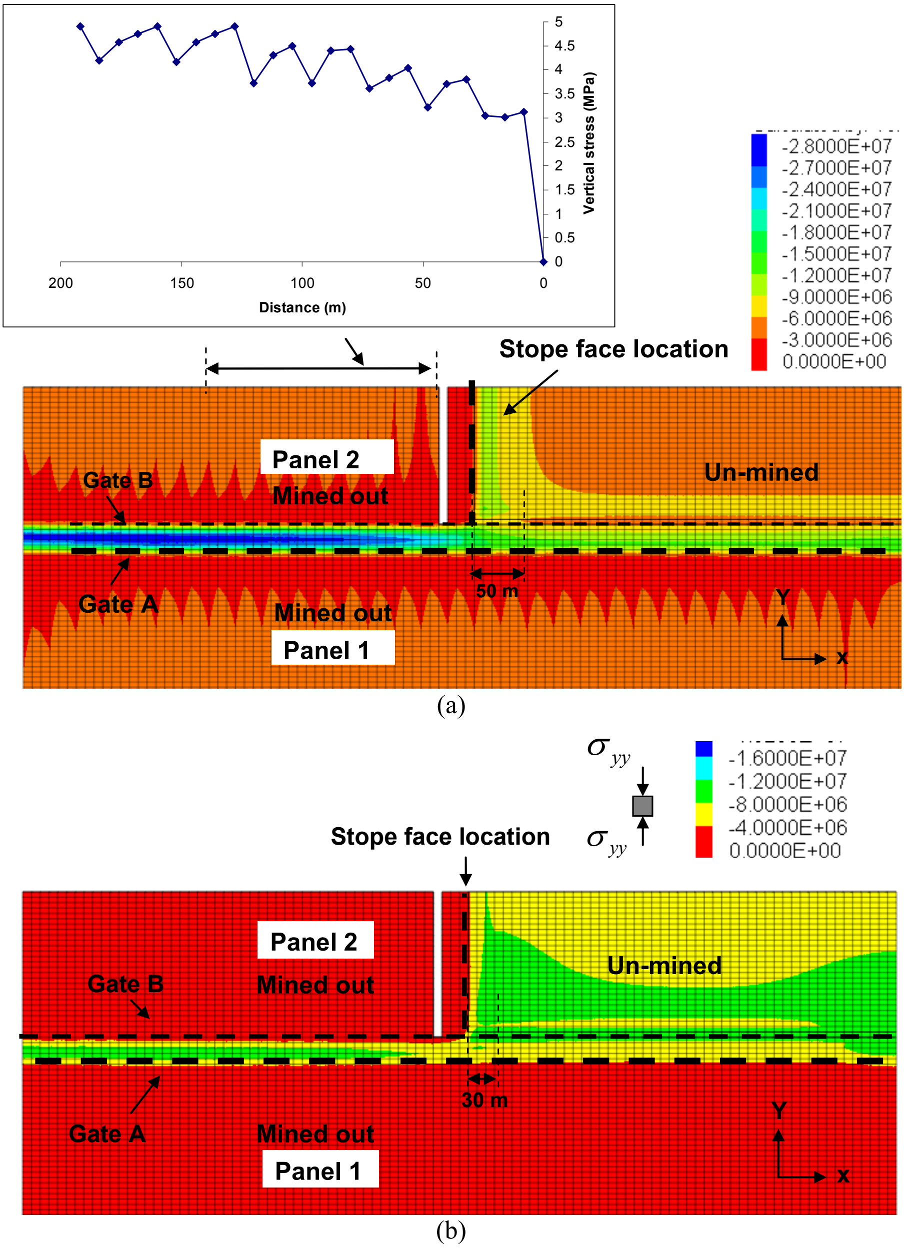

Figure 5.2 Vertical and horizontal stresses on a horizontal plane located 2 m above the stope roof in the three-dimensional model. (a) Vertical stress. (b) Horizontal stress. σ_{yy} is parallel to the longwall face.

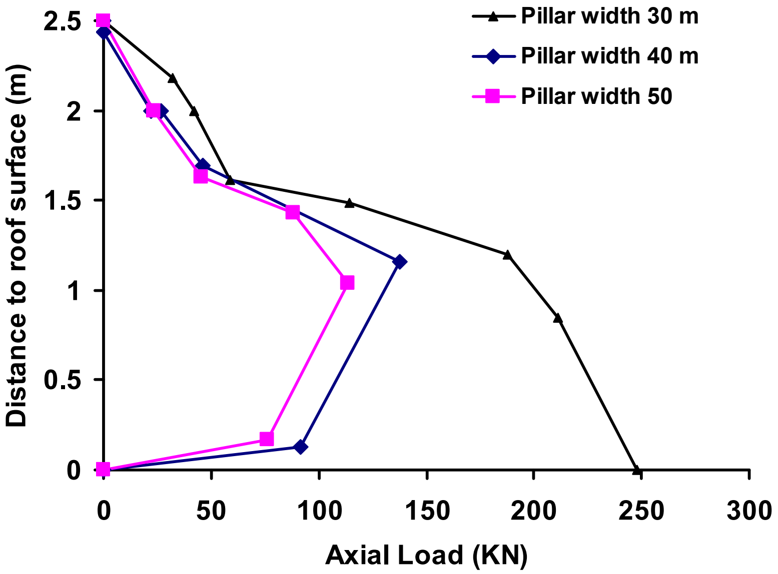

Figure 5.3 Numerical results of the axial load in bolt 5 under an overburden of 110 m of rock and 250 m of ice.

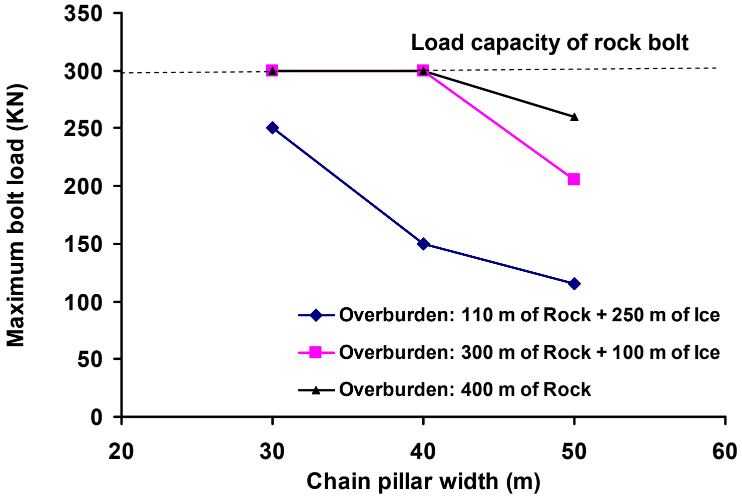

Figure 5.4 Influence of the width of the chain pillar. Maximum axial load of the rock bolts in gate B versus the width of the chain pillar for different overburden conditions.

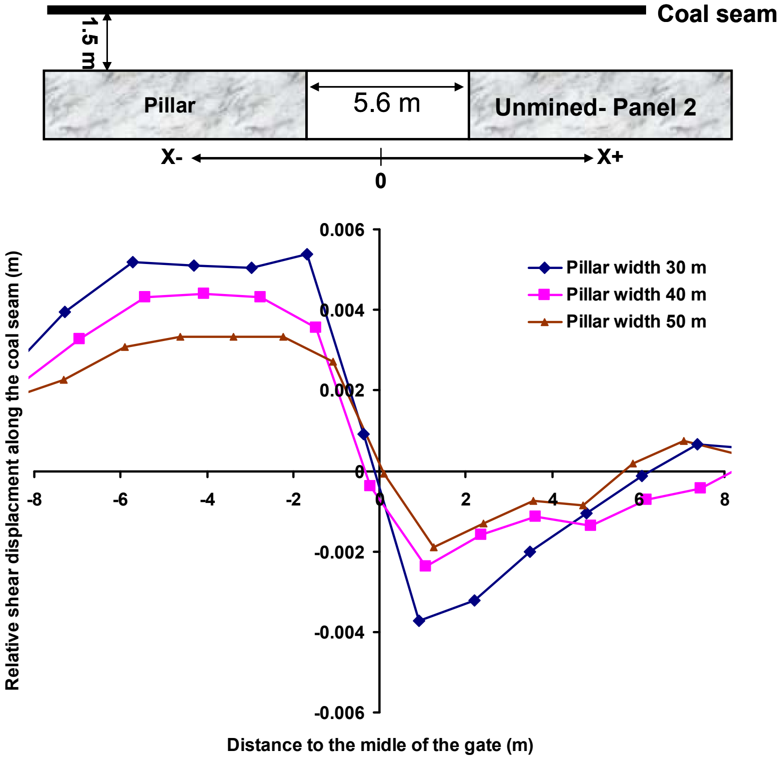

Figure 5.5 Relative shear displacement along the coal seam at a depth of 1.5 m in the roof of gate B after completion of mining in panel 1.

6 Stress changes induced by longwall mining

6.1 Introduction

In longwall mining, stope voids are filled by caved-in rock materials. Cave-in of the roof strata results in stress changes in the rock mass surrounding the longwall panels. The stress redistribution is mainly associated with the in-situ stress state, the layout of the panels, and the mining sequence. The vertical stress in panel walls would increase with an enlargement of the mined-out region. The horizontal stresses in the roof and floor are also changed by the advance of the longwall face as well as the enlargement of the mined-out voids.

As discussed before in the chapter 2, there is not a worldwide accepted method to obtain stress changes induced by longwall mining at the surrounding rocks. The developed numerical approach would be a strong tool for that purpose. Therefore, the algorithm presented in Figure 4.1 is implemented in the numerical simulations to study the stress state at the study site.

Stress changes ahead of stope face are a major concern at stability analysis of the stopes. Therefore, in this chapter at first the stress changes ahead of the stope face were investigated through numerical simulations. Then, two types of modelling were conducted: a local model for studying the stress changes at the barrier pillars and a mine-scale model which consists of all mining region and the border area. The local model includes only two panels to study how the stresses in the barrier pillars change during mining in the two adjacent panels. The aim of the global model is to study the disturbance at the border area caused by longwall mining. The characteristics of the rock masses, discontinuities, rock supports, cave-in and fractured materials are same as the previous models (Table 3.2, 4.1, 2 and 3).

6.2 Stress changes ahead of the stope face

In order to show how stress state changes ahead of the stope face, the simulation results from section 5.3 for the model with overburden of 110 m rock +250 m ice with pillar width of 40 m are used here. The vertical and horizontal stresses along the centre line of the panel at the coal seam level are shown in Figure 6.1. In the goaf area, they increase with the distance from the stope face and reach their maximum at a distance of about 200 m. In the un-mined part of the panel (in front of the stope face) the stresses have their peak values at a distance of 10 m in front of the stope face. After that they decrease gradually to their original values in the undisturbed state. The maximum vertical stress ahead of the stope face is about 3.2 time of the original vertical stress. It is depended on the mechanical properties of the cave-in and fractured materials, periodic cave-in distance and the maximum height of the disturbed zone above the goaf. The maximum abutment horizontal stresses with orientation of parallel and perpendicular to the panel alignment are 1.2 and 1.3, respectively, times of the original horizontal stresses. The numerical results show that the vertical stress concentration rate is the highest value and after that the horizontal stress with orientation of perpendicular to the panel alignment is the second highest stress concentration rate ahead of stope face.

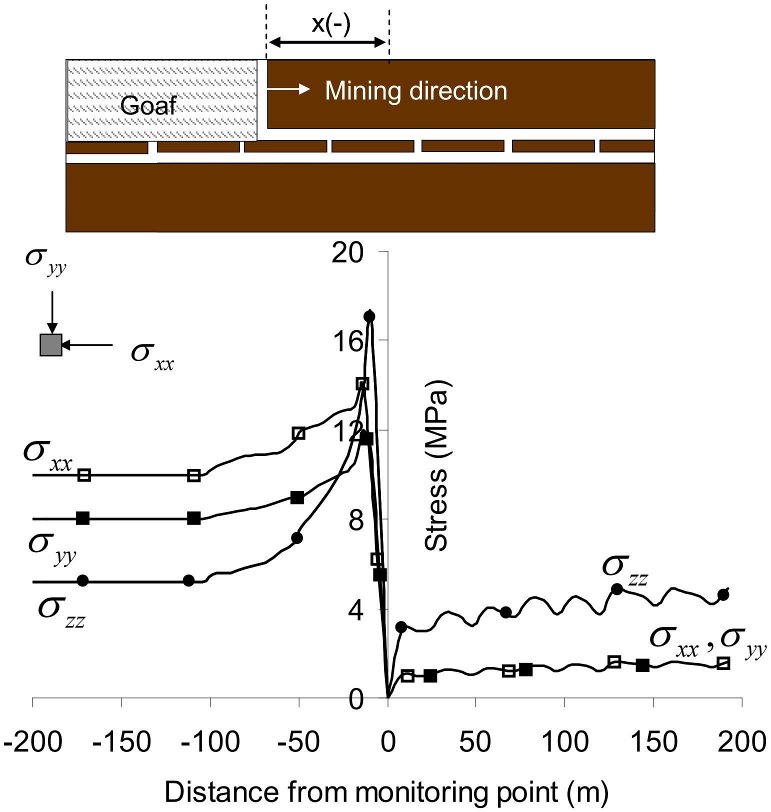

Figure 6.1 Distribution of the vertical and horizontal stresses in the middle of a panel along a horizontal line lying in the middle of the coal seam.

6.3 Local modelling

It is intended that the coal in the border area of Svea Nord mine will be mined out in the future. The barrier pillars beside the main tunnels play a significant role in protecting the border area from disturbance by longwall mining. A local 3D numerical model was established to study the stress changes in the pillars induced by longwall mining activities. The local model includes only two panels in order to simulate the influence of the mining process on the pillars in detail.

The local model is composed of two panels, C4 and C6 (Figure 6.2). Taking into account the symmetry of the displacement and stresses in the cross section of a panel, the model is bordered along the centre lines of the two panels in the horizontal plane. The size of the model is 1500 × 300 × 400 m (length × width × height; Figure6.3). The overburden is assumed to be composed of 300 m of rock and 100 m of ice. The rock part of the overburden is included in the model, while the ice part is replaced by a constant vertical stress on the upper boundary of the model (Figure 6.3). The roof strata are included in the model as illustrated in Figure 3.2. The rock mass is assumed to be an isotropic material obeying a strain-softening law. The mechanical properties of the rock and cave-in materials are given in Tables 3.2 and 4.2. Bedding planes and sandwiched layers of coal and bentonite in the roof strata of the mine are included in the model as discontinuities. These discontinuities obey the Mohr-Coulomb law. The mechanical parameters of the discontinuities are given in Table 4.1. Since the original in-situ horizontal stresses (σ_H and σ_h) are approximately parallel with and perpendicular to the longwall panels (a deviation of about 15 to 20 degree), the in-situ stresses are included in the model same as the original field measurements. History and monitoring points are placed at the mid-height of the panel and along the centre line of the barrier pillar (Figure 6.3a). The model has a same mesh size distribution and loading process as the models described in the chapter 4.

Panel C4 is mined out first, followed by C6. It should be noticed that a local coordinate system is used in the local model with the horizontal y-axis in the cross section of the panels, the horizontal x-axis along the panel length, and the z-axis in the vertical direction (Figure 6.2). Figure 6.4 shows the stress changes along the centre line of the pillar at different stages of mining. Mining in panel C4 causes negligible stress changes in the barrier pillar. Noticeable stress changes occur only when the distance from the longwall face to the pillar edge is less than 150 m. By taking the vertical stress as an example, we demonstrate how the vertical stress changes when the mining face approaches the pillar. The vertical stress σ_{zz} in the centre line of the barrier pillar starts to increase noticeably when the longwall face advances to a position about 150 m from the pillar edge (Figure 6.4a). The stress gradually increases with shortening of the distance until the face is about 20 m from the pillar. After that, rock failure starts to occur in the wall of the pillar, resulting in a reduction in the vertical stress because of rock failure. The failure zone starts at the pillar wall and extends to a depth of about 12 m in the wall when the longwall face reaches the position of the pillar edge. The vertical stress reaches its maximum, about 20 MPa, at the end of the failure zone. The vertical stress drops to 14 MPa after cave-in occurs in panel C6. The horizontal stresses change similarly to the vertical stress until the longwall face reaches the pillar edge. Differently from the vertical stress, the horizontal stresses increase slightly after cave-in occurs in the mine-out area (Figs. 6.4b and c).

Figure 6.5 shows the failure zones in pillar walls, marked by green and red colours, after completion of the mining in panel C6. The failure zones are in the outer portion of the pillar. The maximum depth of the failure zone is about 12 m in the side wall of the barrier pillar facing the mined-out panel. The huge inner portion of the pillar is still intact. Thus, the barrier pillar can provide the border area with good protection from the disturbance of longwall mining.

For showing the consistency of the numerical results with the reality at the mine, a photo of a pillar located in between main tunnels of the mine in front of the barrier pillar of panel C6 is presented in Figure 6.6. The corresponding location of the pillar is shown in Figure 6.5. It is seen that the pillar is stable while it slightly buckled and deformed toward the opening as anticipated by the numerical model (Figure 6.5).

Due to importance of the barrier pillars in protecting main tunnels of the mine from the disturbances of the longwall mining, they have vital role in the mine stability. Therefore, we have done a detail study regarding the stress distribution within the pillars for those three representative overburdens of the mine.

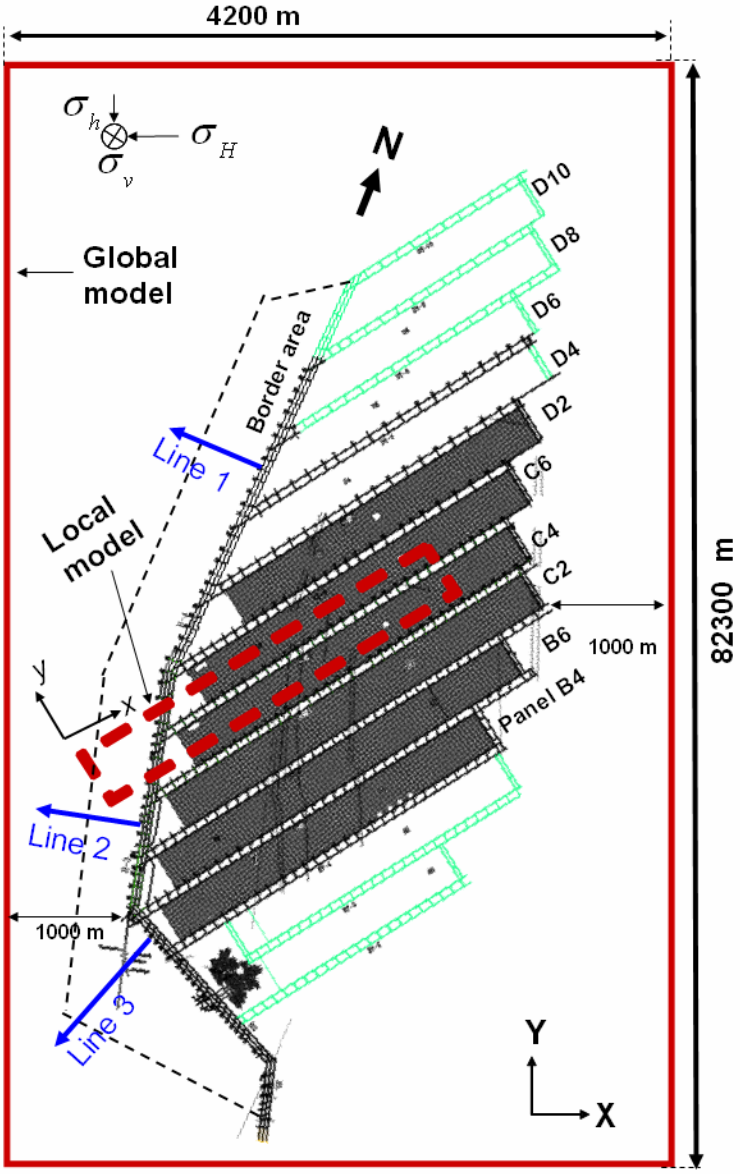

Figure 6.2 Mine map and location of the local and global models.

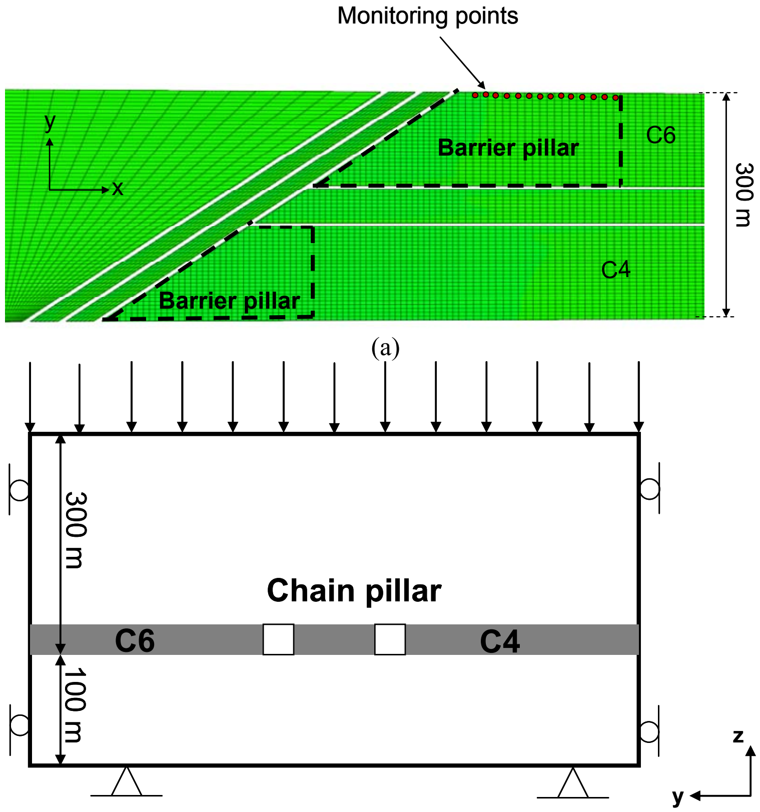

(a)

(b)

Figure 6.3 The 3D local model: (a) horizontal view; (b) cross section of the model and the boundary conditions

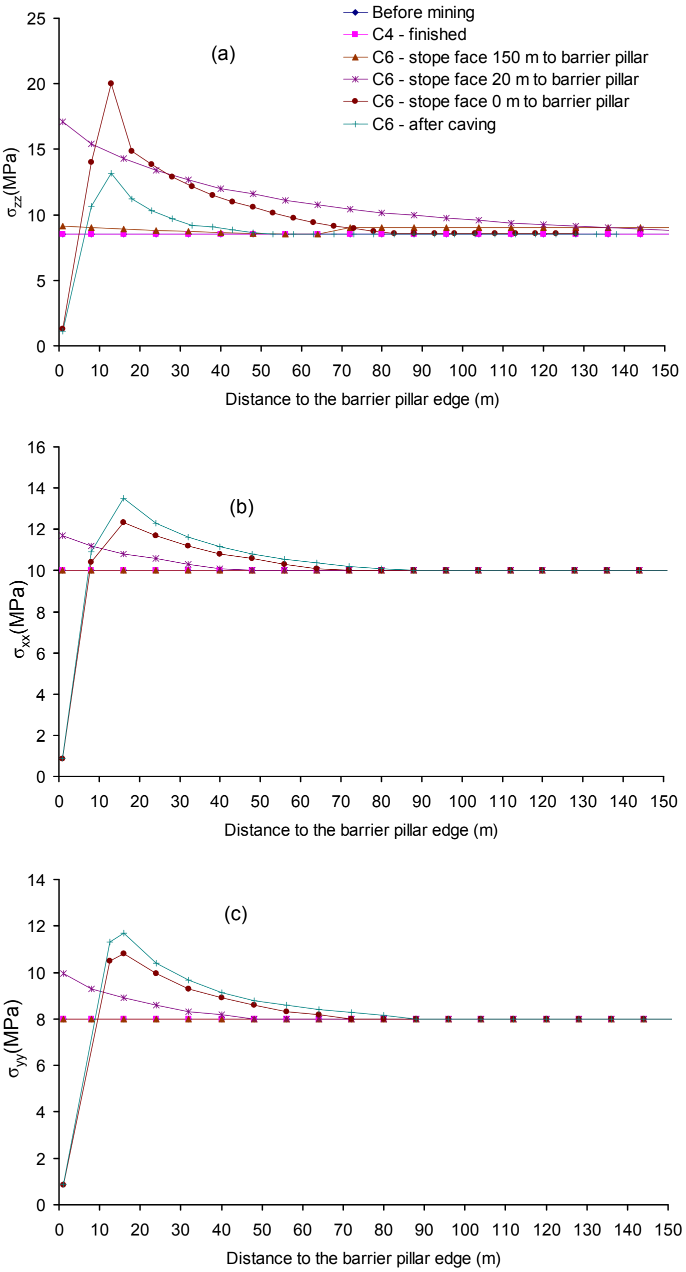

Figure 6.4 Stress changes along the centre line of the barrier pillar in different stages of mining: a) the vertical stress σ_{zz}, b) the horizontal stress σ_{xx} parallel to the panel, and c) the horizontal stress σ_{yy} perpendicular to the panel

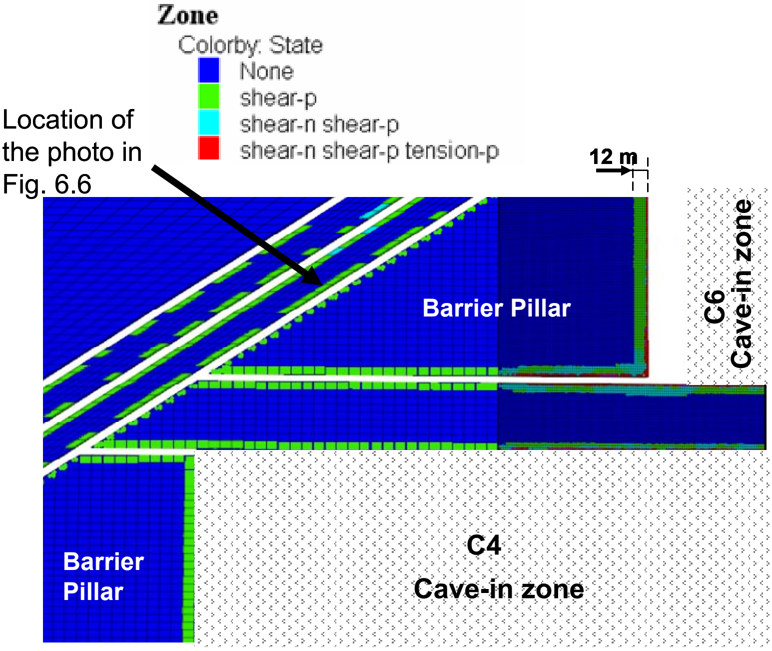

Figure 6.5 Failure zones in the barrier pillar

Figure 6.6 The pillar between main tunnels of the mine located in front of the panel C6. The location of the pillar is shown in Figure 6.5.

6.3.1 Vertical stress distribution in the pillar

The load in the barrier pillars is associated with the size of the fracture zone above the panel and in turn with the overburden. Three different overburdens were examined in the model. They are Case I: 110 m rock + 250 m ice; Case II: 300 m rock + 100 m ice; and Case III: 400 m rock. The vertical stress along the centre line of the pillar is shown in Figure 6.7 for the three cases of overburdens. The vertical stress is zero at the side wall surface of the pillar and increases to its maximum value at a certain depth in the wall. The rock from the wall surface to the position of the maximum stress is in the post-failure stage, resulting in a reduced stress in that region. In the region beyond the position of the maximum stress, the rock/coal has not failed and the stress decreases exponentially with distance from the wall. It can be seen in the figure that the position of the maximum stress moves toward the inside of the pillar with an increase in the rock cover, which indicates that the failure zone becomes larger with a larger overburden.

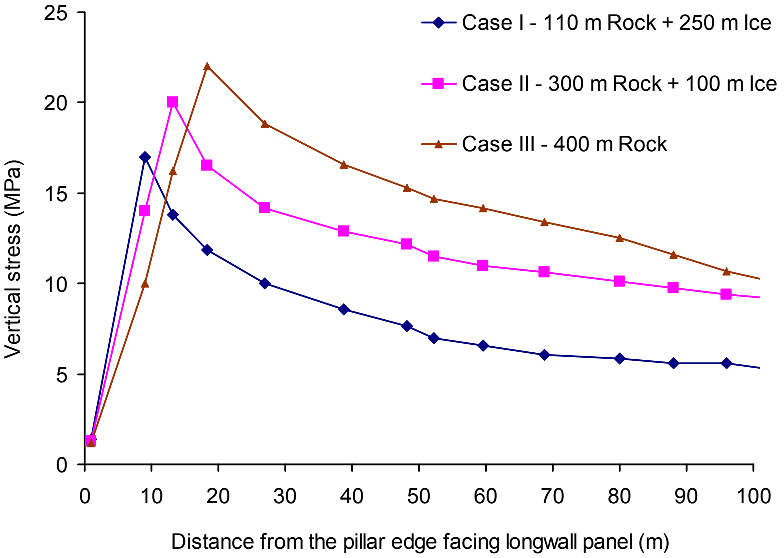

Figure 6.7 Vertical stress in the barrier pillar for different overburdens.

6.3.2 Stress changes in the pillars

With the conventional tributary area design method, the vertical pillar load is equal to the weight of the rock prism overlying above the pillar (Mark et al. 1999). Mining induced cave-in results in stress relaxation in the fracture zone above the mined-out panels. A pressure arch is formed in the dome-shaped boundary of the fracture zone unless the fracture zone has reached the ground surface. The caved-in materials and the fracture zone are at least partially de-stressed. In this case, however, numerical modelling would be able to provide more reasonable results on stress mitigation than the tributary area method. For the sake of comparison, the maximum vertical pillar stresses in the three cases of overburdens are presented in Figure 6.8. The x-axis of the diagram is the relative height of the fracture zone compared to the overburden, h_f/H, where h_f is the height of the fracture zone and H the thickness of the overburden. In the case of the overburden composed of 110 m rock + 250 m ice (case 1), the fracture zone reaches the ground surface. The maximum vertical stress in the pillar is about 3.2 times the in-situ vertical stress. For cases 2 and 3, which have more rock cover in the overburden, the vertical pillar stress is about 2.3 times the in-situ stress. In these two cases the absolute pillar stresses are a little higher than those in case 1, but the ratio to the in-situ stress is smaller.

The stresses in the barrier pillars fluctuate up and down following periodic cave-in events behind the longwall face during mining. The stress change is related to the critical advance length l_s. Figure 6.9 shows changes of the maximum vertical and horizontal stresses in the pillars for the three cases of the overburdens. The vertical stress change is a reduction of 5–6.5 MPa depending on the critical advance length l_s and equivalently on the overburden. The horizontal stress change is an increase of a small amount almost irrespective of the advance length l_s and the overburden.

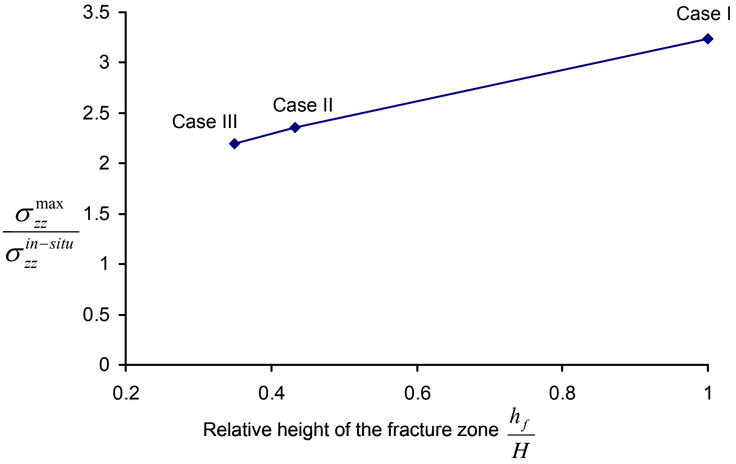

Figure 6.8 The maximum vertical stress in the barrier pillar when the entire panel adjacent to the pillar mined out

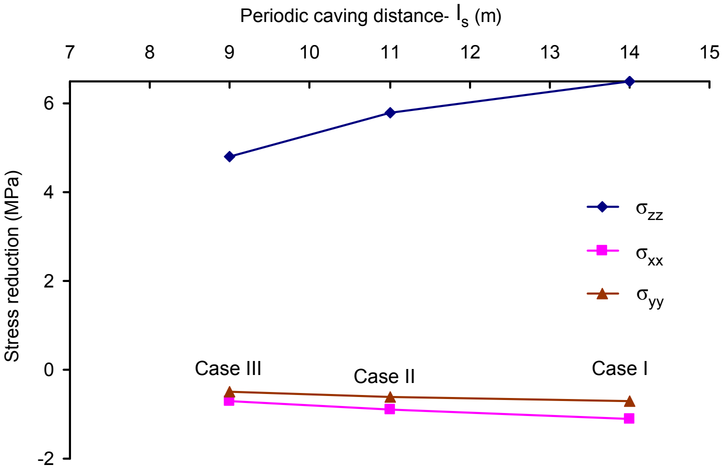

Figure 6.9 Stress changes in the barrier pillar after cave-in in the mined-out panel. Decreases and increases in the compressive stress are shown with positive and negative magnitudes, respectively.

6.4 Global modelling

The stress changes in the border area are affected by all the longwall panels. A mine-scale 3D global model was constructed to simulate the stress state in the border area after completion of mining in all the longwall panels. The global model includes all the panels within it. Small volumes of excavations in the panels have little impact on the border area. Therefore short excavation advances were omitted in the large-scale simulations. Instead the entire panel is mined out in every mining stage in order to save time. A global co-ordinate system is used in the global model with the horizontal X-axis lying approximately in the eastward direction, the horizontal Y-axis approximately in the northward direction, and the Z-axis still in the vertical direction (Figures 6.2 and 6.10).

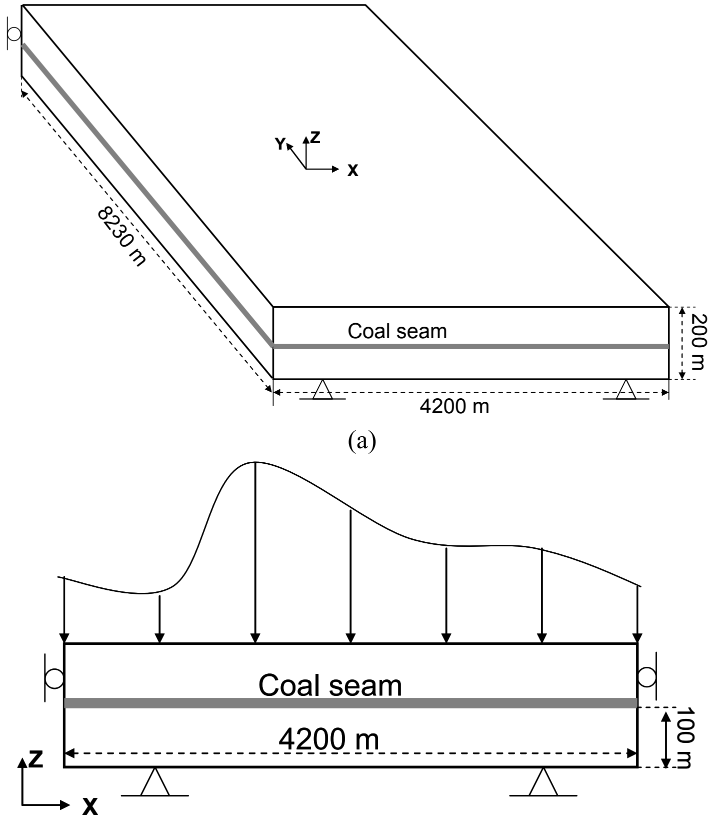

(a)

(b)

Figure 6.10 The global model: (a) 3D view and (b) cross section in the X-Y plane

The global model is 8230 m long, 4200 m wide, and 200 m thick (see Figure 6.2 and also Figure 6.10). The vertical stress applied on the upper boundary of the model is equal to ρgZ, where ρ is the density of the rock mass, g is the gravitational acceleration, and Z is the thickness of the overburden. The stress on the upper boundary is unevenly distributed because of the variation in the elevation of the ground surface. It is assumed that the two in-situ horizontal stresses have same directions and magnitudes with the field measurements. The geological column of the study site is included in the model as illustrated in Figure 3.2. The bedding planes and the sandwiched coal and bentonite interlayers are included in the model as discontinuities. The properties of the rock masses and discontinuities are identical to those used in the local model (see Tables 3.2 and 4.1 and 2). The mesh size of the model at the coal seam level varies from 4×2×2 to 10×2×2 m in X,Y and Z directions, respectively. In the roof and floor strata the mesh size increases by distance from the coal seam. Generally, the mesh size in the roof and floor of the model is about 10×10×4 m in X, Y and Z directions, respectively. Three lines in the border area (lines 1, 2, and 3), are chosen to monitor the stress changes in the border area. The three monitoring lines are marked in Figure 6.2.

The model is first run to equilibrium before excavation. Mining in a panel is simulated by changing the mechanical properties and constitutive law of the rock materials in the cave-in and fracture zones whose borders are outlined in the local model. This procedure starts from panel B4 and continues until panel D10. A similar simulation approach was employed by Tajdus (2009) and Whittles et al. (2006).

The principal stresses along the three monitoring lines are presented in Figure 6.11. The major principal stress σ_1 is in the vertical direction in the near-field of the main tunnel, but it becomes horizontal at a long distance from the tunnel. The stresses are zero on the tunnel wall and increase to their maximum values at a depth of about 10 m. That implies that the first 10 m of the wall fails. The stresses drop to the in-situ stress levels when the distance is more than 25 m from the wall, which indicates that the stress state in the area at least 25 m from the main tunnels is not influenced by the longwall mining.

Figure 6.12 shows the horizontal stresses (σ_{XX} and σ_{YY}) in a horizontal plane 2 m above the panel floor in a part of the barrier pillar region. The local model has shown previously that stress concentrations occur in the barrier pillars. The global model shows that the stresses in the border area on the other side of the main tunnels are not noticeably changed by the longwall mining.

Three panels, B4, B6, and C2, were mined out in sequence in the model in order to examine how mining in panels B6 and C2 influences the stress state in the barrier pillar of B4. The horizontal stress changes along the centreline of the barrier pillar of panel B4 during mining in panels B4, B6 and C2 is presented in Figure 6.13. The results show that mining in panels B6 and C2 does not affect the stresses in the pillar.

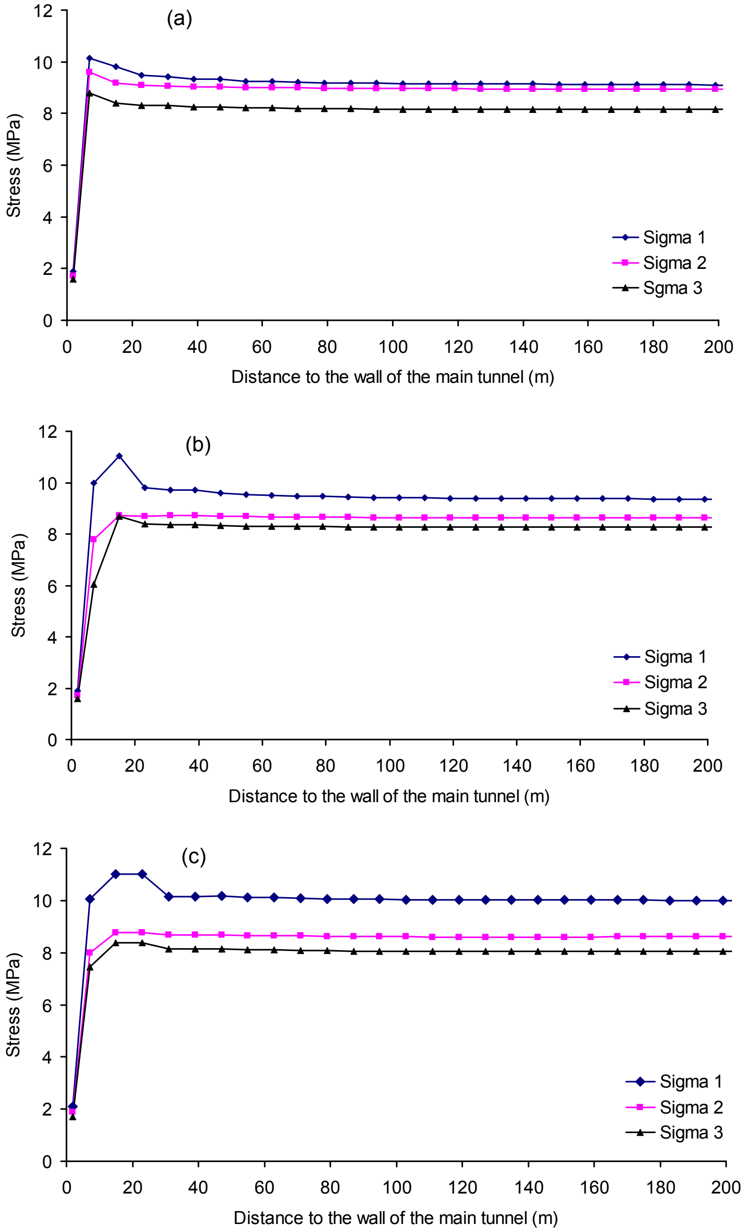

Figure 6.11 Principal stresses in the border area after mining of panels C4 to D10, along: (a) line 1, (b) line 2 and (c) line 3.

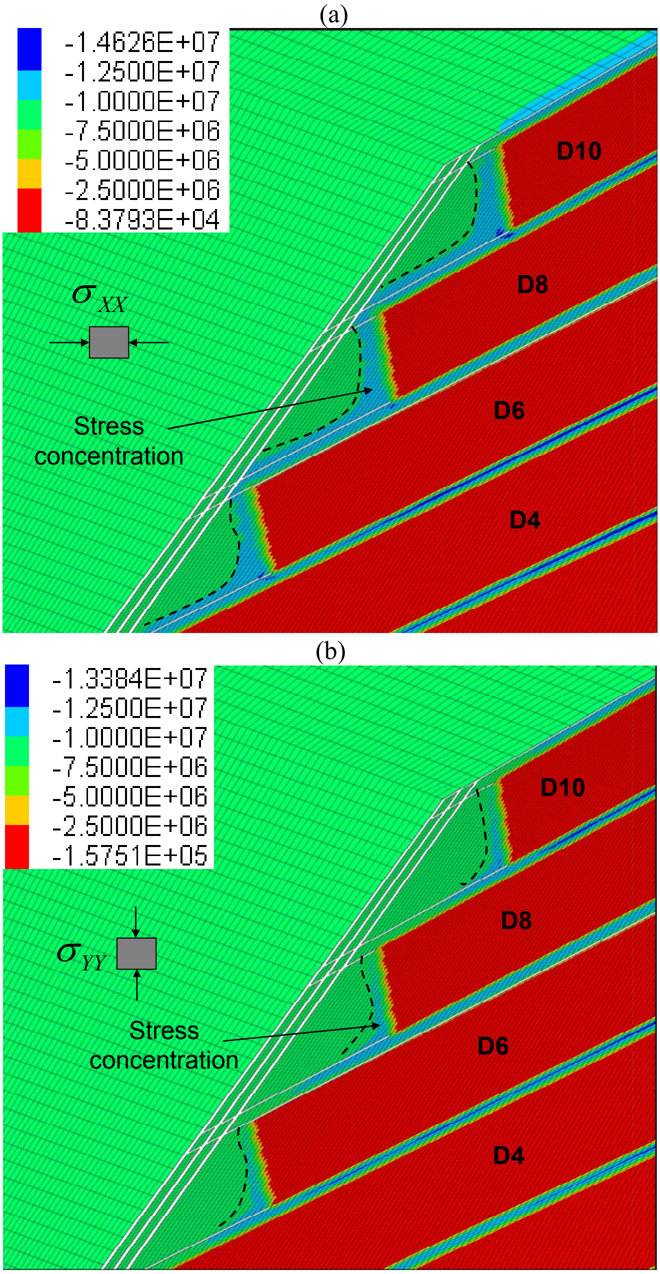

Figure 6.12 Horizontal stresses at the level of coal seam after completion of the longwall panel mining: (a) σ_{XX} and (b) σ_{YY}

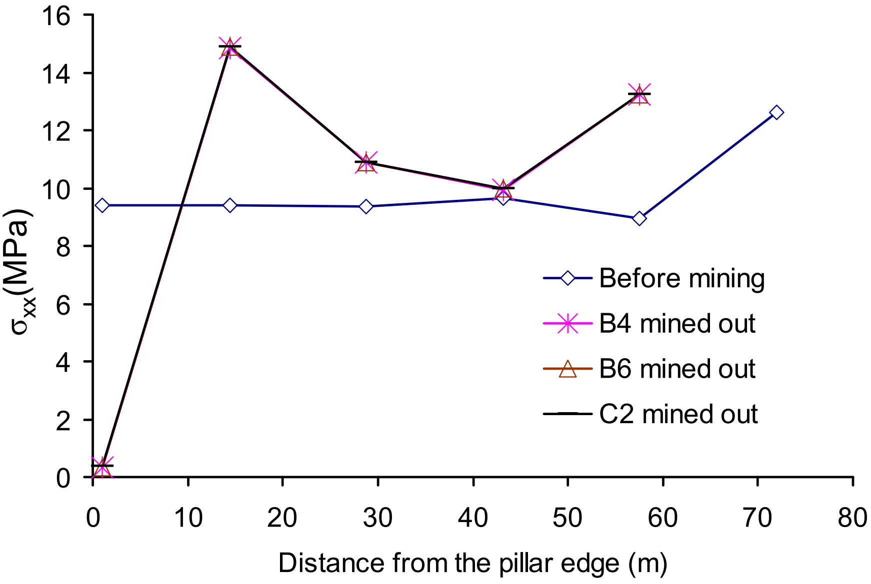

(a)

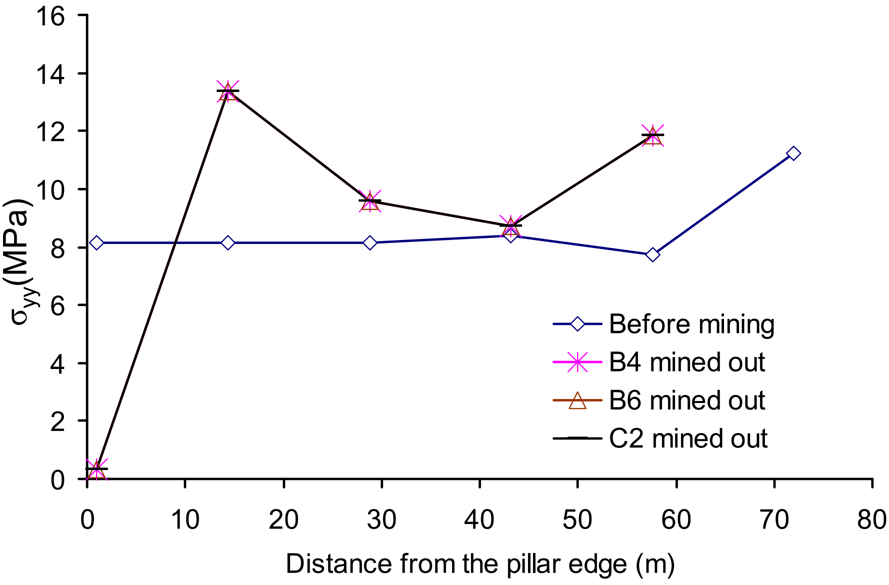

(b)

Figure 6.13 Changes of the horizontal stresses, (a) σ_{XX} and (b) σ_{YY}, along the centre line of the barrier pillar in front of panel B4 after mining panels B4, B6 and C2.

7 Roof strata cave-in mechanism in the longwall panels

7.1 Introduction

In the previous chapters, it has been addressed the importance of understanding the cave-in mechanism in the longwall geomechanics. Gate stability, stress disturbance and stope stability are, indeed, associated with the cave-in performance and the behaviour of the cave-in materials under the weight of the overburden strata. A delayed roof cave-in could lead to severe consequences, for instance stope jamming, stope face bursting, rock and air bursts. Therefore, a thorough understanding of the roof cave-in mechanism is helpful for ground control design in the planning stage of longwall mining, for instance in estimating the load capacity of longwall shields and the length of the longwall stopes.

In this chapter, it would be tried out to study the roof cave-in mechanism at the study site and investigate how different geological environment would influence the cave-in performance (cavability) of the roof strata as well as loading on the longwall shields. The background and literature review about the roof cave-in mechanism have been presented in Chapter 2. It has been showed that none of the existing methods is enough capable in determining the cavability of the roof strata and the required support capacity of the shields.

Roof cave-in is a progressive process which starts in a critical distance behind the stope face and develops upward as the face advances. Cave-in ceases when the cave-in materials fully fill the stope void. The roof strata next to the stope face load the shields via either downward deformation or the dead weight of the cave-in materials. Strong and massive roof strata do not cave in immediately, leaving an overhang, behind the longwall shields. Periodic cave-in events occur after the first cave-in so that a periodic weighting is placed on the longwall shields. These phenomena may also be observed when the stope void is not yet fully filled. Moreover, cave-in depends not only on the geomechanical characteristics of the roof strata, but is also associated with the height of the stope and the location of the bedding planes in the roof. As a result, numerical modelling is an appropriate method to simulate the dynamic process of cave-in and to assess the load on the longwall shields.

Previously an algorithm for numerical modelling of longwall mining in FLAC$^{(3D)}$, Figure 4.1, was proposed. For applying the algorithm to a given mine, it is necessary to determine the critical cave-in strain for the mine. Because of this a comprehensive study of the roof cave-in mechanism is required. Discontinuous models more realistically describe rock masses than continuous models and they can be used for detailed small scale simulations with considering influences of the large number of rock mass characteristics.

In this chapter, a discontinuous numerical code, UDEC, was used to study the roof strata cave-in process in the study site. A back-calculation method, based on a statistical method of design of experiment (DOE), was implemented to obtain the required parameters. The calculated loads on longwall shields were then compared with field measurement data. Beam theory was used to explain the cave-in mechanism.

The loads on the longwall shields were monitored with respect to stope face advances when the panel C6 of the study site (Figure 3.1) was half mined out. Field measurements revealed neither significant overhanging nor any periodic weighting on the longwall shields during mining of this panel. The shield load data were used to calibrate the numerical models.

7.2 Numerical modelling

UDEC, a code based on the discrete element method (DEM), was used to model roof strata cave-in at the study site. The code is capable of simulating large displacement, separation and rotation of rock blocks. A cross-section along the centre line of panel C6 was selected for modelling in order to fulfil the plane strain condition in a 2D model. The model consisted of discrete blocks representing the discontinuous medium of the rock masses surrounding the panel. In the model, the rock blocks were deformable and obeyed a linear elastic stress-strain relationship. Discontinuities obeyed the Mohr-Coulomb constitutive low. The mechanical properties of the rock mass and discontinuities are presented in Table 7.1. The dimensions and boundary conditions of the model are illustrated in Figure 7.1. The average spacing of bedding planes was assumed about 1 m at the roof strata based on the core logged from the boreholes at the study site. Most of the crosscut joints in the roof strata are created by mining so that the spacing of the crosscut joints cannot be predetermined before mining starts. It was determined in the model by back-calculations of the first cave-in distance.

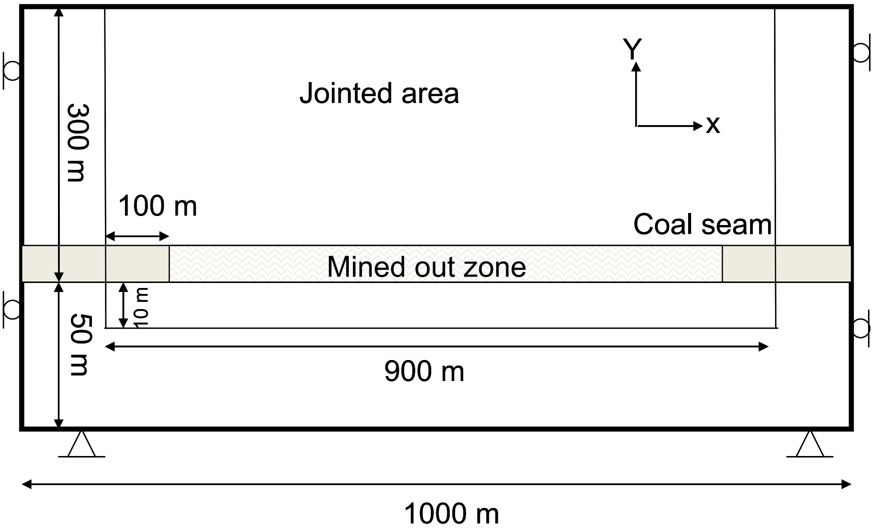

Figure 7.1 Geometry and boundary condition of the numerical model

Table 7-1: Mechanical properties of rock blocks and discontinuities in the UDEC model.

Rock blocks	Young's modulus (GPa)	Poisson ratio	Density (Kg/m3)
	12	0.25	2500
Discontinuities	Cohesion (MPa)	Friction (Degree)	Tensile strength (MPa)
	0	30	0

The normal and shear stiffness of joints, K_n and K_s are also important in the simulation of both the cave-in process and the load on longwall shields. K_n and K_s are associated with the length of joints and the normal stress. K_n and K_s were determined by back-calculations at the moment of the first cave-in. In addition, the numerical results of the longwall shield load during subsequent cave-in events in panel C6 were compared with field measurement data for the sake of verification of both the numerical results and the applicability of the model in investigation of longwall shield loading.

The longwall shields were simulated as two stiff blocks connected by support elements between the roof and floor in the model. The support elements are one-dimensional and thus could only sustain load-deformation in the axial direction. The stiffness of the longwall shields in the mine is assumed 120 MN/m which was determined using the method by Singh & Singh (2009) and Barczak (1992). A longwall shield is about 2 m wide. In the model, the support elements had an out-of-plane spacing of 1 m and thus the stiffness of the support elements is 30 MN/m.

7.2.1 Back-calculations

Back-calculation is often used to indirectly determine rock mass properties. As mentioned above, the normal and shear stiffness of the rock joints, as well as the spacing of the crosscut joints in the roof strata were determined via back-calculations in this study. Field observations revealed that the first cave-in distance in the longwall panels was around 36 m; this distance was used to back-calculate the unknown parameters.

Generally, an iteration method is employed for back calculations. However, the iteration method is time consuming when more than one parameter is back calculated.

A statistical method, called the design of experiment (DOE) technique (NIST 2012), was used in this study for back calculations. DOE can be used to qualitatively evaluate the relationship between input variables (factors) and the output of experiments.

With the DOE method, it needs to define the experimental objective and select the input/output variables. In our case, the unknown parameters are the normal and shear stiffness of rock joints, K_n and K_s, and the spacing of the crosscut joints. The first cave-in distance (l_p) is the experimental response (i.e. output). Furthermore, the variation range of each parameter needs to be pre-defined before experiments start. Joint shear stiffness K_s is associated with joint dilation and friction angle, joint length and normal stress on the joint plane (Barton 1977). Bandis et al. (1983) produced a graph to assess K_n based on their test results and in-situ observations. The length of crosscut joints was assumed to be 1 m in the present study. An elastic numerical simulation revealed that the maximum horizontal stress in the roof of the open stope barely exceeds 12 MPa. K_s was, thus, assumed to be in the range of 0.005-2 GPa/m. Joint normal stiffness (K_n) can be calculated from the joint shear stiffness and the normal stress on the joints (Bandis 1983). During cave-in the normal stress on the crosscut joints is very small and therefore the ratio of K_n/K_s in the present study was assumed to be a value in the range of 10 - 100, that is, K_n was in the range of 0.5-20 GPa/m.

Price (1966) developed a theory suggesting that the spacing of crosscut joints in laminated sedimentary rocks is about the same as the thickness of the stratum, while Narr & Suppe (1991) argued that such spacing is around 1 to 3 times the stratum thickness. The mine in study is characterised by the presence of a number of mining-induced fractures/joints. The joint spacing used in this study was assumed to be 1 to 2 times the stratum thickness.

After definition of the variation ranges of the parameters, DOE experiments started using a number of data sets in the ranges given above. A linear, quadratic, or high order functions, denoted as the response surface method (RSM) (NIST 2012), was fitted to the experimental output. A RSM was then established to predict the nonlinear relationships between the input parameters and the outputs of the experiments. In the present study, the input parameters of the experiments are the normal and shear stiffness of rock joints, K_n and K_s, and spacing of the crosscut joints (S_j). The output is the first cave-in distances (l_p).

Formation of the data sets requires special techniques based on the number of input parameters and also the number of experiments. The data sets, in Table 7.2, were selected with the help of the central decomposition method (CDM) (NIST 2012), which is suitable for experiments comprised of three input parameters.

Table 7-2: Data sets proposed by CDM to obtain the RSM.

Group number	K_n (GPa/m)	K_s (GPa/m)	S_j (m)
1	0.5	0.005	1
2	0.5	0.005	2
3	0.5	2	1
4	0.5	2	2
5	20	0.005	1
6	20	0.005	2
7	20	2	2
8	0.005	1.0025	1.5
9	26.9	1	1.5
10	10	0.001	1.5
11	10	2.7	1.5
12	10	1	0.4
13	10	1	2.7
14	10	1	1.5
15	10	1	1.5
16	10	1	1.5
17	10	1	1.5
18	10	1	1.5
19	10	1	1.5
20	10	1	1.5
21	10	1	1.5
22	10	1	1.5
23	10	1	1.5

Note: K_n is the normal stiffness and K_s the shear stiffness of joints in the model. S_j denotes the spacing of the crosscut joints.

The simulation results based on the data sets were then used to derive a quadratic function describing the relationship between the input parameters and the output. The response surface has the form of:

$$l_p=-4.656+4.0499K_n+39.85K_s+11.32S_j+0.59K_nK_s-0.67K_nS_j-11.50K_sS_j-0.10K_n^2-7.29K_s^2-2.05S_j^2 \qquad (7.1)$$

where K_n and K_s are in GPa/m and S_j in m.

The back-calculations finally revealed that the most favourable parameters for the study site were $K_n = 18$ GPa/m, $K_s = 0.05$ GPa/m and $S_j = 1$ m. These data were used for the numerical modelling presented in the following section.

7.2.2 Summary of modelling results

The excavation sequence in the model was the same as the real one, that is, a 5 m-long advance for every excavation round. The stepwise excavation makes it possible to evaluate the process of cave-in and the load-deformation behaviour of the roof strata.

After excavation, the vertical stress is elevated compared with its original state in the abutments. The roof strata above the mined-out stope separate from each other at the bedding planes under the gravity and deflect and even fail in buckling. The vertical stress concentration in the abutments, pillars and roof strata above the gates, affects the stability of the stope face, gates and pillars.

The roof cave-in is associated with the separation of roof strata and the horizontal stress. The separation length decreases with the distance from the stope roof. The strata experience tensile fracturing, separation and rotation in the region between the roof surface and a critical depth where the bedding plane separation is negligible.

Figure 7.2 depicts the horizontal stress distribution in the panel roof just before the first cave-in, when the stope face has advanced 30 m since the start of mining.
Because the horizontal stress is higher than its vertical counterpart, it may be expected that the maximum horizontal stress concentration should occur within the roof strata. However, the periodic fluctuations in the horizontal stress imply that the separated roof strata behave like beams. Beam bending induces stress fluctuations in individual roof strata. Above the mined-out stope, the roof strata are separated from the host rock and the rock blocks in the strata rotate and form a voussoir beam. The beam theory tells that beam deflection will result in tensile stresses in the lower portion of the beam, while compressive stresses in the upper portion. The total horizontal stress in the beam is the superposition of the bending stress and the in-situ horizontal stress in the strata. It is always compressive in the upper portion of the beam, but it may be either compressive or tensile (or zero in the case of joint separation) in lower portion depending on the

magnitude of the in-situ stress. In extreme cases, the beam deflection is so large that the beam could collapse either due to crushing or buckling. However, the UDEC model is not able to simulate rock crushing.

The horizontal stress in the roof strata in regions close to the ends of the stope has a pattern different from that in the middle region above the stope (Figure 7.2). The roof strata behave like cantilever beams with the fixed ends sitting deeply in the host rock. The transition zones between the voussoir beams and the cantilever beams incline toward the centre of the voussoir beam region. The cantilever beams are formed owing to the downward deflection of the voussoir beams above the mined-out stope.

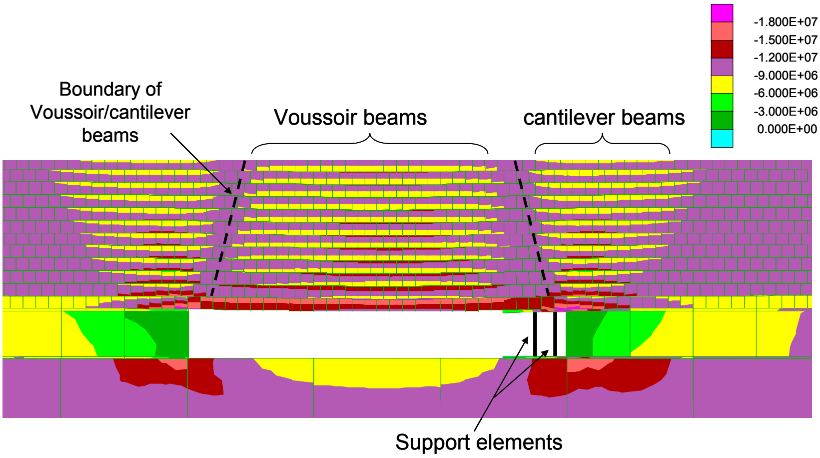

Figure 7.2 Horizontal stresses in the roof strata when the length of the open stope is 30 m.

After the first cave-in, the voussoir beams collapse and fill the stope void. The in-situ horizontal stresses in the host rock surrounding the stope void then become elevated. An additional consequence of the roof cave-in is that the horizontal stresses in the cantilever beam regions become decreased dramatically.

In this chapter, the deflection of a roof stratum is expressed as the ratio of its vertical deformation to its thickness. Based on the analytical methods by Diederichs & Kaiser (1999a), the middle deflection of a voussoir beam deviates from the linear behaviour upon reaching 10% of the beam thickness. The beam collapses at a deflection of 25-35% (Diederichs & Kaiser 1999a; Sofianos 1996). In these methods, it is assumed that the confining horizontal stresses in the beam are induced by the rotation of rock blocks. As a result, the maximum sustainable deflection of a beam increases with the horizontal stress.

In order to investigate the beam formation and the bending process, the maximum horizontal stress and the downward deformation at the middle span of a stratum beam was monitored in the model versus the stope face advance (Figure 7.3). Plotted in the figure are also the roof displacement in a continuous homogenous medium, which are the results from a boundary element modelling using Examine2D (Rocscience 2012). The numbers, 5, 9 and 12, means that the distance of the monitoring positions above the panel floor. The deflection increases and also the stresses in the roof strata are changed, with the stope face advance. Figure 7.3a shows that the stress change starts as soon as mining begins. Roof deflection causes higher stress in the laminated strata than in the homogenous rock masses. The stress increment depends upon the extent of strata bending. It increases with the advance of the stope face. The roof deflection is approximately 25% when the stope advances 30 m.

The maximum horizontal stress (σ_{xx}^{max}) at the middle span is plotted versus the beam deflection prior to the occurrence of the first cave-in in Figure 7.4. The stress σ_{xx}^{max} starts to dramatically increase when the stope face advances to the distance of 30 m and reaches its ultimate at 35 m. The beam strata are then failed in buckling. Buckling of the roof strata occurs at a deflection of 60–75%.

The voussoir beams can fail in the form of crushing (Figure 2.4) when the maximum horizontal stress in the beam at the middle span reaches the compressive strength of the rock material (Diederichs & Kaiser 1999a; Sofianos 1996). 60% of the uniaxial compressive strength (UCS) of the rock material was used as the crushing strength of the rock beams in this study. The UCS of the main roof strata in the study site is about 60 MPa; 60% of the UCS, i.e. 36 MPa was taken as the crushing strength of the voussoir beams. It is seen in Figure 7.4 that the maximum horizontal stress in the first 16 m roof strata drops after its ultimate value, marking buckling failure there. The stress continues to increase with deflection in the roof strata above 16 m, some portion of the rock there may fail in crushing when the stress is beyond the crushing strength of the rock.

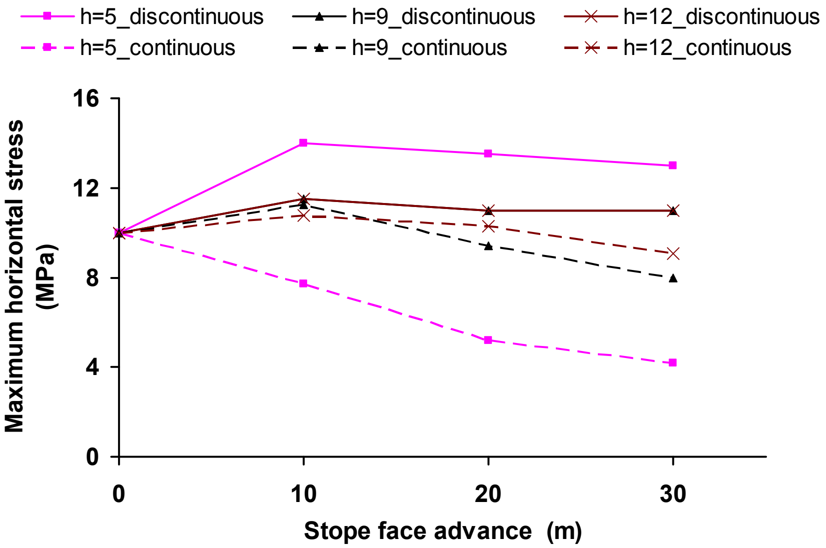

(a)

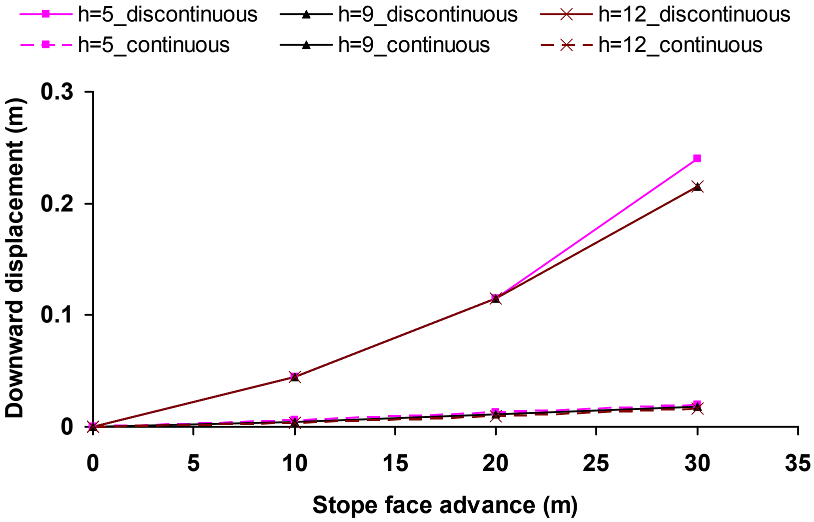

(b)

Figure 7.3 (a) Horizontal stress and (b) downward displacement of the stope roof versus stope face advance. h refers to the height of the roof strata/rock above the floor of the stope.

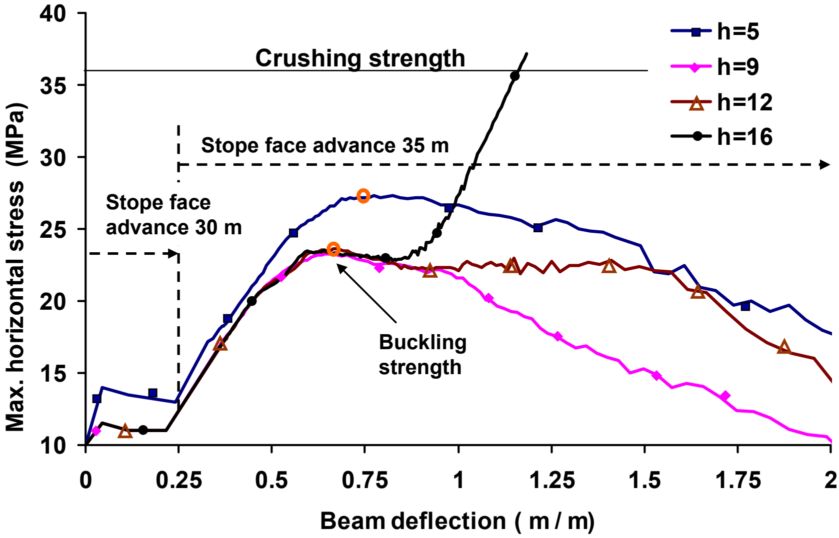

Figure 7.4 Maximum horizontal stress versus deflection of the roof strata. h refers to the height of the roof strata above the floor of the stope

The periodic cave-in length (l_s) is associated with the strength of the cantilever beams. The load on the longwall shields is related to the beam deflection and the deadweight of the cantilever beams in the worst case. The mechanical behaviour of a cantilever beam depends on the block size and mechanical properties of the crosscut rock joints in the beams. A strong cantilever beam would result in a large overhang over the longwall shields, which may collapse in a violent manner when it fails. Weak cantilever beams are more favourable than strong ones for longwall mining. The bulking effect of the cave-in materials cannot be taken into account in UDEC modelling. Therefore the stope void is not fully filled in the simulations and the UDEC modelling may overestimate the deadweight of the cantilever beams formed during periodic cave-ins.

Figure 7.5 presents the simulation results of the load on the longwall shield and the field measurement data. The field measurements of the shield load were conducted when the stope face had reached approximately the middle of panel C6 (Figure 3.1). The results presented in the figure correspond periodic cave-ins in the model. The stope face advance in the figure is the total length of the mined-out panel in the model. As mentioned above, the longwall shield was modelled by two support elements (El_1 and

El_2) connecting two stiff blocks in the roof and floor of the stope. The support elements of El_1 and El_2 are located at 1 m and 3 m respectively, behind the stope face. Element El_2 is loaded more than El_1 because of a larger beam deflection occurs at El_2. The average load of the two simulated support elements agrees quite well with the field measurement data. The approximately constant load on the shields implies that overhang of roof strata does not exist over the longwall shields and the roof cave-in continuously occurs with advance of the stope face.

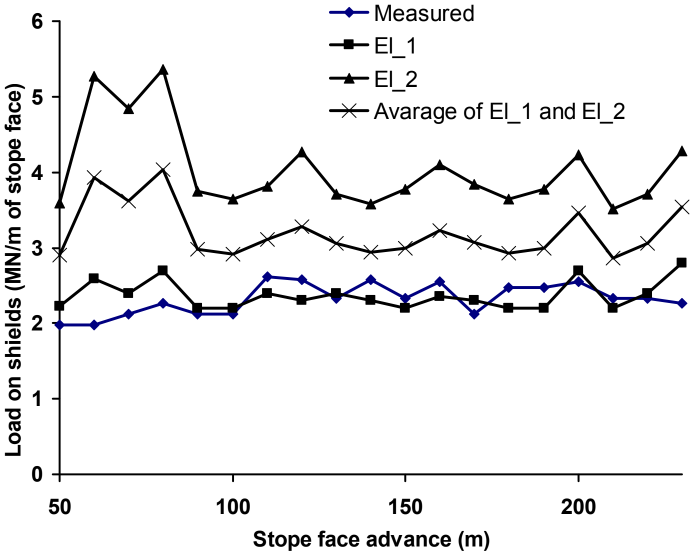

Figure 7.5 Simulated loads on longwall shields and the field measurement data

7.3 Discussion

The cavability of the roof strata is associated with the mechanical properties of the strata, the block size, the in-situ stress state and the height of the mined-out void. Beam forming and beam deflection are the major concerns in studying roof cave-ins. The aim of this section is to understand the cave-in mechanism through sensitivity analyses to the mechanical properties of the roof strata and the in-situ stress state. In the simulations for sensitivity study, the input parameters varied in the following ranges: 5, 10 and 50 GPa for the E modulus of the strata; 1, 2 and 3 m for the spacing of crosscut joints; and

K= 0.33, 1 and 2 for the in-situ stress ratio. The normal and shear stiffness of the joints, K_n and K_s, were kept constant and the cohesion and dilation angle of joints were zero in the simulations.

7.3.1 On the cave-in mechanism

The mining causes the roof strata to separate at the bedding planes. Rotation of the rock blocks form voussoir beams in the roof strata. The bending stress in the voussoir beams is related to the Young's modulus of the rock, the stiffness of rock joints and also the number (or spacing) of rock joints. Large spacing of crosscut joints and high Young's modulus of rock would result in a stiff roof beam. The numerical results reveal that stiff roof beams can sustain high load (Figure 7.6). As a consequence, the first cave-in distance (l_p) increases with the Young's modulus of the rock blocks.

Furthermore, the horizontal in-situ stress is helpful to roof stabilization. It prevents rock blocks from separating from each other whilst the roof deflects towards the stope void underneath. Accordingly, the first cave-in length increases with the stress ratio K (Figure 7.6).

The sustainable deflection of a beam refers the deflection at which buckling starts, Figure 7.7. It increases with the stress ratio K. When K is smaller than 0.3, the sustainable deflection is about 25%, which is consistent with the analytical solutions by Diederichs & Kaiser (1999a). The sustainable deflection could be larger than 100% when the stress ratio K is large enough, for instance $K > 2$. It should also be noted that rock crushing could occur for high stress ratios. For instance, at $K = 2$, the dominant failure mode could be crushing when the deflection induced stress of roof strata is beyond the crushing strength of 36 MPa, Figure 7.7.

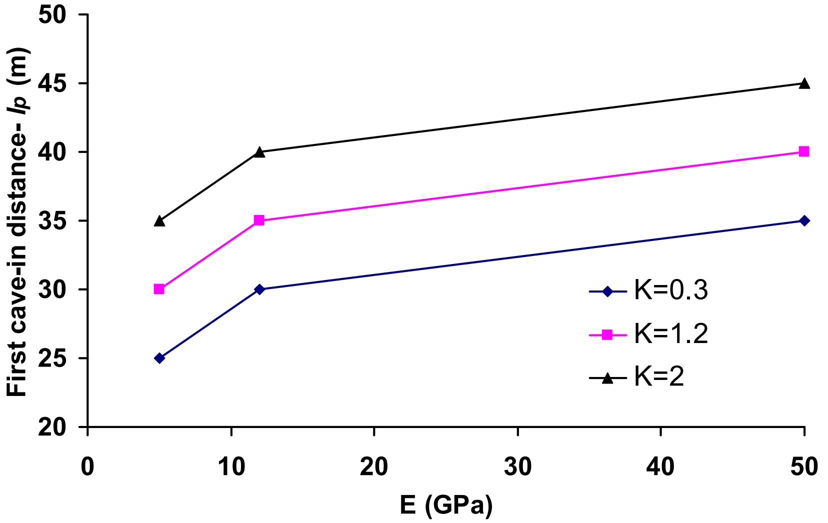

Figure 7.6 First cave-in distance versus the Young's modulus (E) of the rock blocks in the roof. The spacing of the crosscut joints is 1 m in the simulations.

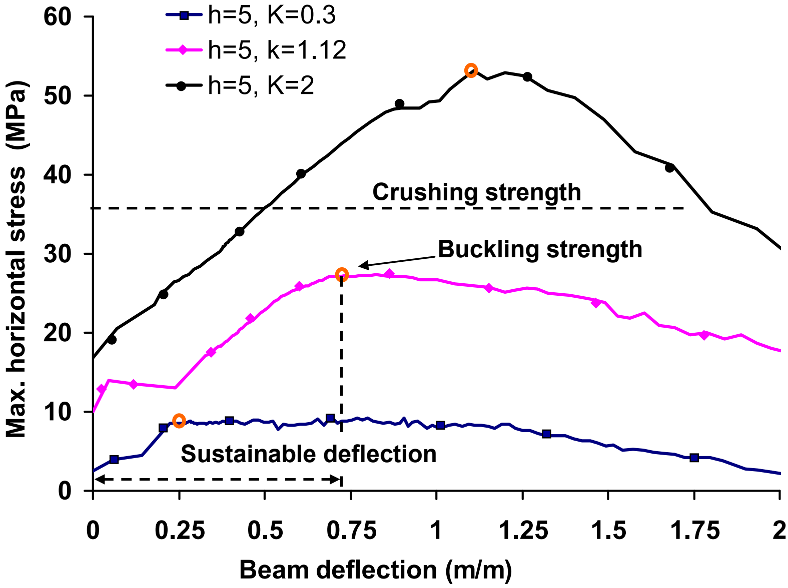

Figure 7.7 Maximum horizontal stress in a stratum versus deflection for different stress K ratio. The Young's modulus of the rock and spacing of the crosscut joints are 12 GPa and 1 m, respectively.

Figure 7.8 shows the influence of block size on the first cave-in distance. In the figure, the hydraulic radius of the block (R_b), defined as the area of the block divided by the perimeter, is used to represent the block size. The stiffness of roof beams increases with R_b and the roof deflection would be smaller. However, an increase in the horizontal in-situ stress makes the first cave-in distance less sensitive to the block size.

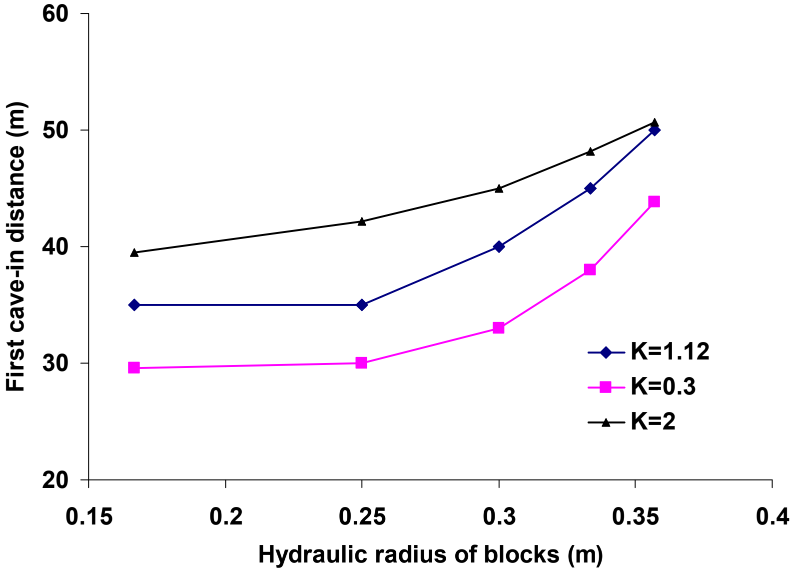

Figure 7.8 First cave-in distance versus block hydraulic radius. The Young's modulus of the beam rock is 12 GPa.

The load on longwall shields during the first cave-in is equal to the deadweight of a portion of the collapsed roof rock. Accordingly, a large first cave-in distance would result in a large shield load. During the periodic cave-ins, the shields are loaded by either the deflection of the cantilever roof beams or the deadweight of the collapsed roof rock. The shield load increases with increases in the block size and in the E modulus of the roof rock (Figure 7.9). An increase in the horizontal in-situ stress slightly increases the shield load during the periodic cave-ins.

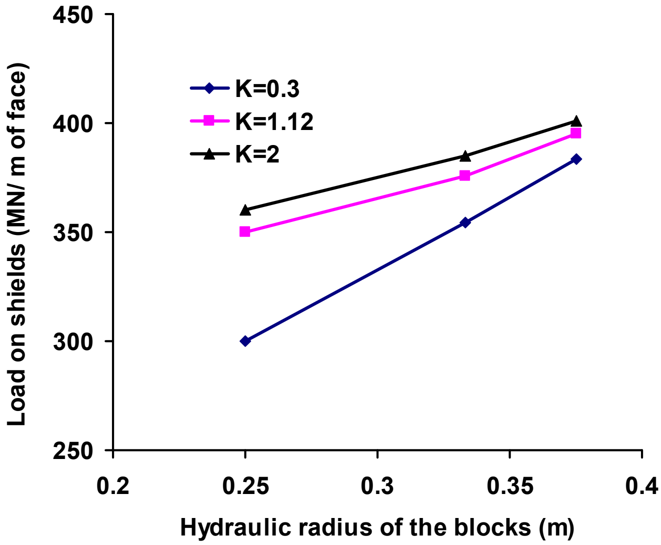

(a)

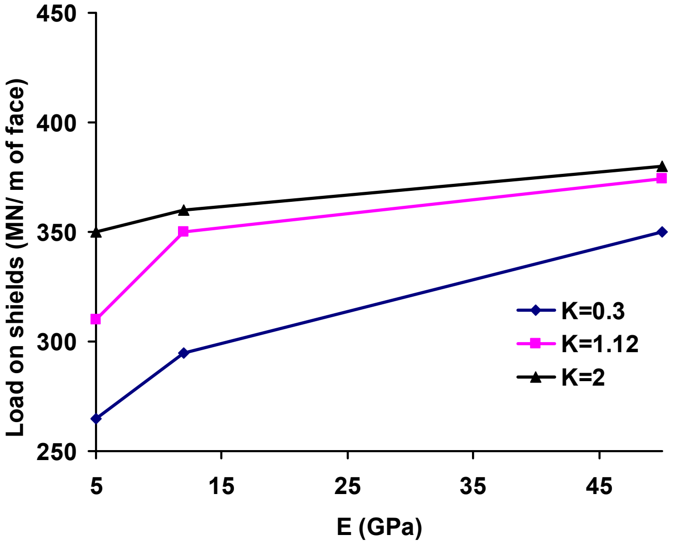

(b)

Figure 7.9 Load on longwall shields versus: (a) Hydraulic radius of blocks, for the case that E modulus of the roof blocks is 12 GPa, and (b) the E modulus of the roof blocks, when the spacing of the crosscut joints is 1 m.

7.3.2 Comparison of the continuous and discontinuous numerical modelling results

In the FLAC$^{(3D)}$ continuous model (Figure 4.1), a critical tensile strain value was utilised to identify the boundary of the cave-in region. We found that the roof strata above the stope void intend to cave in when the maximum principal strain (in tension) equal to, or larger than 5%. The maximum height of the cave-in zone is about 16 m above the stope floor. In this section, we address the similarities and differences between the FLAC$^{(3D)}$ continuous model and the UDEC discontinuous model of the study site.

In the continuous model, equivalent mechanical properties were applied to the rock mass and a strain softening constitutive model was used. The uniaxial compressive strength for the rock mass was about 8 MPa. Discontinuity elements were added in the model to simulate bedding planes in the rock mass. However, rotation of the rock blocks were not considered in the FLAC$^{(3D)}$ model.

Figure 7.10 presents the maximum horizontal stress in the roof beams versus the middle-span convergence of the stope roof during the first cave-in when the advance distance reaches l_p = 35 m in the UDEC model. It is seen in the figure the maximum horizontal stress in the first 16 m roof strata drops after its ultimate value, implying that the roof strata fail in buckling, whilst the stress in the strata above continues to increase with the roof convergence, indicating that they are stable. By considering the bulking factor, the volume of the caved-in materials from the first 16 m roof strata is large enough to fully fill the stope void. Therefore, the caved materials could provide support to the strata above and protect them from cave-in. Thus, the results of the UDEC modelling agree with the results of the FLAC $^{(3D)}$ modelling.

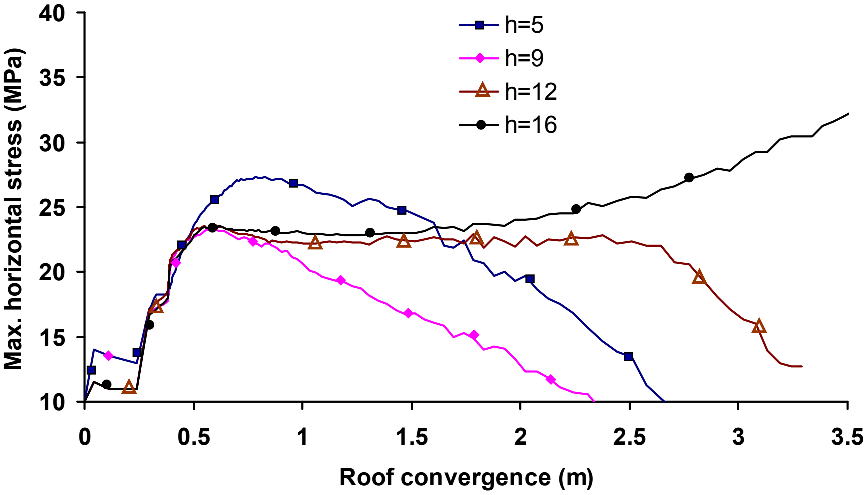

Figure 7.10 Maximum horizontal stress in the roof strata versus roof convergence when the stope face advanced from 0 (mining start) to 35 m in the panel. h refers to the height of the roof strata above the panel floor

8 Analytical methods for investigating stability of laminated roof strata above underground openings

8.1 Introduction

Underground openings are often excavated in stratified rocks, particularly in coal mines. Stratification is associated with bedding planes and foliation, which have very low tensile and shear strengths. Therefore, the mechanical response of each stratum individually influences the stability of the opening. For instance, in coal mining, the stability of the gates, tunnels, and stopes is related to the mechanical response of the immediate roof stratum to the mining activities.

Fayol (1885) claimed that the roof strata are separated from each other by deflection, and their weight is transferred to the abutments of the opening rather than carried by the beam underneath. Therefore, it is believed that the stability of the roof strata is related to the deflection of the roof beams induced by their own weight. Conventional beam theory would be applicable to investigate the stability of roof strata. However, Bucky (1931) and Bucky & Taborelli (1938) studied the behaviour of intact rock beams using physical models. They observed that a vertical crack was created in the midspan of the beam when the beam deflected. Moreover, strata usually contain crosscut joints. Thus the tensile strength of strata is almost zero in the direction perpendicular to the crosscut joint planes. The rock blocks in such stratum rotate and interlock with each other to form a jointed voussoir beam when the stratum deflects downward (Evans 1941). In a voussoir beam, a compression arch is formed as soon as deflection occurs. The arch starts in the lower portion of the beam at the abutments and rises to the upper portion of the beam at the midspan. The offset compression creates a moment in the beam which equilibrates the moment by the weight of the beam (Figure 8.1a). Generally, voussoir beams are statically undetermined (Beer & Meek 1982). Therefore, it is necessary to make some assumptions when analysing the stability of voussoir beams.

Evans (1941) developed a relationship between the vertical deflection, the lateral thrust, and stability of a jointed voussoir beam. Evans' method was later reformulated and further developed by Beer & Meek (1982), Brady & Brown (1983), Sofianos (1996), and Diederichs & Kaiser (1999a). In order to overcome the static indeterminateness of voussoir beams, assumptions have to be made regarding the thickness and geometry of the compression arch. However, there are still arguments in the matter how to determine the thickness and geometry of the compression arch (Sofianos 1999; Diederichs & Kaiser 1999b).

There have been a number of attempts to study the behaviour of voussoir beams via numerical simulations. The first well-known numerical modelling of voussoir beams was conducted by Wright (1972) with the linear elastic finite element method; his results were used by Sofianos (1996) to develop a model of voussoir beams. Sepehr and Stimpson (1988) aimed to develop a relationship between roof deflection and the spacing of the crosscut joints in horizontally laminated strata with numerical modelling. Sofianos (1996) re-evaluated the numerical results obtained by Wright (1972) and proposed a critical thickness of the compression arch for beam buckling. He claimed that the thickness of a compression arch at the abutments (n_0) is initially equal to $0.75d$, where d is the thickness of the beam. It decreases to less than $0.3d$ at the moment of buckling. He proposed a formula for the critical thickness of the compression arch which was solely a function of beam span. Sofianos & Kepenis (1998) and Nomikos et al. (2002) studied the stability of voussoir beams by numerical modelling with UDEC software, but their results on the critical thickness of the compression arch contradict the numerical results of others. Evans (1941) and Brady & Brown (1983) assumed that the initial n_0 is equal to $0.5d$. Diederichs & Kaiser (1999a) found, however, that the thickness of the compression arch is $0.75d$ in the beginning and then decreases to $0.35d$ at the moment of buckling. They used numerical modelling conducted by UDEC to prove their results. They also argued that this contradiction was due to the different discretisation methods and boundary conditions in the numerical models.

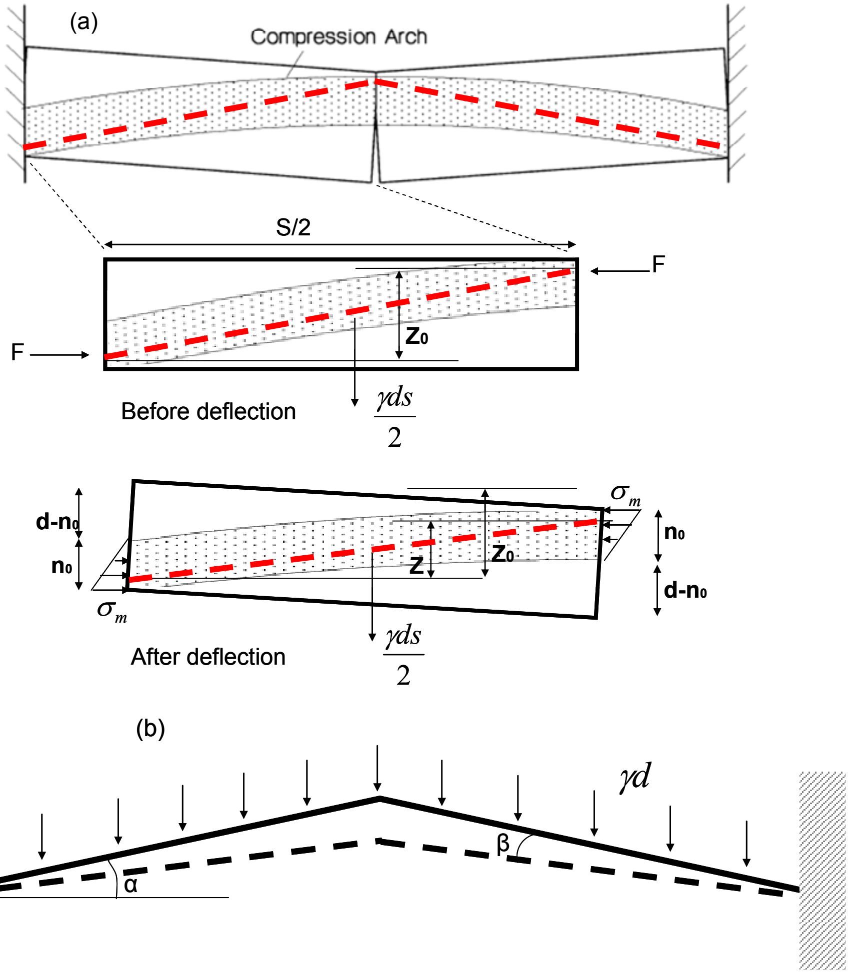

Figure 8.1 (a) Arch forming in the voussoir beams, (b) shortening of the arch axis due to beam deflection

Tsesarsky & Talesnick (2007) compared the numerical results by $\mathrm{FLAC}^{(2D)}$ and a DDA code with the laboratory centrifuge tests of jointed voussoir beams conducted by Talesnick et al. (2007). The vertical deflections predicted by $\mathrm{FLAC}^{(2D)}$ and DDA are reasonably comparable with the centrifuge model. However, the accuracy strongly depends on the stiffness of the crosscut joints. The thrust force induced by compression arch is relatively lower in the numerical modelling than the physical modelling. The geometry of the compression arch was well predicted by $\mathrm{FLAC}^{(2D)}$.

Through laboratory tests, Sterling (1980) proposed that the failure modes of a jointed voussoir beam include buckling, lateral compression failure (crushing) at the midspan and abutments, abutment slip, and diagonal fracturing (Figure 2.4). Abutment slip is observed in low span-to-thickness ratio beams (thick beams), while crushing and buckling occur in thin beams. Ran et al. (1994) showed that if the angle of the crosscut joints with the normal of the bedding planes is less than 1/3 to 1/2 of the friction angle of the crosscut joints, the voussoir beam analogy is valid.

In summary, in spite of the substantial contributions from analytical, numerical, and laboratory investigations regarding the stability of voussoir beams, they have limitations in terms of engineering applications. The main issues here are the assumptions for the geometry of the compression arch and the method implemented to tackle the static indeterminacy of the beams, which results in controversial outcomes.

In this research, a model with assuming bilinear geometry for the compression arch is developed. The model employs an iterative method to find the statically stable situation of the beam with the theorem of minimum potential energy (Maceri 2010). This study takes into account the effect of the in-situ horizontal stresses on the voussoir beam's stability, which so far has not been considered so far by others, except in the continuous beams.

8.2 Voussoir beam model

A laminated roof stratum over an underground excavation with span of S is considered. The thickness of the beam is d while the beam rock obeys the linear elastic model. For an elastic beam without joints, the behaviour can be straightforwardly governed by elastic beam theory. The stress magnitude is related to the supporting condition of the beam ends. For an end-fixed beam, the maximum stress occurs at the abutments and the maximum deflection at the midspan, which are expressed, respectively by (Obert & Duval 1966):

$$\sigma_{\max}^{f} = \frac{\gamma S^2}{2d} \tag{8.1}$$

$$\delta_{m}^{f} = \frac{\gamma S^4}{32Ed^2} \tag{8.2}$$

where E is the Young's modulus of the beam rock and γ is the unit weight of the beam rock. The maximum stress at the midspan is half of that at the abutment.

Yield is assumed to occur when the tensile stress at the abutments reaches the tensile strength of the rock. After vertical tensile fracturing at the abutments, the beam becomes simply supported if neither slip occurs at the abutment joints (Diederichs & Kaiser 1999a) nor horizontal stress is applied to the beam. The maximum tensile stress at the midspan of a simply supported beam (pinned-end) can be obtained as follows:

$$\sigma_{\max}^{p} = \frac{2\gamma S^2}{3d} \tag{8.3}$$

Here, the maximum tensile stress in the beam is higher than that for the end-fixed condition, which causes the first fracture to occur at the midspan of the beam. Afterward a series of subsequent fractures are created along the beam (Sterling 1980), so that a voussoir beam is formed.

The following assumptions are made in the development of the model. The model is developed in two dimensions and assumes the out-of-plane thickness of the beams is 1 m. The beam consists of two blocks with three joints that are located at the abutments and midspan (Figure 8.1). It is assumed that the stress is distributed triangularly in the cross-sections of the beam at the abutments and midspan. Stress distribution within the beam forms a compression arch which starts from the lower portion of the beams in the abutments and reaches the upper portion of the beam at the midspan. An arch axis is defined which represents the locations where the arch force (F) acts at the cross-sections of the beam, the red line in Figure 8.1a. The arch force (F) is calculated by multiplying the compression arch stress by its thickness at the cross-sections of the beam and F is constant all along the beam.

The thickness of the compression arch is equal at the abutments and midspan of the beam; although it varies along the beam. The thickness of the compression arch in the abutments and midspan (n_0) is unknown at the beginning and is obtained by an iterative method using the theorem of the minimum potential energy stored in the voussoir beam. For the sake of simplicity, a bilinear geometry is assumed for the arch axis (Figure 8.1b). In the previous researches (Sofianos 1996; Diederichs & Kaiser 1999a), a parabolic geometry was assumed for the arch axis. For beams with a thickness much less than the beam span, however, its approximation with a bilinear function would not cause significant error in the outcomes of the model. With regard to the sketch of the arch axis in Figure 8.1b, the shortening of the arch axis generates the force of F which allows the arch to carry the vertical load of the beam weight. Owing to the vertical crosscut joints in the abutments and midspan, the arch force of F is horizontally acting at the location of crosscut joints.

The height of the arch axis is associated with the thickness of both the compression arch at the abutments and midspan and the beam. The primary height of the arch axis (Z_0) is defined as:

$$Z_0 = d - \frac{2}{3} n_0 \tag{8.4}$$

and the shortening of the compression arch means the height decreases to Z (Figure 8.1a).

Before the shortening of the compression arch, the lines of the arch axis make an angle of α from the horizontal line whereas it decreases to α-β after shortening (Figure 8.1b). It should be noted that α is equal to $atan(2Z_0/S)$. Assuming the elastic behaviour of the beam rock, the arch force (F) is calculated by considering the amount of the shortening induced at the arch axis. Therefore, the force of the compression arch is calculated by:

$$F = \frac{AE}{\cos(\alpha - \beta)} [1 - \frac{\cos(\alpha)}{\cos(\alpha - \beta)}] \tag{8.5}$$

where E is the Young's modulus of the beam rock and A is the average area of the cross-sections of the compression arch all along the beam.

Numerical simulations have revealed that the thickness of the compression arch varies along the beam. The thickness of the compression arch (n) starts to increase from n_0 at the abutments to d with an increase in the distance from the abutments. After that it is constant and then it decreases again with when approaching the midspan. In the midspan it is almost equal to n_0 again (Figure 8.2). The detail of the numerical simulations is presented in section 8.4. Based on the numerical results, the average thickness of the compression arch along the beam is 1.5-1.8 n_0 when the compression arch thickness in the abutment (n_0) is smaller than 0.67-0.55d. In this study the average thickness of the compression arch is assumed to be equal to $1.8n_0$ when $n_0 \leq 0.55d$ and otherwise it is equal to d. Therefore:

- if $n_0 \leq 0.55d$ then $A = 1.8n_0$
- if $n_0 > 0.55d$ than $A = d$

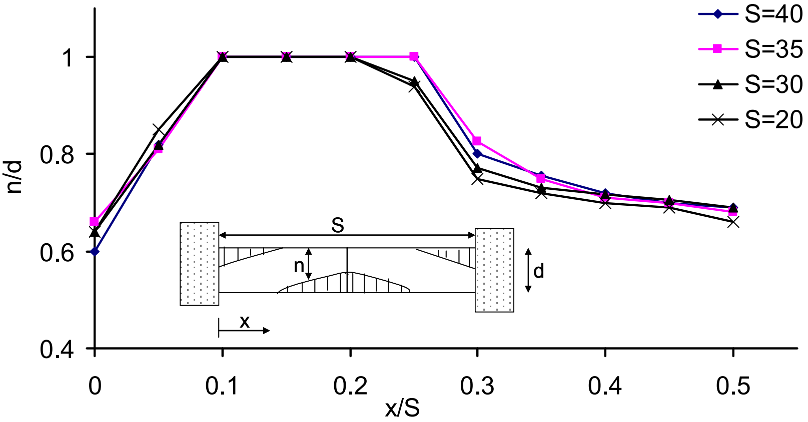

Figure 8.2 variation of the thickness of the compression arch along beams with Young's modulus of 40 GPa

With regard to the sketch of the beam (Figure 8.1b), in the static equilibrium condition, after the compression arch is deformed and shortens, the moment induced by the beam weight is equal to the moment induced by the couple force of F. Hence:

$$F = \frac{\gamma d S}{4\tan(\alpha - \beta)} \tag{8.6}$$

With substituting of (8.5) in (8.6), it is obtained that:

$$Q(\beta) = \frac{\gamma S d}{4AE} - \tan(\alpha - \beta)[\frac{1}{\cos(\alpha - \beta)} - \frac{\cos(\alpha)}{\cos(\alpha - \beta)^2}) = 0 \tag{8.7}$$

This equation could be used to find the deformation of the compression arch i.e. β and after that the arch force (F) can be calculated via Eq. (8.5). Eq. 8.7 does not have an analytical solution, so a numerical method like the Newtown-Raphson method (Thomas 2011) could be used.

As mentioned before, the thickness of the compression arch in the abutments and midspan (*n_0*) and, as a consequence, α at the moment of the static equilibrium are unknown. Considering the thickness of the beam and the geometry of the compression arch, there are a number of different possible values for *n_0* and α which could satisfy the static equilibrium condition, i.e. Eq. (8.7). Only one of them, however, is valid on the basis of the theory of minimum potential energy. The theory states that the most stable condition is reached when the potential energy stored in a system is minimal while the second deviation of the potential energy function is more than zero, i.e. the function has concave shape (Maceri 2010). The potential energy of a jointed voussoir beam (*J*) is calculated by:

$$J = FS[\frac{1}{\cos(\alpha - \beta)} - \frac{1}{\cos(\alpha)}] - \frac{\gamma d S^2}{4}[\tan(\alpha) - \tan(\alpha - \beta)] \tag{8.8}$$

The stored potential energy in the beam should be calculated for different α which satisfy the equilibrium equation, i.e. Eq. (8.7). The one with the lowest potential energy stored at the beam is the answer.

In order to present the calculation method in a clear way, the developed analytical method is summarised in a flowchart (Figure 8.3). At first it is assumed that the thickness of the compression arch in the abutments and midspan (*n_0*) is equal to the beam thickness. The thickness of the compression arch is then reduced by 90% per each step of the calculation until it is very small. Before Eq. (8.7) is solved for an α, it is checked that the equation has an answer in the range 0≤β≤α/2 by the intermediate value theorem of calculus (Thomas 2011). The configuration of the beam with *n_0* or α which results in equilibrium and has the minimal stored potential energy in it is the answer.

In order to investigate the stability of the voussoir beams, it is necessary to calculate the factor of safety for the three types of failure mode, namely buckling, crushing, and slipping (Figure 2.4).

The factor of safety for crushing failure at the abutment and the midspan can be obtained by comparing the stress in the compression arch at the abutments and midspan of the beam with the uniaxial compression strength of the rock (σ_{ci}). As stated previously, the stress distribution at the crosscut joints is triangular. The maximum abutment stress is calculated by

$$\sigma_m = \frac{2F}{n_0} \tag{8.9}$$

and then the factor of safety against crushing at the abutments and midspan of the beam is calculated by:

$$FS_{cr} = \frac{r\sigma_{ci}}{\sigma_m} \tag{8.10}$$

where *r* is a constant which represents the fraction of the uniaxial compression strength of the rock that can be used as the crushing strength. Alejano et al. (2008) suggested *r = 60%*.

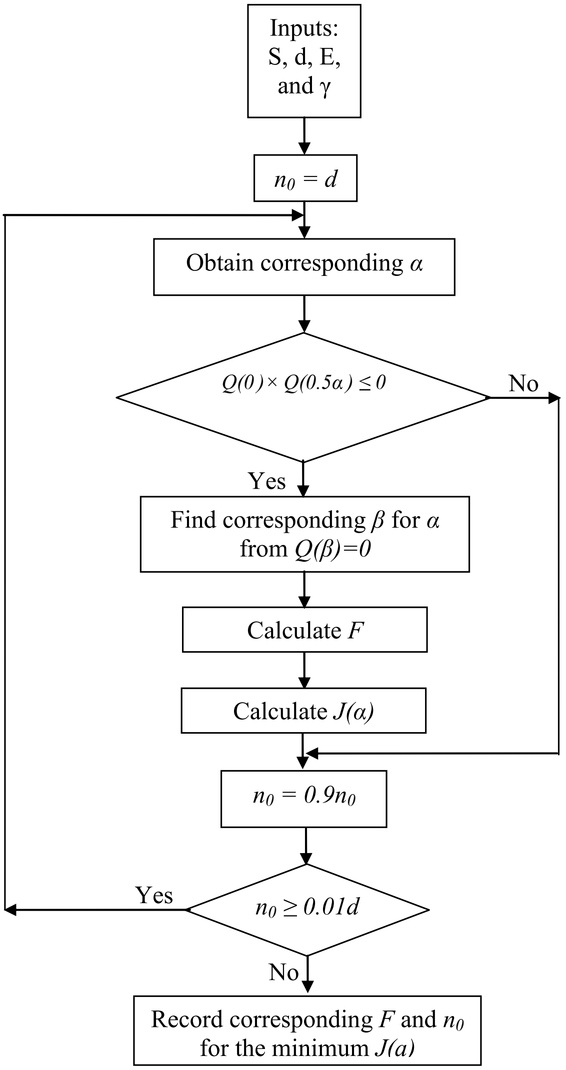

Figure 8.3 A flowchart for stability analyses of voussoir beams.

The sliding failure mode occurs if the frictional resistance of the crosscut joints is not sufficient to prevent the block from sliding at the abutments. The factor of safety for the sliding failure of the beams can be obtained by:

$$FS_{sl} = \frac{2\sigma_m n_0}{\gamma S d} \tan \phi \tag{8.11}$$

where ϕ is the friction angle of the crosscut joints of the beam.

In this study, the factor of safety for the buckling failure of the beam is defined as the ratio of the maximum stable span of the beam against buckling failure mode (S_{ult}) to the current span of the beam (S):

$$SF_{bk} = \frac{S_{ult}}{S} \tag{8.12}$$

S_{ult} can be obtained by the proposed algorithm (Figure 8.3).

Figure 8.4a depicts the thickness of the compression arch in the abutment (n_0) versus the beam span. For the sake of the comparison, both the beam span and the thickness of the compression arch are normalised to the thickness of the beam. The unit weight of the beam rock is equal to 27 KN/m^3. In Figure 8.4a, it is evident that the maximum thickness of the compression arch is equal to *0.45d* when the shortening of the compression arch is negligible. When the beam span increases, the thickness of the compression arch decreases until it reaches *0.375d* at the moment of the buckling failure. Moreover, it is shown that the maximum stable span of the beam increases with the Young's modulus. The ultimate thickness of the compression arch is not associated with the Young's modulus of the beam rock.

In the linear part of Figure 8.4a there is a slight fluctuation in the graph which might be a numerical noise induced by either iterative method of calculation or by numerically solving of the equilibrium equation, Eq. 8.7.

The maximum abutment stress (σ_m) increases with the span of the beam and reaches its maximum value at the maximum stable span of the beam against buckling mode of failure (S_{ult}) (Figure 8.4b). Increasing the Young's modulus also causes the maximum abutment stress to decrease slightly.

(a)

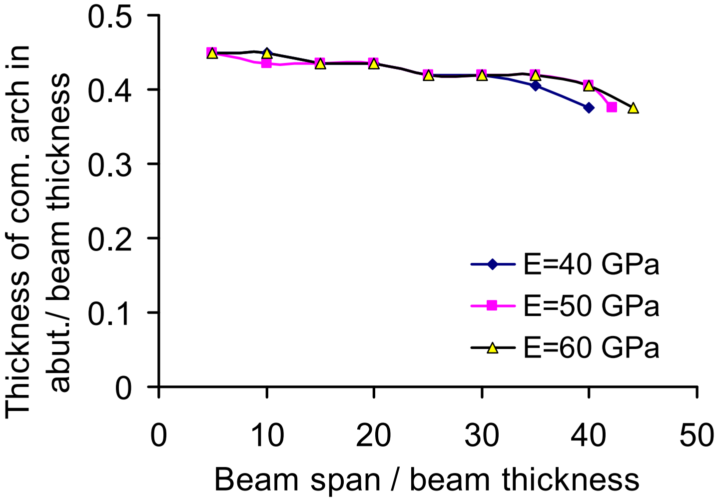

(b)

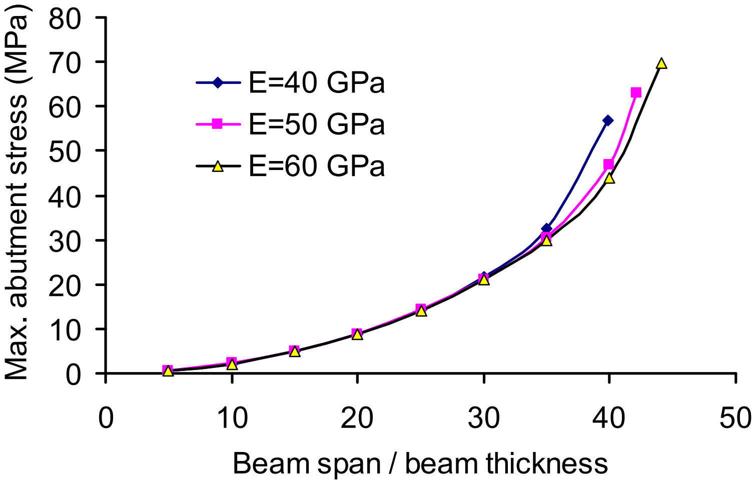

Figure 8.4 (a) Thickness of the compression arch in the abutments (n_0) and (b) maximum abutment stress versus the beam span for different Young's modulus of the rocks.

8.3 Voussoir beams subjected to horizontal stress

For underground structures constructed in stratified rocks, the horizontal stress is helpful to stabilise the roof strata. However, the method developed in the previous section does not take into account this factor. The major issues in developing an analytical approach for voussoir beams subjected to in-situ horizontal stress is how the horizontal stress helps the beam's stability and what the boundary conditions of the voussoir beams are when the stress is imposed on the beam. The rectangular cross section of the beam at the abutments prevents it from being a perfectly moment free boundary. Therefore, they cannot rotate without any resistance at the abutments and midspan. In addition, horizontal stress helps prevent joint opening during bending. Careful numerical simulations of the voussoir beams subjected to horizontal stress have showed that end-fixed boundaries are preferable compared to pinned-end boundaries for beams if no slipping occurs at the crosscut joints. The details of the numerical modelling are presented in the next section. In order to study of the stability of voussoir beams subjected to horizontal stress, the classic continuous beam approach for the beam with fixed ends was implemented.

The following assumptions are taken in the development of the model. Similar to the previous section, it is assumed that rock behaves linear elastically. The beam contains three crosscut joints at the abutments and the midspan. The joints are purely frictional without tensile strength. The beam is fixed at the abutments. The free diagram of the beam is presented in Figure 8.5a. The out-of-plane thickness of the beam is assumed 1 m.

Timoshenko (1961) proposed an approach to calculate the deflection and bending moments, as well as the stability of the beam subjected to horizontal axial and lateral loads. The deflection of a statically undetermined structure can be investigated by the superposition method. Hence, the beam with the free diagram presented in Figure 8.5a is divided into two different statically determined beams, Figures 8.5b and c. Details of the deflection equations for the continuous beams can be found in (Timoshenko 1961).

The deflection profile of the beam as illustrated in Figure 8.5b can be obtained by:

$$y = \frac{\gamma d S^4}{16EIu^4}[\frac{\cos(u-2ux/S)}{\cos(u)} - 1] - \frac{\gamma d S^2}{8EIu^2} x(S-x) \qquad (8.13)$$

where I is the moment inertia of the beam and u is:

$$u = \frac{S}{2}\sqrt{\frac{P}{EI}} \tag{8.14}$$

Here, P is the resultant axial force in the beam, which is expressed by $P = \sigma_{xx}^{in-situ} \times d$.

The bending moment of the beam is calculated by:

$$T = \frac{\gamma d S^2}{4}[1 - \frac{\cos(u - 2ux/S)}{\cos(u)}] \tag{8.15}$$

For the beam presented in Figure 8.5c, M_0 is added to the ends of the beam to capture the end-fixed condition of the original beam (Figure 8.5a). Therefore, the magnitude of M_0 is obtained from the condition that the rotation of the beam ends produced by both the uniform load along the beam and horizontal stress is eliminated by the moments acting at the beam ends. Then:

$$M_0 = \frac{\gamma d S^2}{12}\frac{ux(u)}{\tan(u)} \tag{8.16}$$

where

$$x(u) = \frac{3[\tan(u) - u]}{u^3} \tag{8.17}$$

The deflection of the beam in Figure 8.5c induced by constant moments acting at its ends is calculated as follow:

$$y = \frac{-1}{EI}[\frac{M_0 x^2}{2} - \frac{M_0 S x}{2}] \tag{8.18}$$

The bending moment of the beam is also constant along the beam and is equal to M_0.

Eventually, the bending moment and deflection of the beam in Figure 8.5a are equal to the summation of the bending and deflection of the beams in Figures 8.5b and c with consideration of their direction. The maximum deflection of the beam in Figure 8.5a also occurs in the midspan while the maximum bending moment of the beam is situated at the abutments.

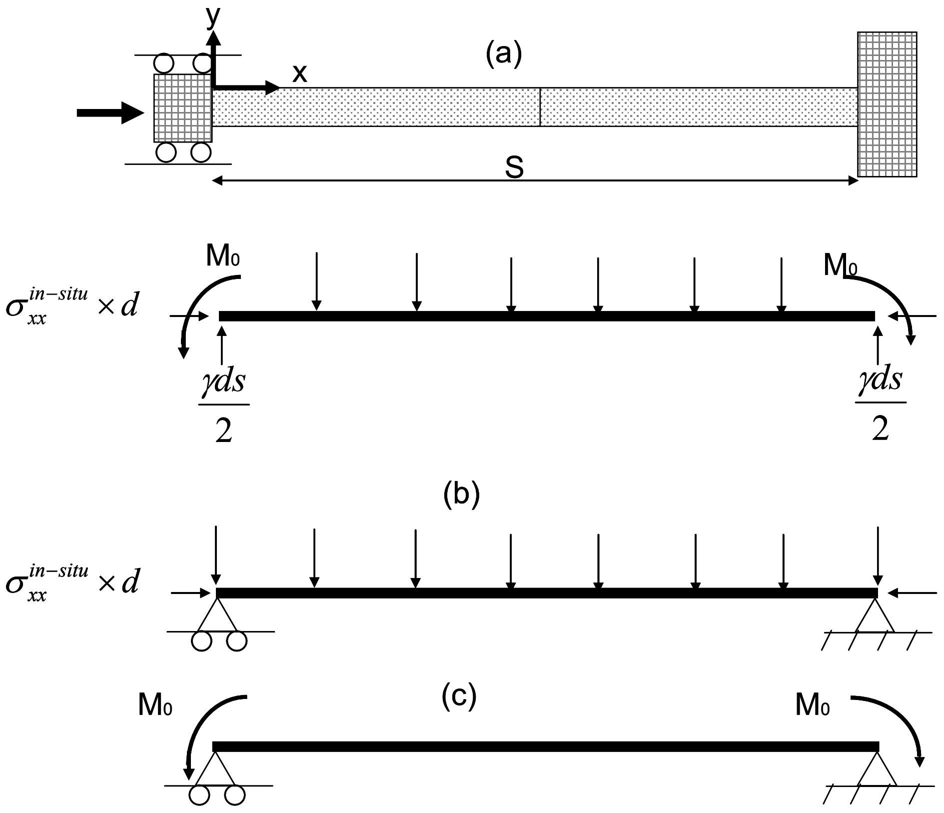

Figure 8.5 (a) The free diagram of the roof voussoir beam when subjected to in-situ horizontal stress. The statically undetermined beam in (a) is decomposed to two statically determined beams in (b) and (c).

The tensile stress induced by the beam deflection would cause the crosscut joints in both abutments and midspan to open. When the open length of the crosscut joints is sufficiently large, the end-fixed boundary conditions would be transformed into pinned-end boundaries. Therefore, the beam loses the confines provided by the horizontal stress, and ultimately becomes unstable.

The maximum bending moment of the beam in Figure 8.5a, occurs at the abutments, is calculated as follow:

$$T_{\max} = M_0 \tag{8.19}$$

and the maximum deflection of the beam, occurring at the midspan, is calculated as follows:

$$\delta = y_{\max} = \frac{M_0 S^2}{8EI} - \frac{5\gamma d S^4}{384EI} \frac{12(2\sec(u) - 2 - u^2)}{5u^4} \qquad (8.20)$$

The crosscut joints at the abutments start to open when the minimum bending stress is equal to zero. The minimum bending stress of the beam is expressed by:

$$\sigma_{\min}^{ab} = \sigma_{in-situ}^{xx} - \frac{T_{\max} d}{2I} \qquad (8.21)$$

The abutment joints will open when $\sigma_{\min}^{ab} \leq 0$. The open length of the abutment joints is obtained by:

$$l_{open} = \frac{d}{2} - \frac{I\sigma_{in-situ}^{xx}}{T_{\max}} \qquad (8.22)$$

As mentioned previously, when the open length of the beam joints is large enough the beam's end-condition transfers to a pinned-end and the beam loses the confinement provided by the horizontal stress. Therefore, in this study a critical open length of the abutment joints is used to evaluate the beam's stability against buckling. It is assumed that when $l_{open} \geq 0.35d$, the beam buckles.

The maximum stable span of the beam against buckling (S_{ult}) obtained by such criteria should be used in Eq. (8.12) to calculate the buckling factor of safety. For calculating the factor of safety for beams against the crushing mode of failure (Figure 2.4b), the maximum abutment stress is obtained by:

$$\sigma_{\max}^{ab} = \sigma_{in-situ}^{xx} + \frac{T_{\max} d}{2I} \qquad (8.23)$$

and similarly to Eq. (8.10) the factor of safety against crushing mode of failure is calculated by:

$$FS_{cr} = \frac{r\sigma_{ci}}{\sigma_{\max}^{ab}} \qquad (8.24)$$

where $r=0.6$.

In order to further investigate the behaviour of voussoir beams subjected to in-situ horizontal stress, the developed method is implemented on a beam with a Young's modulus of 40 GPa and with a beam rock unit weight of 27 KN/m^3. Figure 8.6 depicts the influences of the horizontal stress on the maximum abutment stress ($\sigma_{\max}^{ab}$) versus the beam span. Increasing the beam span exponentially increases the abutment stress induced by the beam bending. In beams subjected to a higher horizontal stress, however, the maximum abutment stress rises more as the span of the beam increases. In addition, the maximum stable span of the beams against buckling mode of failure increases with the horizontal stress.

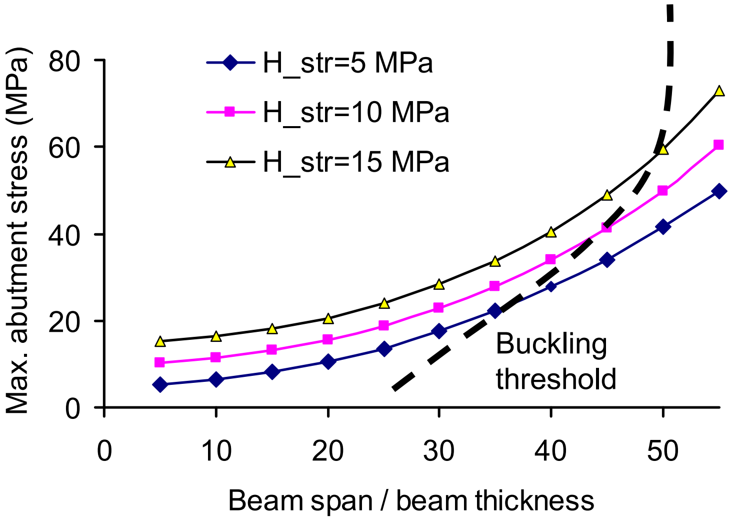

Figure 8.6 Maximum abutment stress versus span of a beam for different in-situ horizontal stresses.

Figure 8.7 shows the open length of the abutment joints versus the beam span. It is clear that the maximum length of the open joint calculated with the developed method never exceeds *0.5d*. With *0.35d* as the threshold length of the open joint for the buckling of the beam, it is clear that the maximum stable span increases with the horizontal stress.

As mentioned previously, the validity of the assumed end condition for beams is related to the open length of the crosscut joints in the abutments and midspan. After the crosscut joints are opened, the beam's behaviour might deviate from a purely end-fixed beam to a pinned-end beam.

Figure 8.8 depicts the midspan deflection of the beam versus the beam span for different magnitudes of horizontal stress. The higher the horizontal stress, the greater the deflection in the beam is for a specific span. This phenomenon is more obvious as the beam span increases.

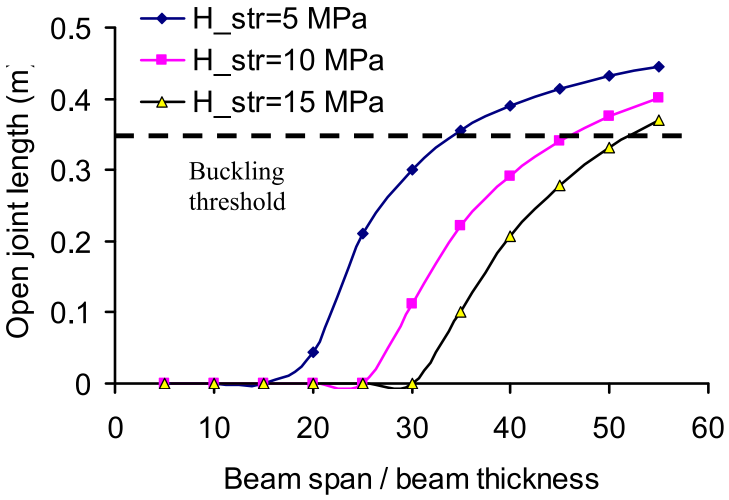

Figure 8.7 The open length of the abutment joint of a beam for different in-situ horizontal stresses.

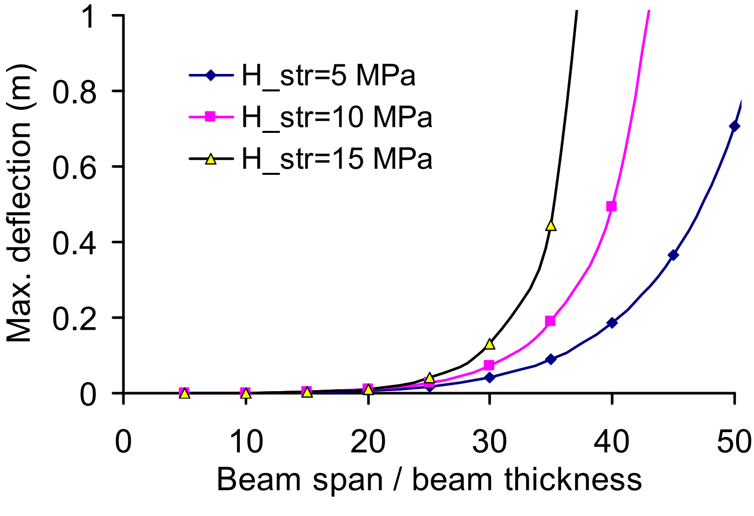

Figure 8.8 Deflection of a beam with different in-situ horizontal stresses.

8.4 Numerical verification of voussoir beam models

Numerical simulations were used to verify the models developed for the jointed voussoir beams. The numerical simulations should consider the real behaviour of the jointed voussoir beam in order to be comparable for verification purposes. As mentioned in the introduction, a number of numerical simulations have been conducted to study the mechanical behaviour of voussoir beams. Sofianos & Kapenis (1998) and Nomikos et al. (2002) assumed a rigid abutment with deformable beam rock and joints with a high normal stiffness. Abutment joints have high shear strength, which prevents them from sliding. In addition, they assumed zero friction and zero cohesion for the midspan joint. The high normal stiffness of the abutment joints results in a good agreement between the analytical and numerical methods in terms of the abutment stress induced by deflection. This may result in a lower deflection prediction than in reality. Diederichs & Kaiser (1999a) argued that rigid abutments lead to the inaccurate prediction of moment arms (Z) and the deflection of the beam. To improve the accuracy of the numerical model, they considered deformable abutments with high Young's modulus and purely frictional joints at the abutments and the midspan. They assumed, however, that abutment joints have a high normal stiffness of 100 GPa/m.

Based on the above argument, the discrete element code UDEC was used in this study to verify the developed methods. The simulations were conducted in a manner as close to reality as possible. The vertical joints were assumed to be purely frictional surfaces, whereas the beam blocks and the abutments were deformable and had same Young's modulus. Geometry similar to that of the analytical model was used in the UDEC models. The beams consisted of two blocks with vertical joints at the abutments and the midspan (Figure 8.9)

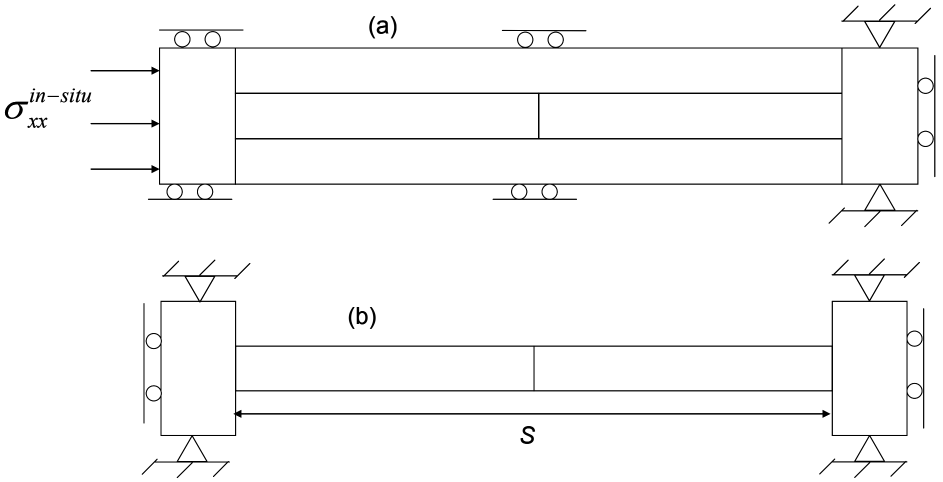

Figure 8.9 Geometry and boundary condition of the voussoir beam models in UDEC: (a) the preliminary equilibrium initiation model, (b) beam generation model.

During the numerical simulations, the unit weight of the blocks was assumed to be 27 KN/m^3, and a high frictional angle (70°) was assumed for the joints in order to prevent block sliding. The simulations were conducted for beams with different spans. The numerical models were divided into two groups according to the applied in-situ horizontal stresses. In the first group, the in-situ horizontal stress was zero, and in the second group it was not zero. In order to simulate beam loading as close as possible to the roof of underground openings, the modelling for each beam was conducted in two steps. First, a block (Figure 8.9a) was constructed and the model was run to equilibrium. It should be noted that in the case of existing in-situ horizontal stress, the left-hand boundary in Figure 8.9a is subjected to horizontal stress, whereas in the case without horizontal stress the left- and right-hand boundaries are similarly fixed in the horizontal direction. After equilibrium, the upper and lower blocks of the model were deleted and the left-hand boundary was fixed in both the horizontal and vertical directions. Later, the model was again run to equilibrium. The numerical results are presented in the following sections.

8.4.1 Voussoir beams without horizontal stress

In these simulations, the normal stiffness of the crosscut joints was assumed to be 100 GPa/m. The numerical results for the maximum stable span of the beam against buckling mode of failure and the maximum abutment stress acceptably match with the developed method (Figures 8.10 and 8.11).

The thickness of the compression arch at the abutment (n_0) is in good agreement in trend. The model predicts smaller thickness of the arch in the abutments than the numerical simulations (Figure 8.10). It might happen because of the nonlinear stress distribution at the abutment joints while in the developed method it has a triangular shape. The major reason, which causes the deviation of the numerical and analytical results, is block overlapping which is allowed in the numerical simulations with UDEC (ITASCA 2010). In UDEC, in order to capture the interaction of the blocks, they allowed to penetrate into each other with an infinitesimal size (overlapping). The block penetration generates the interaction stress between the blocks in the model. The penetration size depends on the size of the blocks in the model. Block overlapping would cause a large connection area between the beam and abutments. Therefore, the thickness of the compression arch obtained from the numerical simulations is larger than the reality.

The maximum abutment stress calculated by the model deviates from the numerical results when the beam span increases (Figure 8.11).

Generally, it can be said that the analytical model captures the behaviour of voussoir beams well enough and can be applied to the stability analysis of roof strata of underground openings in stratified rocks.

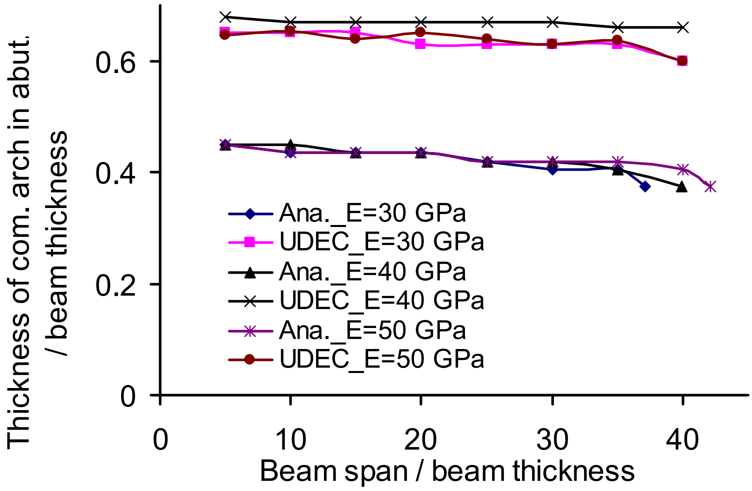

Figure 8.10 Comparison of the thickness of the compression arch obtained by numerical and analytical methods.

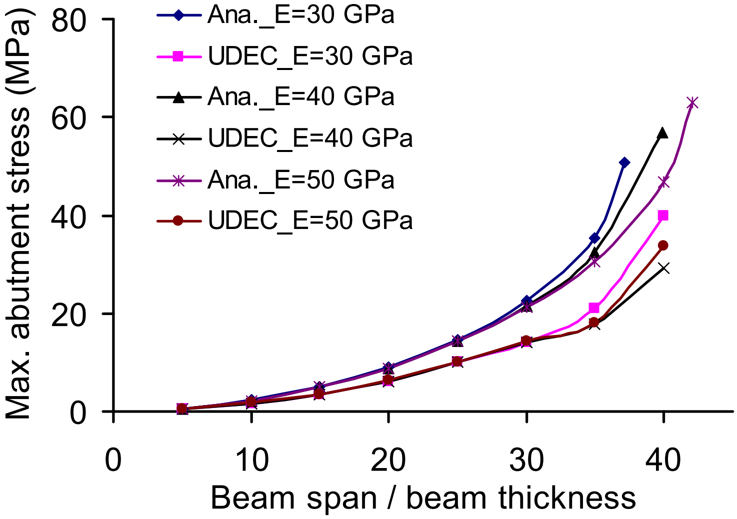

Figure 8.11 Comparison of the maximum abutment stress obtained by numerical and analytical methods.

8.4.2 Voussoir beams subjected to in-situ horizontal stress

In these simulations, the normal stiffness of the crosscut joints is 20 GPa/m. Figure 8.12 presents the maximum abutment stress ($\sigma_{\max}^{ab}$) changes versus the span of the beams for different horizontal stresses. The developed method well predicts the maximum abutment stress of the beam for different spans. At the moment of buckling, the maximum abutment stress is slightly larger than the value obtained by the numerical simulations. The buckling criterion is also shown in Figure 8. 12. The maximum stable span of the beam obtained via UDEC simulations and the developed model are, in fact, in close correlation.

Figure 8.13 shows the open length of the abutment joint versus the span of the beam for different horizontal stresses. When the magnitude of the horizontal stress is fairly low (in this case, lower than 5 MPa), the calculated open joint length perfectly matches the numerical results. The open joint length obtained by the developed model, however, deviates slightly from the numerical results when the horizontal stress rises.

The midspan deflection of the beam obtained from the numerical simulations coincides fairly well with the analytical model when the horizontal stress is low (Figure 8.14). For a large in-situ horizontal stress, the developed analytical model predicts more deflection than the numerical results. This mismatch is related to the differences between the boundary conditions of the analytical and the numerical models. In the analytical model, the horizontal force imposed to the beam is always constant during the beam deflection while in the numerical model with deflection of the beam, the vertical crosscut joints in the abutments are opened and the amount of the horizontal force imposed to the beam decreases.

Generally, the results of the numerical simulations are in good agreement with the analytical method when it is assumed that the beam has end-fixed boundaries. The horizontal stress in the beam confines it and prevents the crosscut joints from separating.

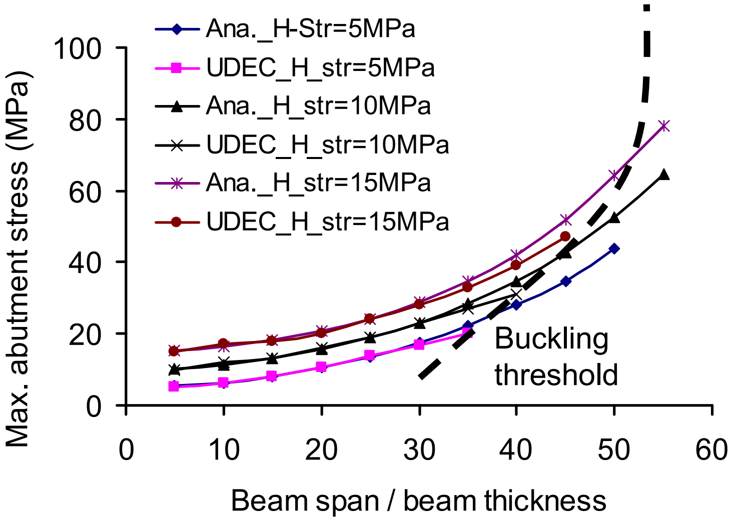

Figure 8.12 Comparison of maximum abutment stress obtained by numerical and analytical methods for different in-situ horizontal stresses.

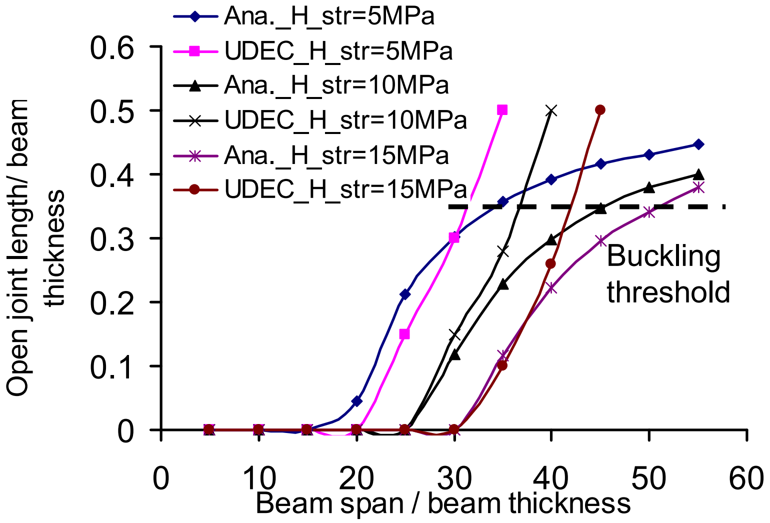

Figure 8.13 Comparison of the open length of the abutment joint obtained by numerical and analytical models.

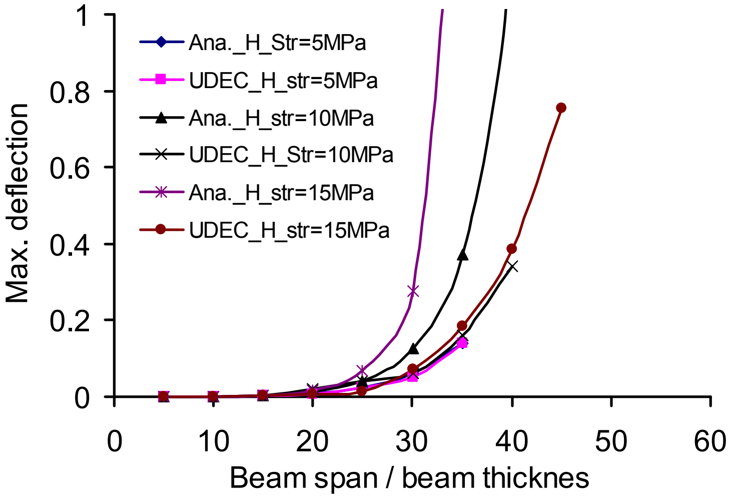

Figure 8.14 Comparison of the midspan deflection of a beam obtained by numerical and analytical methods.

8.5 Discussion

In this section, the developed method is applied to the study of the stability of some specific beams, and the stability of beams with different geomechanical conditions is discussed. The developed method is implemented to study the stability of a beam with $E = 50\ GPa$ and contains cohesion-free crosscut joints while subjected to 0, 5, 10 and 15 MPa in-situ horizontal stresses. The uniaxial compression strength of the beam rock is assumed to be 70 MPa with $r = 60\%$. The friction angle of the crosscut joints is assumed to be 30º in order to determine the factor of safety for sliding at the abutments.

For the beam with zero horizontal stress, when the beam span is increased, the factor of safety for sliding increases whereas it decreases for the crushing and buckling failure modes (Figure 8.15). Assuming the acceptable factor of safety for the design of the beam is one, the maximum stable span of the beam is 35 m.

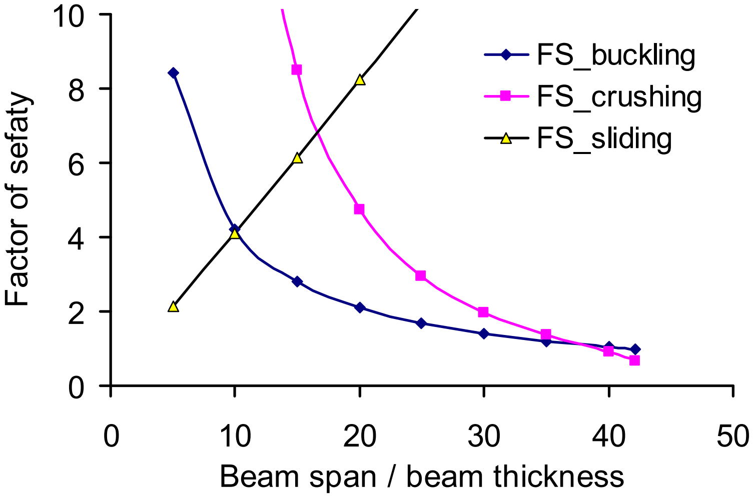

Figure 8.15 Factor of safety for a beam without in-situ horizontal stress.

Applying the horizontal stress along the beam raises the factor of safety for the beams against the buckling failure modes (Figure 8.16). With the rise in the horizontal stress, the factor of safety for the crushing failure mode decreases (Figure 8.17). Assuming an acceptable factor of safety for the beam is equal to one, the failure mode of the beam changes from buckling to crushing when the horizontal stress is 15 MPa. Comparing the different factors of safety for the beam (Figures 8.16 and 17) shows that, regardless of the failure mode, the horizontal stress increases the maximum stable span of the beams.

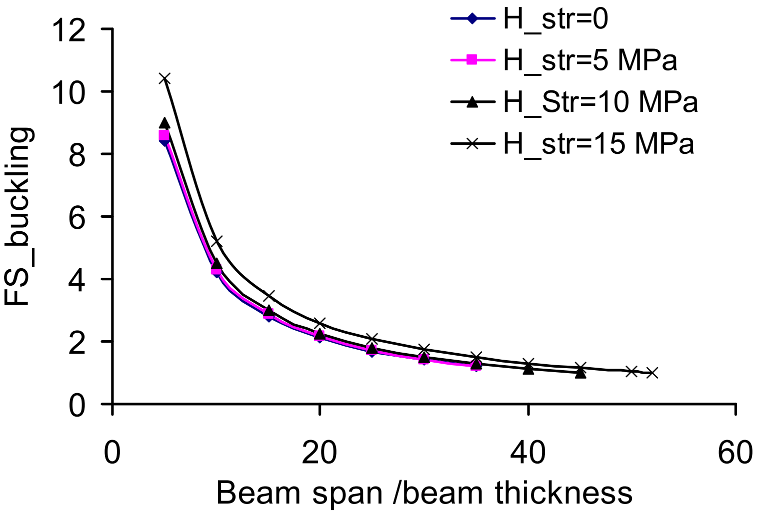

Figure 8.16 Factor of safety of a beam against buckling mode of failure for different in-situ horizontal stresses.

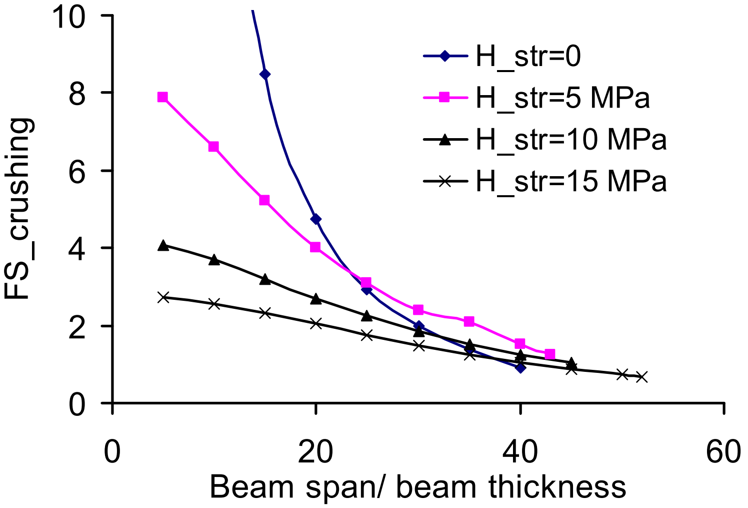

Figure 8.17 Factor of safety of a beam against crushing mode of failure for different in-situ horizontal stresses.

9 Conclusions

9.1 Conclusion remarks

The primary goal of this research was to develop a numerical approach for studying the influences of longwall mining in the host rocks, particularly at the border area of the study site, and to implement the developed approach to study the roof supporting practices in the study site. Longwall mining involves roof strata cave-in and consolidation of the caved materials under the weight of the overburden rocks. Roof strata cave-in causes stress relaxation in the surrounding rocks and helps the stability of gates and pillars. The study consists of three major parts, continuous, discontinuous numerical simulations and analytical study.

The continuous numerical simulations were conducted by a finite difference code of FLAC$^{(3D)}$. A novel algorithm was developed to simulate the longwall mining process. The algorithm considers the roof strata cave-in, fracturing and consolidation of the caved-in rocks. The caved-in roof rocks are identified by a strain-based criterion. The algorithm was implemented for numerical simulations of longwall mining and its results were used to study the roof cave-in performance, gate stability and stress changes induced by mining in the nearby rocks. Moreover, the results of the simulations were implemented in a mine-scale numerical model. The large-scale model consisted of all the longwall panels and border area of the study site. The large-scale numerical simulation was conducted to study disturbances induced by longwall mining in the panels at the border area of the mine.

In order to investigate the roof strata cave-in mechanism at the study site, discontinuous numerical simulations via UDEC code was conducted. A back-calculation method based on a statistical method was implemented to obtain the required parameters for numerical modelling. The numerical models were calibrated with the measured load of the longwall shields at the study site.

The discontinuous numerical simulations with UDEC revealed that the roof cave-in process involves with the formation and collapse of voussoir beams. Therefore, two analytical methods were developed for studying roof beams' stability in cases with and without in-situ horizontal stresses. The analytical models were calibrated with the numerical simulations conducted by UDEC.

The major conclusions from this research are as follows:

- Numerical modelling with the developed algorithm revealed that the roof strata do not cave in more than 12 m in depth over the panels. The height of the fractured zone above the cave-in rocks never exceeds 140 m in the deep panels. Extension of the disturbed zone (cave-in + fractured zones) above a panel is controlled by weak interlayers and location of the bedding planes.

- Both the field measurement data and numerical results show that loading of the rock bolts installed in gates occurs mainly during excavation of the gates. Mining in panels does not cause significant load increment in the bolts. The current width of the chain pillars, 40 m, is enough to provide protection to the gates from mining induced disturbances under an overburden of 110 m of rocks plus 250 m of ice. Under a larger overburden, panel mining would cause significant load increments in bolts.

- The size of the chain pillars has a significant influence on the stability of the gates and loading of rock bolts. In the case of thin chain pillars, longwall mining induces a shear displacement on the weakness planes between roof strata. The shear displacement causes instability problems in the gates. Therefore, the location of the weakness planes should be taken into account in the support design.

- Both the numerical investigations and in-situ measurements reveal that mining in the neighbour panel does not cause significant stress changes in the roof of the gates under an overburden of 110 m of rock plus 250 m ice. The chain pillar between two adjacent panels provides good protection to the main gate in this condition. Under larger overburdens longwall mining causes significant stress changes at the roof of the main gates.

- The maximum vertical stress ahead of the stope face reaches the maximum of 3.25 times the original vertical stress when the panel is shallow and the disturbed zone expands enough to reach the ground surface. For the deeper longwall panels the maximum vertical stress decreases linearly as the panel depth increases.

- The simulations show that the stress in the barrier pillars and abutment fluctuates up and down during mining because of periodic cave-in events occurring behind the longwall face. The vertical stress in the pillars decreases by about 5 MPa under an overburden of 400 m when the mined-out stopes are filled by cave-in rocks.

- A failure zone of about 12 m is found to have developed in the side wall of a barrier pillar after completion of the panel mining. A significantly large part of the barrier pillars is still intact and is able to provide protection to the border area on the opposite side of the longwall panels.

- The 3D large-scale simulation shows that a failure zone of about 10 m has developed in the wall of the main tunnels on the side of the border area after all the longwall panels have been mined out. Beyond the first 25 m from the main tunnels, the stress state in the border area remains unchanged after completion of longwall mining. Therefore, it will be possible to mine the border area in the future.

- The general significance of the large-scale simulation is that it proves that the failure zone in the host rock surrounding an underground void with a large volume is limited to a relatively small extent as long as the void is backfilled by either caved materials or other types of loose materials.

- The discontinuous numerical simulation revealed that the mechanism of the roof cave-in and loading on the longwall shields can be explained by the beam theory.

- The discontinuous simulations show that voussoir beams are formed in the roof strata above the stope void before the first cave-in occurs. This beam-forming process causes high horizontal stress concentrations in the roof strata owing to bending.

- The numerical modelling with UDEC showed that roof beam buckling is associated with the in-situ horizontal stress in the strata. The sustainable deflection of a voussoir beam is about 25% when the horizontal in-situ stress is low, whereas in high horizontal stress situations both the sustainable deflection and the buckling strength of the beams increase significantly.

- Both the numerical simulations and the field measurements at the study site revealed that the roof strata cave-in results in approximately constant loads on the longwall shields which does not change by the stope face advance.

- Numerical results suggest that strong roof strata could cause dramatic increases in the shield load. Therefore, weak roof strata are preferable to strong roofs in longwall mining.

- The proposed approach for the discontinuous numerical simulations of the roof strata is a useful tool for evaluating shield loads and can be used to determine the required load capacity of longwall shields in the design stage.

- The analytical method developed for stability analysis of voussoir beams shows that the maximum abutment stress of beams increases with the Young's modulus of rocks. Beams with high Young's modulus are stable with a large span. The developed method also reveals that in an extremely stiff voussoir beam (with high Young's modulus) the failure mode might be crushing rather than buckling.

- With horizontal stress applied along the beams, the maximum stable span of the beams increases. However, when the horizontal stress is large enough, the failure mode changes from buckling to crushing. Therefore, when the horizontal stress is high, roof beams might suddenly collapse by the crushing failure mode, whereas the maximum deflection of the beam at the moment of collapse is relatively small.

9.2 Major contributions of the thesis

The major contributions of this thesis can be summarised as follows:

- A novel algorithm for numerical modelling of the longwall mining process was proposed. The algorithm considers the roof strata cave-in and fracturing as well as consolidation of the caved-in materials under the weight of overburden rocks.

- A method was presented for using the results of detailed numerical simulations in a mine-scale numerical model.

- The statistical method of Design Of Experiment (DOE) was implemented to back-calculate the required parameters for numerical modelling. The back-calculation method is easy to follow and applicable to any back-calculations in geomechanics.

- It was proved through a comprehensive discontinuous numerical simulation that the roof strata cave-in in longwall panels could be studied by the beam theory.

- A novel analytical model was proposed to study the stability of the voussoir beams in roof strata of underground openings in the stratified rocks. This method is applicable for the beams with a low horizontal stress where the beam stability is governed by the compression arch forming within it. The model requires an iterative calculation to converge.

- A new analytical method was, also, developed to investigate the stability of the voussoir beams subjected to in-situ horizontal stresses. This method is based on the continuum beam theory.

Also, from the application perspective, the developed algorithm for the numerical modelling of longwall mining could be applied to study the longwall geomechanics and the stability analysis of gates and pillars. The presented discontinuous numerical simulation approach could be suitable for finding the required load capacity of the longwall shields during design of longwall mines. The analytical methods could be used to find the first cave-in distances of the longwall panels and then to implement it in the stability analysis of the gates.

10 Further development

Further developments, required to continue this research, are summarised as follows:

- The critical cave-in strain, used to identify the roof strata cave-in above an open stope, was obtained through back-calculations over ground surface subsidence. In order to obtain the critical cave-in strain with more accuracy, it is necessary to study the progress of the roof strata cave-in and fracturing with stope face advance. To that end, it is necessary to study roof cave-ins by mean of real data obtained from long extensometers installed along boreholes from the ground surface into the mining influenced zones. It is an expensive undertaking but would provide valuable data.

- Real time stress measurements in the roof of the gates with stope face advance would improve our understanding about the influences of the roof cave-in in nearby rocks of a longwall panel. Moreover, validation of the numerical simulations with those field data would increase the accuracy of numerical modelling.

- Longwall mining causes significant disturbances in the roof strata of gates such as horizontal and vertical stress concentrations and shearing along the bedding planes. With the developed numerical approach it is possible to describe them. A new roof support design method is required, however, to consider those results in stabilisation of gates.

- Physical modelling of the voussoir beams is required to accurately validate the developed analytical methods. In the physical modelling the variation of the compression arch thickness at the abutments and midspan should be studied in detail.

- The developed analytical methods for the voussoir beams need to further develop in order to be applicable in design of roof supporting for gates. Moreover, they could be applied further to the study of loading of longwall shields and to assess the roof cavability.

11 References

Alejano L.R. Taboada J. García-Bastante F. and Rodriguez P. (2008) 'Multi-approach back analysis of a roof bed collapse in a mining room excavated in stratified rock', *International Journal of Rock Mechanics and Mining Science*, 45, pp. 899-913.

Badr, S. Schlisser, A. Salamon M. and Ozbay, U. (2002) 'Numerical modeling of yielding chain pillars in longwall mines' in Hammah, R. Bawden, w. and Curran, j (eds) *Mining and Tunneling Innovation and Opportunity, Proceeding of 5th North America Rock Mechanics Symposium*, Toronto, Ontario, Canada.

Bai, M. Kendorski, F. and Van Roosendaal D. (1995) 'Chinese and North American high-extraction underground coal mining strata behaviour and water protection experience and guidelines', in Peng, S.S. (ed.) *Proceeding of 14th International Conference on Ground Control in Mining*, Morgantown, USA, pp. 209-17.

Bandis, S.C. Lumsden, A.C. and Barton, N.R. (1983) 'Fundamental of rock join deformation', *International Journal of Rock Mechanics and Mining Science & Geomechanics Abstracts*, 6, pp. 249-68.

Barton, N., Lien, R. and Lunde, J. (1974) 'Engineering classification of rock masses for the design of tunnel support', *Rock Mechanics*, 6(4), pp. 189-236.

Barton, N.R. and Choubey, V. (1977) 'The shear strength of rock joints in theory and practice' *Rock Mechanics and Rock Engineering*, 10, pp. 1-54.

Barton, N. (2002) 'Some new Q-value correlations to assist in site characterization and tunnel design', *International Journal of Rock Mechanics and Mining Science*, 39(2), pp. 185-216.

Barton, N. and Pandey, S.K. (2011) ‘Numerical modelling of two stoping methods in two Indian mines using degradation of c and mobilization of φ based on Q-parameters’, *International Journal of Rock Mechanics and Mining Science*, 48 (7), pp. 1095-1012.

Barczak, T.M. (1992) ‘*Examination of design and operation practices for longwall shields*’, United States Department of The Interior, Bureau of Mines Information Circular; IC 9320, p.14.

Beer, G. and Meek, J.L. (1982) ‘Design curves for roofs and hanging walls in bedded rock based on Voussoir beam and plate solutions’, *Transactions of the Institution of Mining and Metallurgy*, 91, pp. 18–22.

Bieniawski, Z.T. (1968) ‘The effect of specimen size on compressive strength of coal’, *International Journal of Rock Mechanics and Mining Science*, 5, 325– 335.

Brady, B.H. and Brown, E.T. (1985) *Rock Mechanics for Underground Mining*. 1st edn, Londen: George Allen and Unwin.

Brady, B.H. and Brown, E.T. (2002) *Rock Mechanics for underground mining*. 2nd edn. Netherlands: Springer.

Brown, T. (2003) *Block Caving Geomechanics*. Brisbane: Julius Kruttschnitt Mineral Research Centre, University of Queensland.

Bucky, P.B. (1931) ‘Use of models for the study of mining problems’, *American Institute of Mining and Metallurgical Engineers*, 425, pp. 3–28.

Bucky, P.B. and Taborelli, R.V. (1938) ‘Effects of immediate roof thickness in longwall mining as determined by barodynamic experiments’, *Transactions of the Institution of Mining and Metallurgy*, pp. 130-314.

Cai, M. Kaiser, P.K. Tasakab, Y. and Minamic, M. (2007) ‘Determination of residual strength parameters of jointed rock masses using the GSI system’ *International Journal of Rock Mechanics and Mining Science*, 44(2), pp. 247-265.

Colwell, M.G. Frith, R.F. and Mark, C. (2002) ‘Analysis of Longwall Tailgate Serviceability (ALTS): A Chain Pillar Design Methodology for Australian Conditions’, in Mark, C. Heasley, K. Lannacchione, A.T. and Tuchman, R. (eds) *Proceedings of the Second International Workshop on Coal Pillar Mechanics and Design, Pittsburg, PA, USA*, NIOSH Information Circular 9448, pp 33-48.

Colwell, M.G. Hill, D.J. Frith, R.C. (2003) ‘ALTS II – A Longwall Gateroad Design Methodology for Australian Collieries’, in *Proceedings of the 1st Australasian Ground Control in Mining Conference: Ground Control in Mining: Technology & Practice, Sydney 10 – 13 November 2003*, pp 123-135.

Das, S.K. (2000) ‘Observation and classification of roof strata behaviour over longwall coal mining panels in India’ *International Journal of Rock Mechanics and Mining Science*, 37, pp. 585-97.

Diederichs, M.S. and Kaiser, P.K. (1999) ‘Stability of large excavation in laminated hard rock masses: the voussoir analogue revisited’, *International Journal of Rock Mechanics and Mining Science*, 36, pp. 97-117.

Diederichs. M.S. and Kaiser. P.K. (1999) ‘Authors' reply to Discussion by A. L. Sofianos’, *International Journal of Rock Mechanics and Mining Sciences*, 36(7), pp. 995–999.

Duplanic, P. and Brady, B.H. (1999) ‘Characterization of caving mechanism by analysis of seismicity and rock stress’, in Vouille, G. and Berest, P. (eds) *Preceding of the 9th international congress on rock mechanics, Paris, France*, pp. 1049-1053.

Evans, W.H. (1941) ‘The strength of undermined strata’, *Transactions of the Institution of Mining and Metallurgy*, 50, pp. 475-500.

Everling, G. (1973) ’Die Vorausberechnung des Gebirgsdrucks fur einen Abbauplan’, *Gluckauf*, 109(23), pp. 1131–3.

Frith, R. (2000) ‘Optimising primary bolting to aid roadway development in the current OH & Sen environment: conflict or opportunity’, *Australian Coal Review*, Oct. 2000, pp. 30–35.

Fayol, M. (1885) Sur les movements de terain provoques parl'exploita-tion des mines. *Bull. Soc. Indust. Min*, 14, pp. 818.

Gale, W.J. and Blackwood, R.L. (1987) ‘Stress distributions and rock failure around coal mine roadways’ *International Journal of Rock Mechanics and Mining Science & Geomechanics Abstracts*, 24(3), pp. 165–73.

Ghose, A.K. and Dutta, D. (1987) ‘A rock mass classification model for caving roofs’, *International Journal of Mining and Geological Engineering*, 5, pp. 257-71.

Hebblewhite, B.K. and Lu, T. (2004) ‘Geomechanical Behavior of Laminated, Weak Coal Mine Roof Strata and the Implications for a Ground Reinforcement Strategy’, *International Journal of Rock Mechanics and Mining Sciences*, 41, pp. 147-157.

Hajiabdolmajid, V. Kaiser, P.K. and Martin, C.D. (2002) ‘Modelling brittle failure of rock’, *International Journal of Rock Mechanics & Mining Sciences*, 39, pp. 731–741.

Hansen, T.F. (2004) *Analyse av rasutvikling og vannproblematikk i Svea Nord.* MSc Thesis, Norwegian University of Science and technology, Trondheim, Norway.

Hartman, H.L. and Mutmansky, J.M. (2002) '*Introductory mining engineering*', 2nd edition, Hoboken, New Jersey, John Wiley and Sons.

Heasley, K.A. (1988) *Numerical Modeling of Coal Mines with a Laminated Displacement- Discontinuity Code.* Ph.D. Thesis, Colorado School of Mines, Colorado, USA.

Hoek, E. and Brown, E.T. (1998) 'Practical estimates of rock mass strength' *International Journal of Rock Mechanics & Mining Sciences*, 34, pp. 1165–1186.

Hoek, E. (2001) 'Rock mass properties for underground mines', in Hustrulid W.A. and Bullock, R.L. (eds) *Proceeding of Underground Mining Methods: Engineering Fundamentals and International Case Studies, Litleton, Colorado*, SME.

Hoek, E. (2007) *Practical rock engineering*. Available at: http://www.rocscience.com/education/hoeks_corner, (Accessed 10.08.2012).

ITASCA (2010) *FLAC(3D)-User manual, version 4*. USA-Minnesota.

ITASCA (2010) *UDEC-User manual, version 5.00*. USA-Minnesota.

Ivars, D.M. Pierce, M.E. Darcel, C. Reyes-Montes, J. Potyondy, D. Young, P. and Cundall, P. (2011) 'The synthetic rock mass approach for jointed rock mass modeling', *International Journal of Rock Mechanics & Mining Sciences*, 48(2), pp. 219-244.

Jing, L. And Hudson, J.A. (2002) 'Numerical methods in rock mechanics', *International Journal of Rock Mechanics & Mining Sciences*, 39, pp. 409-427.

Kelly, M. Gale, W. Luo, X. Hatherly, P. Balusu, R. and LeBlanc Smith, G. (1998) 'Longwall caving process in different geological environments – better understanding through the combination of modern assessment methods', in Aziz N.I. and Indrertna B. (eds), *Proceeding of International Conference in Geomechanics/Ground Control in Mining and Construction, Wollongong,* University of Wollongong: Wollongong, pp. 573–89.

Lawrence, H. (2009) 'A method for the design of longwall gateroad roof support', *International Journal of Rock Mechanics & Mining Sciences*, 46, pp. 789–795.

Maceri, A. (2010) '*Theory of elasticity*', Springer, Berlin, 2010.

Mark, C. (1992) 'Analysis of longwall pillar stability (ALPS): an update', in Santa Fe, N.M. *Proceedings of the Workshop on Coal Pillar Mechanics and Design, Pittsburgh, PA*,U.S. Department of the Interior, Bureau of Mines, IC 9315, pp. 238-249.

Mark, C, Chase, F.E, and Molinda, G.M. (1994) 'Design of longwall gate entry systems using roof classification', in Mark, C. (eds) *Proceedings New Technology for Longwall Ground Control: The USBM Technology Transfer Seminar,* U.S. Bureau of Mines Technology Transfer , USBM SP 94-01, pp. 5-18.

Mark, C, and Chase, F.E. (1997) 'Analysis of Retreat Mining Pillar Stability', in Mark, C. and Tuchman, R.J. *New Technology for Ground Control in Retreat Mining: Proceedings of the NIOSH Technology Transfer Seminar*, *Pittsburgh, PA: US,* Department of Health and Human Services NIOSH IC 9446, pp. 17-34.

Mark, C. Russel, F and Mark, C. (1999) 'Analysis of longwall tailgate serviceability (ALTS): A chain pillar design methodology for Australian conditions', Mark, C. Heasley, K. Lannacchione, A.T. and Tuchman, R. (eds) *Proceedings of the Second International Workshop on Coal Pillar Mechanics and Design, Pittsburg, PA, USA*, NIOSH Information Circular 9448, pp. 34-49.

Mark, C, Molinda, G.M. and Dolinar, D.R. (2001) 'Analysis of roof bolt systems' in Peng, S.S. Mark, C. and Khair, A.W. (eds). *Proceedings of the 20th International Conference on Ground Control in Mining*, Morgantown, West Virginia, West Virginia University, pp. 218-225.

Mark, C. (2002) 'Analysis of longwall pillar stability (ALPS): An update' Mark, C. Heasley, K. Lannacchione, A.T. and Tuchman, R. (eds) *Proceedings of the Second International Workshop on Coal Pillar Mechanics and Design, Pittsburg, PA, USA*, NIOSH Information Circular 9448, pp. 238-249.

Mark, C. Gale, W. Oyler, O. and Chen, J. (2007) 'A case history of the response of a longwall entry subjected to concentrated horizontal stress', *International Journal of Rock Mechanics and Mining Sciences*, 44(2), pp. 210-221.

Mark, B. and Pierce, M.E. (2009) 'A review of recent experience in modeling of caving', in Estrehuizen G.S. (ed) *Proceeding of the international workshop on numerical modeling for underground mine excavation design, Pittsburgh, PA, US*, Institute of occupational safety and health (NIOSH), Pitsburg PA, pp. 19-28.

Molinda, G. and Mark, C. (1994) '*Coal mine roof rating (CMRR): a practical rock mass classification for coal mines*. Pittsburgh, PA: U.S. Department of the Interior, Bureau of Mines, IC 9387.

Mortazavi, A. Hassani, F.P. and Shabani. M. (2009) 'A numerical investigation of rock pillar failure mechanism in underground openings' *Computer and Geotechnics*, 36, pp. 691-697.

Narr, W. and Suppe, J. (1991) 'Joint spacing in sedimentary rocks', *Journal of Structural Geology*, 11(9), pp. 1037-48.

NIST/ SEMANTECH. *E-Handbook of statistical methods*. Available at: www.itl.nist.gov/div898/handbook (accessed at 15.01.2012).

Nomikos, P.P. Sofianos, A.I. and Tsoutrelis, C.E. (2002) 'Structural response of vertically multi-jointed roof rock beams', *International Journal of Rock Mechanics and Mining Sciences*, 39(1), pp. 79–94.

Obert, L. and Duvall, W.I. (1966) *Rock mechanics and the design of structures in rock*. John Wiley and Sons, 649 pp.

Orest, P. (2005) 'Back-analysis techniques for the improvement of the understanding of rock in underground constructions', *Tunnelling and Underground Space technology*, 20, pp. 7-21.

Pappas, D.M. and Mark, C. (1993) *Behavior of simulated longwall gob material.* US Department of the Interior, Bureau of Mines: Report of Investigations, RI-9458.

Park, D.W. and Gall, V. (1988) 'Supercomputer assisted three-dimensional finite element analysis of a longwall panel', In Khair A.W. (ed), *Rock Mechanics as a Guide for Efficient Utilization of Natural Resources, Proceeding of 30th U. S. Rock Mechanics Symposium*, Morgantown, pp 133–40.

Peng, S.S. and Chiange, H.S. (1984) *Longwall mining*. New York: Wiley.

Price, N.J. (1966) '*Fault and joint development in brittle and semi-brittle rock*', London: Pergamon Press Ltd.

Ran, J.Q. Passaris, E.K.S. and Mottahed, P. (1994) 'Shear sliding failure of the jointed roof in laminated rock mass', *Rock Mechanics and Rock Engineering*, 4, pp. 235-51.

Rocscience '*Examine 2D: 2D Stress Analysis for Underground Excavations version 7.0*' Available at http://www.rocscience.com/products/11/Examine2D (Accessed at 20.03.2012).

Salamon, M.D.G. (1964) 'Elastic analysis of displacements and stresses induced by mining of seam or reef deposits. Part II', *Journal of the South African Institute of Mining and Metallurgy*, 64, pp. 197–218.

Salamon, M.D.G. and Munro, A.H. (1967) 'A study of the strength of coal pillars' *Journal of the South African Institute of Mining and Metallurgy*, 67, pp 55-67.

Salamon, M.D.G. (1999) 'Mechanism of caving in longwall coal mining', in Hustrulid, W. and Johnson, J.A. (eds) *Rock mechanics contributions and challenges: proceedings of 31th U.S. symposium. Denver Co. A.A,*Taylor & Francis, pp. 161-168.

Sepehr, K. and Stimpson, B. (1988) ‘Roof deflections and sag in jointed horizontally bedded strata—a numerical study’, *Rock Mechanics and Rock Engineering*, 21, pp. 207–218.

Sing, G.S.P. and Sing, U.K. (2009) ‘A numerical modeling approach for assessment of progressive caving of strata and performance of hydraulic powered support in longwall workings’, *Computers and Geotechnics*, 36, pp. 1142-1156.

Sheorey, P.R. (1984) ‘Use of rock classification to estimate roof caving span in oblong workings’, *International Journal of Mining engineering*, 2, pp. 133-40.

Smart, B.D. and Aziz, N.I. (1989) ‘The influence of caving mechanism on powered support rating’, *Aust IMM Bull Proc*, 294(4), pp. 77–84.

Sofianos, A.I. (1996) ‘Analysis and design of underground hard rock Voussoir beam roof’, *International Journal of Rock Mechanics and Mining Sciences*, 33(2), pp. 153–166.

Sofianos, A.I. and Kapenis, A.P. (1998) ‘Numerical evaluation of the response in bending of an underground hard rock Voussoir beam roof’ *International Journal of Rock Mechanics and Mining Sciences*, 35(8), pp. 1071–1086.

Sofianos, A.I. (1999) ‘Discussion of the paper by M. S. Diederichs and P. K. Kaiser 'Stability of large excavations in laminated hard rock masses: the Voussoir analogue revisited’, *International Journal of Rock Mechanics and Mining Sciences*, 36(7), pp. 991–993.

Sterling, R.L. (1980) ‘The ultimate load behaviour of laterally con-strained rock beams’, in Summers, D.A. and Compiler (eds) *The state of the art in rock mechanics, Proceeding of the 21st US Symposium on Rock Mechanics, University of Missouri-Rolla, May 28-30, 1980,* University of Missouri-Rolla.

Tajdus, K. (2009) ‘New method for determining the elastic parameters of rock mass layers in the region of underground mining influence’, *International Journal of Rock Mechanics and Mining Sciences,* 46, pp. 1296–1305.

Talesnick, M.L. Ya’acov, N.B. and Cruitoro, A. (2007) ‘Modeling of a Multiply Jointed Voussoir Beam in the Centrifuge’, *Rock Mechanics and Rock Engineering*, 40(4), pp. 383-404.

Thin, G.T. Pine, R.T. and Trueman, R. (1993) ‘Numerical modelling as an aid to the determination of the stress distribution in goaf due to longwall coal mining’, *International Journal of Rock Mechanics and Mining Sciences & Geomechanics abstracts*, 7, pp. 1403-09.

Timoshenko, S. and Gere, M. (1961) *Theory of Elastic Stability*. McGraw-Hill, 541 p.

Thomas, G.B. (2011) *Calculus and analytic geometry*. 12th edn. Reading, Mass. Addison-Wesley.

Trueman, R. (1990a) ‘The application of a numerical model to longwall coal mine roadway design’, *Mining Science Technology*, 10, pp. 157-165.

Trueman, R. (1990b) ‘A finite element analysis for the establishment of stress development in a coal mine caved waste’, *Mining Science Technology*, 10, pp. 247-252.

Trueman, R. Lyman, G. and Cocker, A. (2009) ‘Longwall roof control through a fundamental understanding of shield-strata interaction’, *International Journal of Rock Mechanics and Mining Sciences*, 46, pp. 371-380.

Tsesarskey, M. and Talesnick, M.L. (2007) ‘Mechanical response of a jointed beam-Numerical study of centrifuge models’, *International Journal of Numerical and Analytical Methods in Geomechanics*, 31, pp. 977–1006.

Vakili, A. and Hebblewhite, B.K. (2010) ‘A new cavability assessment criterion for Longwall Top Coal Caving’, *International Journal of Rock Mechanics and Mining Sciences*, 47, pp. 1317-1329.

Wargle, L. (1993) ‘*The use of numerical modeling for underground coal mine design*’. in Comprehensive rock engineering, Hudson, J.A. (ed), Oxford: Pergamon Press; pp. 733-748.

Whittaker, B.N. (1974) ‘An appraisal of strata control practice’, *Mining Engineering*, 134, pp. 9–24.

Whittles, D.N. Lowndes, I.S. Kingman, S.W. Yates, C. and Jobling, S. (2006) ‘Influence of geotechnical factors on gas flow experienced in UK longwall coal mine panels’, *International Journal of Rock Mechanics and Mining Sciences*, 43, pp. 369-387.

Wilson, A.H. (1977) ‘The effect of yield zones on the control of ground’, in Proceeding of *6th International Strata Control Conference*, Banff, Paper 3.

Wilson, A.H. (1981) ‘Stress and stability in coal rib sides and pillars’, in Peng S.S. (eds), *Proceeding of 1st Annual Conference on Ground Control in Mining, West Virginia University*, pp. 1–12.

Wilson, A.H. (1982) ‘Pillar stability in longwall mining’, in Chugh Y.P. Karmis M. (eds). *State of the art of ground control in longwall mining science. New York,* SME, pp. 85–95.

Wright, F.D. (1972) ‘Arching action in cracked roof beams’, in *Proceedings of the 5th International Strata Control Conference, London*, National Coal Board , pp. 1–9.

Yavuz, H. (2004) ‘An estimation method for cover pressure re-establishment distance and pressure distribution in the goaf of longwall coal mines’, *International Journal of Rock Mechanics and Mining Sciences*; 41, pp. 193–205.